Making Sense of Disorder in Molecular Solids Using Solid-State NMR

HELEN MICHELLE WICKINS

Making Sense of Disorder in Molecular Solids Using Solid-State NMR

A thesis by

Helen Michelle Wickins

Submitted to Durham University

for the degree of

Doctor of Philosophy

Department of Chemistry

March 2023

Declarations

I hereby declare that this thesis is an original work and has not been submitted for a degree, diploma or other qualification at any other University. It is my own work unless referenced to the contrary in the text.

Abstract

Crystalline materials are typically characterised by diffraction-based techniques which excel at solving the structures of well-ordered materials. However, these techniques have difficulty characterising disorder, as it disrupts the long-range order needed for defined Bragg peaks. Solid-state nuclear magnetic resonance (NMR) is an excellent tool for studying disorder, as it is sensitive to local environment and can detect motion over many orders of magnitude. In this work, NMR-based techniques, primarily lineshape and relaxation analyses, are used in combination with diffraction and molecular dynamics (MD) simulations to uncover the dynamic disorder in three types of system. Firstly, despite limited amounts of some samples, NMR is able to characterise the dynamics of diamondoids, a series of rigid hydrocarbon cages. In diamantane and 1(2)3 tetramantane, ^{13}C relaxation shows evidence of C_3 rotations with activation energies of 21.1(4) kJ mol^{-1} and 15(2) kJ mol^{-1} respectively. For triamantane, second moments, a historical method of summarising static ^{1}H lineshapes, show that the molecules undergo multi-axis jumps, information that could not be obtained through modern NMR or diffraction-based techniques. Secondly, the phase transition in the relaxor ferroelectric material, hydrazinium magnesium formate, is shown to be caused by reorientation of hydrazinium ions from perpendicular to parallel in the channels. Here, a new mechanism is proposed whereby the relaxor ferroelectric response arises directly because of the molecular motion, not despite it. Finally, MD simulations reveal that the dynamics of the solvent molecules in two cocrystal solvates of furosemide-picolinamide have significant librational character. This explains why lineshape and relaxation analyses, which assume a constant amplitude with temperature, are unable to provide a coherent dynamic model. In summary, the NMR techniques used herein, along with supporting diffraction and computational tools, supports their utilisation in the future to better understand disordered materials.

Acknowledgments

First and foremost, I would like to thank my supervisor, Professor Paul Hodgkinson, for your guidance and support throughout my PhD. Without your technical suggestions and insightful discussions, this project would not have been possible. I am also extremely grateful to Dr David Apperley who taught me everything I know in the lab. Your ability to give relatable answers to my questions, both the ridiculous and the profound, was unrivalled. I am also very grateful to the Leverhulme Trust for funding my PhD.

I would like to thank everyone in the solid-state NMR groups, both past and present, in particular: Karen for conducting my yearly reviews; Caitlin for your unwavering positivity; and Sam for showing me that David's way is not the only way!

There are also a number of researchers, internal and external, who deserve a mention for their help on specific projects. Thank you to Robert Glaser for providing the extremely rare diamondoid samples. Thank you to Paul Saines's group at the University of Kent, for providing the MOF samples and analysing the diffraction studies. Lastly, thank you to everyone involved in the computational analysis of FSPA, namely: Vasily, Mark, Gül, Valentina and Will.

On a personal note, I must thank my parents for supporting my interest in science from the beginning. I am also grateful to Amy for your attention to detail whilst proof reading this thesis. A special thanks goes to Jo who has supported me through everything throughout my PhD. You have kept me writing when I wanted to stop and read my chapters in remarkable detail. You, along with Rosalind, Archie and Ada, have always kept a smile on my face. Thank you.

Finally, I thank the examiners, Professor Yaroslav Khimyak and Dr Samuel Page for taking the time to read my work, I hope you find it interesting.

List of Abbreviations

API Active pharmaceutical ingredient

CC Correlation coefficient

CP Cross polarisation

CSA Chemical shift anisotropy

DE Direct excitation

dHMF Deuterated HMF

DSC Differential scanning calorimetry

FID Free induction decay

FS Furosemide

FSPA Furosemide-picolinamide

FWHM Full width at half maximum

HMF Hydrazinium magnesium formate

IR Inversion recovery

MAS Magic-angle spinning

MC Monte Carlo

MD Molecular dynamics

MOF Metal organic framework

NMR Nuclear magnetic resonance

PA Picolinamide

PXRD Powder X-ray diffraction

RF Radio frequency

SCND Single-crystal neutron diffraction

SCXRD Single-crystal X-ray diffraction

TMS Tetramethylsilane

TOSS Total sideband suppression

XRD X-ray diffraction

Contents

Chapter 1

Background and Thesis Overview

1.1 Disorder in Molecular Organic Solids

Characterising solid materials primarily focuses on determining structure. This is typically done with diffraction techniques which excel at determining the structure of ordered materials. However, a common challenge of interpreting diffraction data arises from crystallographic disorder, since Bragg diffraction relies on long-range order.

There are two main types of crystallographic disorder: static disorder, where atoms are fixed in a non-crystalline arrangement, and dynamic disorder, where the positions of atoms change with time. There are many types of materials which exhibit static and dynamic disorder in varying amounts as summarised in Figure 1.1.[1] Crystalline solids, with periodic arrangements of fixed atoms, are the most ordered materials while liquids have maximum static and dynamic disorder. Amorphous solids, which have significant static disorder, can be described as glassy when there is little dynamic disorder, or rubbery when there is more mobility. There are also types of system with significant periodicity but have notable dynamics. These include plastic crystals and many inclusion compounds. Finally, there are liquid crystals, systems with significant mobility and static disorder but with ordering in some dimensions.

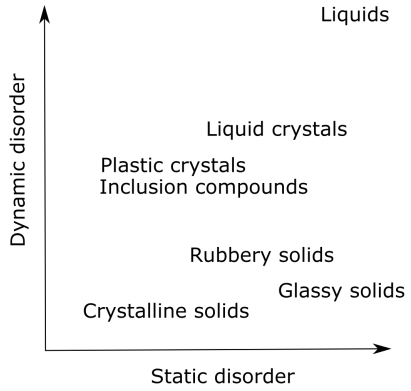

Figure 1.1: The dynamics in different types of matter. Adapted from reference 1.

Understanding and characterising disorder is beneficial in many different fields. In the pharmaceutical industry a full understanding of molecular properties, and how these impact the critical attributes of drug products, is essential.[2] In fields such as functional materials, it is often not sufficient to understand the structure of the material, as it is the molecular motion in a system which often explains the material's bulk properties.

Solid-state nuclear magnetic resonance (NMR) is an excellent method of studying disorder as, in contrast to Bragg diffraction, NMR is sensitive to local environment. Moreover, dynamics are fundamental to every NMR measurement. In fact, the stark differences between solid- and solution-state NMR originate from the differences in the molecular dynamics. In solutions, molecules tumble rapidly and isotropically, averaging all orientation dependent interactions to the isotropic value. In solids, these interactions usually remain and are moderated by the molecular dynamics, meaning spectra are more difficult to interpret in the solid state but retain information about the molecular dynamics.

Solids have a range of potential motions, including vibrations, small-angle librations, jump-type motions involving a whole molecule rotation and translational motions. This thesis is primarily focused on reorientation motions which can be characterised by many different NMR techniques. While vibrations are important solid-state motions, they typically occur on a much faster timescale than relevant for NMR so only averages are observed.

Dynamic processes in solids can be described with an autocorrelation function, $G(\tau)$, which is a measure of the proportion of molecules that are in the same position at time t and $t + \tau$. $G(\tau)$ decays with increasing τ resulting in Equation 1.1 for simple random motion where τ_c is defined as the correlation time of the motion. Correlation times are used to quantify the rate of motion; the smaller the τ_c, the faster the motion.

$$G(\tau) = \exp\left(-\frac{\tau}{\tau_c}\right) \tag{1.1}$$

Motions are often described in terms of rates, ν, which are defined in terms of the correlation time in Equation 1.2. Rates of motion in the solid state can span many orders of magnitudes from slow polymer chain reorientation on the order of Hz, to vibrations around 10^{14} Hz.

$$\nu = \frac{1}{2\pi\tau_c} \tag{1.2}$$

NMR is sensitive to motion over many orders of magnitude, however individual experiments are only sensitive to a relatively narrow motional range. When describing rates of motion with solid-state NMR, it is useful to place motions into three categories: intermediate, slow and fast.

Intermediate dynamics usually involve hindered jumps such as phenyl ring flips or sidechain reorientation. Dynamics in this region directly affect the NMR spectrum and hence fitting lineshapes can be a powerful technique. This is most widely used with static

^{2}H lineshapes which change rapidly in width and shape when the jump rate is the order of the quadrupolar coupling ($\approx 200\,\text{kHz}$). Intermediate dynamics can also be observed in static ^{1}H lineshapes which will narrow with motion on a similar rate to the homonuclear dipolar coupling ($\approx 20\,\text{kHz}$).

Slow dynamics are too slow to directly show up in a spectrum. They typically involve significant structural rearrangement, for example polymer chain dynamics. Slow motions are best studied with exchange-type experiments since the motion is often slow enough to observe a change in chemical shift.

Fast dynamics are too fast to directly show up in a spectrum. They typically involve weakly hindered entities such as methyl rotation or guest reorientation in a host-guest system. Fast motions are often studied by T_1 relaxation, which is sensitive to fluctuations in the local field caused by molecular motions on the order of the Larmor frequency i.e. 100s of MHz. This can provide motional parameters such as activation energies and rates of motion. Relaxation of isotopically dilute nuclei, such as ^{13}C and ^{15}N, can be used to obtain detailed dynamic information, for example the molecular moiety involved or the geometry of the motion. Relaxation of isotopically abundant nuclei, such as ^{1}H, can provide dynamic information without site resolution.

NMR has been used extensively to characterise dynamic disorder in a wide variety of materials, such as proteins and biomolecules, metal organic frameworks (MOFs), liquid crystals, polymers and macromolecules. The focus of the information obtained often varies significantly on each class of material depending on what is deemed to be relevant in that field. For example, polymer research tends to focus on side chain dynamics;[3] studies on MOFs often use solid-state NMR to analyse gas adsorption/desorption behaviour, which is critical for applications in the carbon capture field.[4,5] The solid-state NMR of proteins and biomolecules is heavily focused on determining how hydration levels affect molecular motion, which gives information about biologically relevant parameters.[6–10]

1.2 Thesis Overview

This thesis will show how NMR-based techniques can be applied in three types of system to analyse disorder. Applicable theory is given in Chapter 2 which gives a brief overview of how NMR works and the basic experimental techniques used in solid-state NMR. The second half provides a more detailed description of how relaxation and lineshapes can be used to study motion in solids. Chapter 3 describes some of the specific experimental techniques common to subsequent results chapters.

Chapter 4 focuses on the dynamics of diamondoids, a series of hydrocarbon molecular cages found in crude oil. The first half of the chapter documents the spectra and relaxation times of diamantane, triamantane, 1(2)3 tetramantane and cyclohexamantane, and shows how relaxation can be used to determine motional parameters, such as activation energies and rates of motion. The strengths and limitations of relaxation data for determining the geometry of motions is also discussed. The second half of the chapter

focuses on second moments, a historical method of describing static ^{1}H lineshapes which were previously used to understand dynamics in the solid state. They fell out of favour due to difficulty calculating the second moments of dynamic molecule, as well as the discovery and preferred use of new techniques, such as relaxation, which were often more informative. This section shows that second moments can still be a useful complementary tool to relaxation.

Chapter 5 examines the structure and dynamics of hydrazinium magnesium formate (HMF), a MOF which exhibits unusual phase-dependent relaxor ferroelectric behaviour. Unlike most 'so-called' relaxors, the relaxor ferroelectric behaviour is seen above the phase transition. NMR is used alongside diffraction studies to understand the dynamics of the hydrazinium ion above and below the phase transition, which is shown to directly relate to the material's macroscopic properties.

Finally, in Chapter 6 the dynamics of the solvent molecules in two cocrystal solvates of furosemide-picolinamide (FSPA), FSPA ethanol and FSPA acetone are studied. Here, the standard ^{2}H lineshape and relaxation analyses are more difficult and appear to give contradictory information. This is explained in the second half of the chapter which uses molecular dynamics (MD) simulations to show that the solvent molecules are undergoing a barrierless motion. This means that the standard NMR relaxation analysis, which assumes motions have an energy barrier, is no longer valid.

Chapter 2

Theory of Solid-State NMR

The complete theory of NMR is notoriously complex and a full understanding of even the simplest experiment is fundamentally impossible without quantum mechanics. However, there are models and concepts which are used to understand and predict aspects of NMR without the need for quantum mechanics. The following section focuses on the semi-classical descriptions which are sufficient for understanding the subsequent results presented in this thesis. For further details or information regarding quantum mechanical approaches the reader is pointed to the following books: *Spin Dynamics: Basics of Nuclear Magnetic Resonance*[11] by M. H. Levitt; *Understanding NMR Spectroscopy*[12] by J. Keeler; *Introduction to Solid-State NMR Spectroscopy*[13] by M. Duer; and *Solid-State NMR Basic Principles & Practice*[1] by D. Apperley, R. Harris and P. Hodgkinson.

2.1 Nuclear Magnetism

A nucleus has a property known as spin, which, like mass or electric charge, is an intrinsic property of elementary particles. The spin of a nucleus, I, can take any zero, positive integer or positive half integer value, and determines the magnitude of the angular momentum of the nucleus. Quantum mechanics states that a nucleus with spin I has $2I + 1$ orientations, each with degenerate energy. For example, ^{1}H, ^{13}C and ^{15}N are spin-$\frac{1}{2}$ nuclei so have two orientations; any nucleus with a spin greater than $\frac{1}{2}$ is called a quadrupole and will have three or more orientations as discussed further in Section 2.4.2.1. When nuclei are placed in a strong external magnetic field, $\boldsymbol{B}_0$, the energy levels split into non-degenerate levels with the energy difference, ΔE, proportional to the field strength. This is shown in Equation 2.1 where γ is the magnetogyric ratio and $\hbar$ Planck's constant, h, divided by 2π. This is known as the Zeeman effect. At equilibrium, the spins will distribute between the two levels according to the Boltzmann distribution meaning there is a very small preference for the low energy state. This results in a small net magnetisation, $\boldsymbol{M}_0$, within the sample aligned with the magnetic field as described by Equation 2.2, where N

is the number of nuclei, k is the Boltzmann constant and T is the temperature.

$$\Delta E = \gamma \hbar B_0 \tag{2.1}$$

$$M_0 = \frac{N(\gamma\hbar)^2 B_0}{4kT} \tag{2.2}$$

During a pulse sequence, a radio frequency (RF) pulse is applied at the resonant frequency, or Larmor frequency (ν_{NMR}), equivalent to the energy difference of the two states, as shown in Equation 2.3. This will interact with the nuclear spins in the sample causing transitions between the energy levels.

$$\nu_{\mathrm{NMR}} = \frac{\Delta E}{h} = \frac{\gamma B_0}{2\pi} \tag{2.3}$$

2.1.1 The Vector Model

Although each spin system must be treated quantum mechanically, the effects of RF pulses on a system can be pictured semi-classically with the 'vector model'. First proposed by Bloch in 1946, the vector model treats the net magnetisation, $\boldsymbol{M}_0$, as a vector pointing along the direction of the applied field (by convention along z).[14]

In the vector model, when the sample is placed in an external magnetic field, $\boldsymbol{B}_0$, the bulk magnetisation precesses at frequency ν_{NMR} around $\boldsymbol{B}_0$. When there is an applied RF pulse, the magnetisation also interacts with $\boldsymbol{B}_1(\mathrm{t})$, the much weaker RF field at the frequency ν_{RF}. For convenience and simplicity of explanations, experiments are described in a coordinate frame known as 'the rotating frame of reference'. This frame rotates around the z axis in time with the RF field, ν_{RF}. In this rotating frame, $\boldsymbol{B}_1(\mathrm{t})$ appears to be static and directed in the xy plane depending on the phase of the pulse. If a pulse is applied exactly on resonance ($\nu_{\mathrm{RF}} = \nu_{\mathrm{NMR}}$) then $\boldsymbol{B}_0$ is effectively eliminated and the bulk magnetisation is affected by $\boldsymbol{B}_1$ only. In this case, the RF pulse rotates the magnetisation vector in the yz plane.

In a real sample, there will be several resonances due to electron shielding. Each resonance will have a slightly different Larmor frequency hence $\nu_{\mathrm{RF}} = \nu_{\mathrm{NMR}}$ no longer holds for every spin in the system.

2.1.2 The Pulse-Acquire Sequence

The simplest method of recording an NMR spectrum is through a pulse-acquire sequence, also known as direct excitation (DE). Firstly the RF power is applied for the time taken to rotate the magnetisation 90 °, from the z axis into the xy plane. Since the precession or nutation rate is dependent on the power of the RF pulse used, the time of the pulse must first be calibrated at the chosen power with a nutation curve. Secondly, when the pulse has finished, the precession of the resulting magnetisation is detected in the xy plane

during the acquisition time. Before another pulse is applied, the system is allowed to relax back to equilibrium in both the xy plane and z axis.

2.1.3 The Free Induction Decay

After applying a pulse, the precession of the magnetisation induces a small voltage in the coil of the probe which allows the xy component of the magnetisation to be detected. This precessing magnetisation oscillates at approximately the Larmor frequency and decays due to transverse relaxations, hence it is known as the free induction decay (FID). This FID usually contains multiple signals each with a slightly different frequency which makes it difficult to analyse directly. Therefore the signal is Fourier transformed which takes the time-domain signal and converts it into a frequency-domain spectrum.

2.2 Relaxation

Relaxation drives the spins in a sample to equilibrium following a perturbation, such as a pulse. There are three different relaxation processes that are considered here:

- $\boldsymbol{T_1}$**: Spin-lattice relaxation** or longitudinal relaxation is the process of returning the z component of the bulk magnetisation to thermodynamic equilibrium with its surroundings, the 'lattice', in the static magnetic field. It involves the spins flipping between energy levels so that a Boltzmann distribution can be reached and is described by an exponential with a time constant T_1. In the solid state, T_1 can be significantly longer than the acquisition time, which means a delay is needed between each repetition to allow the spins to return to equilibrium (see Section 3.3).

- $\boldsymbol{T_2}$**: Spin-spin relaxation** or transverse relaxation (T_2 and T_2*) is the process of the spins exchanging energy with themselves. At equilibrium the xy components of magnetic moments are randomly distributed in the xy plane meaning there is no measurable net magnetisation. When an RF pulse is applied, the spins become coherent. The T_2* process is the returning of the xy component of $\boldsymbol{M}$ to zero and hence causes the FID to actually decay. T_2 relaxation is measured from the decay of the signal from a series of echo experiments. The difference between T_2 and T_2* results primarily from inhomogeneities in the magnetic field, i.e. if the magnetic field were perfectly homogeneous $T_2 = T_2$*.

- $\boldsymbol{T_{1\rho}}$**: Spin-lattice relaxation in the rotating frame** is the process of returning the xy component of $\boldsymbol{M}_0$ to zero in the presence of an RF field. Under these circumstances, the magnetisation has been spin-locked and so the decay is much slower than T_2 relaxation. It can be likened to T_1 relaxation, but instead of applying to relaxation along $\boldsymbol{B}_0$ it applies to relaxation along $\boldsymbol{B}_1$, the RF field.

2.3 NMR in the Solid State

The basic principles of NMR in the solid and the solution state are identical, however the techniques used and the appearance of spectra are very different. Molecules in solution tumble rapidly and isotropically which leads to the averaging of the internal interactions to the isotropic value. In solids, molecules are much more restricted so orientationally dependent interactions will affect spectra. This can reduce spectral resolution and significantly increase the complexity of spectra. However, this increased complexity hides the potential to extract far greater information.

2.3.1 Internal Interactions

There are multiple internal interactions which affect NMR. Table 2.1 summarises the most relevant interactions in solids.

Table 2.1: Properties of internal interactions.

	Label	**Isotropic value**	**Approximate magnitude / Hz**
Shielding	σ	σ_{iso}	$10^2 - 10^5$
Dipolar coupling	D	0	$10^3 - 10^4$
Quadrupolar coupling	Q	0	$10^3 - 10^7$

2.3.1.1 Shielding

When a sample is placed into an external field, the electrons in the molecules shield the nuclei resulting in the nuclei experiencing a slightly reduced field. The extent of the reduction is dependent upon the electronic arrangements in the different chemical environments in the molecules. This gives rise to chemical shifts where different chemical environments have different resonant frequencies.

Due to asymmetry of the local electronic environment surrounding the nucleus, shielding is an anisotropic interaction meaning the magnitude of the shielding depends on the orientation of the molecule to the field. In solids, anisotropic interactions leads to powder patterns which are distinctive lineshapes due to the random orientation of crystallites in a sample. Shielding anisotropy leads to chemical shift anisotropy (CSA), which can usually be spun out with magic-angle spinning. In the solution state, the CSA, as with other internal interactions, is reduced to the isotropic value due to rapid molecular tumbling.

2.3.1.2 Dipolar Coupling

Dipolar coupling is the through-space interaction between two spins. Due to heteronuclear dipolar coupling, a ^{13}C spectrum of a an isolated carbon-hydrogen pair would appear as a doublet with the spacing proportional to $(3\cos^2\theta - 1)$, where θ is the angle between

the internuclear vector and the magnetic field. This shows that dipolar coupling is an orientation dependent interaction. In a powder sample, dipolar coupling results in line broadening. Dipolar coupling is axially symmetric about the internuclear vector, however anisotropic motion affecting the two spins involved can cause an asymmetry in the averaged dipolar coupling tensor.

2.3.1.3 Quadrupolar Coupling

Quadrupolar coupling applies to any nucleus with spin greater than a half. It is an electric interaction, not a magnetic interaction and it is due to the electric quadrupole moment (Q), a parameter which gives the effective shape of the nuclear charge distribution. In spin-$\frac{1}{2}$ nuclei $Q = 0$ due to symmetry but quadrupoles can have a positive or negative electric quadrupole moment which can interact with the electric field gradient and cause extensive broadening. When present, quadrupolar couplings can dominate the appearance of spectra since they can be very large, up to 10s of MHz. Quadrupolar coupling and lineshapes are covered in Section 2.4.2.1.

2.3.2 Basic Solid-State NMR Techniques

2.3.2.1 Solid Echoes

Within an NMR probe, the same coil produces the high voltage RF pulse and detects the minute FID response. To allow the pulse to fully finish, and give the circuitry time to settle, there is a period of time, known as the dead time ($\approx 6\,\mu s$), between the end of the pulse and the start of the FID recording. With a long FID, the effect of missing the first few data points is not hugely significant and will at worst result in spectrum phasing issues which are easily fixed in the processing. However for short FIDs, which are typical for static ^{1}H and ^{2}H spectra, a significant amount of the signal is lost in the dead time. To overcome this, an echo is often used for static spectra. After the initial 90 ° pulse, the spins are all coherent in the xy plane. There is then a delay, τ, when the magnetisation starts to precess in the xy plane at approximately the ν_{RF}. In the rotating frame of reference, the spins spread out from the y axis in the xy plane due to dipolar interactions, quadrupolar interactions and/or CSA. After a delay time there is then a refocusing pulse which flips the spins such that the spins are refocused back to the y axis over a time equal in length to the first delay, τ. In systems where CSA is the dominant interaction, a 180 ° refocussing pulse is used and this is known as a spin echo. In systems where dipolar or quadrupolar interactions are dominant, a 90 ° refocussing pulse is used and this is known as a solid echo.

2.3.2.2 Cross Polarisation

For dilute nuclei such as ^{13}C and ^{15}N, a simple pulse-acquire sequence typically results in spectra with low signal-to-noise. To combat this, cross polarisation (CP) is used which

transfers magnetisation from abundant spin nuclei, such as ^{1}H, to the nuclei of interest. This improves signal-to-noise in two main ways. Firstly the repetition rate, or recycle delay, of pulses is determined by the T_1 relaxation time (covered in Section 3.3). Since ^{1}H T_1 relaxation times are typically much shorter than ^{13}C/^{15}N relaxation times, there can be many more repetitions in the same experimental time. Secondly the strength of an NMR signal depends on the difference in energy, ΔE, which is proportional to the magnetogyric ratio as shown in Equation 2.3 on page 6. Hence the signal intensity is improved by a factor of 4 ($\gamma^{^{1}\mathrm{H}}/\gamma^{^{13}\mathrm{C}}$) or 10 ($\gamma^{^{1}\mathrm{H}}/\gamma^{^{15}\mathrm{N}}$) for ^{13}C and ^{15}N spectra respectively.

A basic CP sequence involves an initial 90 ° pulse on the ^{1}H channel with phase x, bringing the ^{1}H magnetisation into the y axis. A ^{1}H spin-lock pulse with phase y is then applied with the aim of maintaining magnetisation in the y axis. At the same time, a contact pulse is applied to the X channel at a calibrated power such that the nutation rates of each channel are equal ($\nu_1{}^{\mathrm{H}} = \nu_1{}^{\mathrm{X}}$)*. During this contact time, the magnetisation transfers from the ^{1}H spins to the X spins. The X signal is then recorded, often with ^{1}H decoupling.

2.3.2.3 Magic-Angle Spinning

Solid-state NMR uses a technique called magic-angle spinning (MAS) to help resolve signals and reduce the effects of internal interactions. Chemical shielding, dipolar coupling and quadrupolar coupling all have $\frac{1}{2}(3\cos^2\theta - 1)$ orientational dependence where θ is the angle between the principal axis and $\boldsymbol{B}_0$. Physically rotating a sample at 54.74 ° will, in theory, multiply the anisotropies by zero. However, to fully narrow the signal, the spin rates must be much larger than the size of the interaction. This is possible for some interactions, such as ^{13}C CSA, difficult for others, such as homonuclear ^{1}H dipolar interactions, and impossible in others, such as quadrupoles with significant quadrupolar coupling constants (due to the second order quadrupolar coupling interaction).

If spinning speed is comparable to the size of the interaction, MAS can result in spinning sidebands, which is explained further in Section 2.4.2. These appear as additional resonances spaced at the spinning rate apart from the isotropic chemical shift. In some instances spinning sidebands can prove useful by providing information about the anisotropic interaction which is being partially averaged. In instances where sidebands are not desirable, they can be suppressed through sequences such as total sideband suppression (TOSS). TOSS uses four 180 ° pulses before the acquisition which effectively randomises the phases of the spinning sidebands while preserving the phase of the isotropic resonances.

*This breaks down at high spinning speeds and instead magnetisation becomes most efficient on a sideband i.e. $\nu_1{}^{\mathrm{H}} = \nu_1{}^{\mathrm{X}} \pm n\nu_{\mathrm{r}}$ where ν_{r} is the spinning rate and $n = 1$ or 2.

2.4 Using Solid-State NMR to Study Disorder

Almost all NMR interactions are anisotropic i.e. the strength of the interaction depends on the orientation of the spin or spins to the applied magnetic field. Solid-state NMR spectroscopists usually work hard to suppress these anisotropic interactions through MAS. However, the anisotropic nature of the internal interactions is invaluable when interested in molecular motion since a molecular reorientation can be observed through the change of strength of an NMR interaction.

Solid-state NMR is sensitive to motion over many orders of magnitude; the timescale of the motion dictates the type of experimental techniques that are used. Motion on the order of Hz-kHz is classed as slow, and is typically measured though exchange-type experiments. Intermediate motion can be measured though lineshapes and is typically on the order of 10s – 100s kHz. Motions on the MHz timescale can be probed with relaxation measurements.

2.4.1 Relaxation

Relaxation is driven by molecular motion, and hence measuring relaxation times can be used to probe molecular motions. Different relaxation types give information about motions on different timescales. For example, T_1 relaxation times will be sensitive to motions around the Larmor frequency, which is around 100s of MHz depending on the nuclei studied and magnet used. $T_{1\rho}$ will be sensitive to motion around the spin-lock frequency, which is typically 10s of kHz. T_2 relaxation is rarely used in the solid state because it is difficult to separate true T_2 relaxation from other factors that determine lineshape.

Only limited information can be gained from relaxation rates without fitting the data. Data is typically plotted as an Arrhenius plot, with the common logarithm ($\log_{10}$) or natural logarithm ($\log_e$) of the relaxation time plotted against inverse temperature. This is then fitted to linear combinations of spectral densities with the exact combination depending on the relaxation mechanism, see Equations 2.6 – 2.8.

Relaxation is the result of fluctuating local magnetic fields which are generated from within the sample and will be slightly and randomly different for each spin. They can arise from various sources such as dipolar coupling or CSA. The frequency, ν, of the random fluctuating fields can be described with something known as the spectral density, $J(\nu)$. This is given by Equation 2.4 where τ_c is the correlation time which is defined in Equation 1.1 on page 2.

$$J(\nu) = \frac{2\tau_c}{1 + (2\pi\nu\tau_c)^2} \tag{2.4}$$

Figure 2.1 shows that for faster motions ($\tau_c = 10\,\text{ns}$) the spectral density function is flatter and extends further, hence the random fluctuating fields can sample a much

greater range of frequencies. For slower motions ($\tau_c = 100\,\text{ns}$) fluctuating fields are more restricted to the lower frequencies.

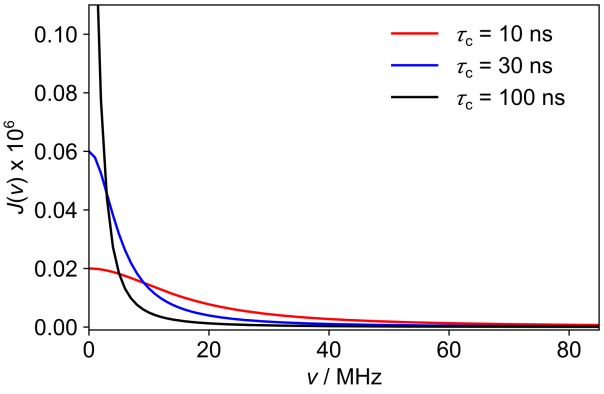

Figure 2.1: A plot to show the spectral density as a function of frequency at three different correlation times.

If a random fluctuating local field happens to be oscillating at the Larmor frequency, it can cause the magnetisation of an individual spin to change orientation, which drives the bulk magnetisation towards equilibrium. An individual experiment is sensitive to random fluctuating fields at one particular frequency i.e. 500 MHz for ^{1}H T_1 relaxation on a 500 MHz spectrometer. Figure 2.2 shows a log-log plot of τ_c vs $J(\nu)$ for three particular frequencies. Note that the gradients are the same for each frequency but the maximum is different for each correlation time. For a given frequency, ν, the spectral density reaches a maximum when $\tau_c \approx (2\pi\nu)^{-1}$. In the extreme narrowing condition, which applies to fast molecular motions, relaxation rates are proportional to τ_c. In the rigid lattice limit, which applies to slow molecular motions, relaxation rates are proportional to ${\tau_c}^{-1}$.

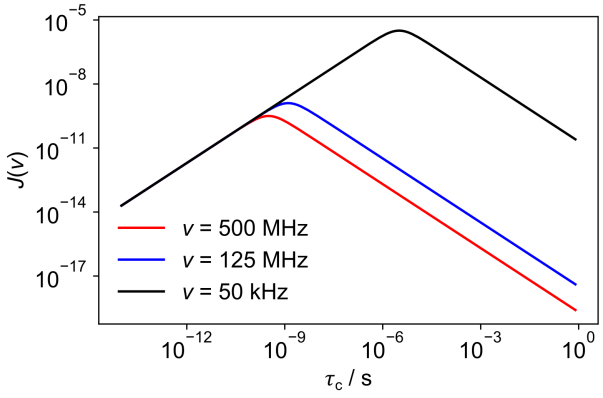

Figure 2.2: A log-log plot to show the spectral density as a function of correlation time.

For thermally activated processes, the correlation time is related to the activation energy, E_a, through Equation 2.5 where R is the gas constant, τ_0 is the pre-exponential

factor and T is the temperature. Plotting a graph of $\ln(T_1)$ against $\frac{1}{T}$ will have a gradient proportional to E_a or $-E_\mathrm{a}$.

$$\tau_\mathrm{c} = \tau_0 \exp\left(\frac{E_\mathrm{a}}{RT}\right) \tag{2.5}$$

For homonuclear dipolar relaxation driven by isotropic motion with Larmor frequency ν_0, or quadrupolar relaxation with Larmor frequency ν_0, relaxation times are fitted to:

$${T_1}^{-1} = AJ(\nu_0, \tau_\mathrm{c}) + 4AJ(2\nu_0, \tau_\mathrm{c}) \tag{2.6}$$

where A is a scaling constant. For heteronuclear dipolar relaxation driven by isotropic motion (e.g. for relaxation of protonated carbons) with spins S(^{13}C) and I(^{1}H) with Larmor frequencies $\nu_{0\mathrm{S}}$ and $\nu_{0\mathrm{I}}$ respectively, relaxation times are fitted to:

$${T_1}^{-1} = AJ(\nu_{0\mathrm{I}} - \nu_{0\mathrm{S}}, \tau_\mathrm{c}) + 3AJ(\nu_0, \tau_\mathrm{c}) + 6J(\nu_{0\mathrm{I}} + \nu_{0\mathrm{S}}, \tau_\mathrm{c}) \tag{2.7}$$

For relaxation around $\boldsymbol{B}_1$ with frequency ν_1:

$${T_{1\rho}}^{-1} \propto \left(\frac{3}{2}J(\nu_1, \tau_\mathrm{c}) + \frac{5}{2}J(\nu_0, \tau_\mathrm{c}) + J(2\nu_0, \tau_\mathrm{c})\right)$$

When $T_1 >> T_{1\rho}$ (generally the case):

$${T_{1\rho}}^{-1} \simeq AJ(\nu_1, \tau_\mathrm{c}) \tag{2.8}$$

These equations are described by Bakhmutov.[15] Using Equations 2.4 – 2.8, the relaxation times are fitted to an E_a, a pre-exponential factor, τ_0, and a scaling constant, A. To make the fitting more stable, the latter two parameters are fitted as a logarithm. This allows the parameters to be fitted to a limited range of linear values, instead of a significant range spanning many orders of magnitudes, by effectively taking the log of Equation 2.5.

There are important differences between analysing relaxation times of abundant and dilute spins. The data is fitted to slightly different equations (given above) and how the data can be used to infer motional geometry is also different. The relaxation times of abundant nuclei, such as ^{1}H, are equalised due to efficient spin diffusion between protons averaging the relaxation times of individual spins. This means that one set of motional parameters is calculated for the whole molecule, which can make interpreting the values more difficult. With dilute nuclei, lack of spin diffusion means that specific relaxation times can be calculated for each site. This can be used to infer the geometry of motions by comparing the relaxation times of each site.

2.4.2 Lineshapes

The effects of motion can be seen in NMR lineshapes in many different ways depending on the dominant interactions in the system. Before discussing how molecular motion affects the lineshapes and linewidths of resonances, it is important to understand the factors that determine the linewidth and how they are affected by various experimental parameters.

Internal interactions are classed as either homogeneous (homonuclear dipolar coupling) or inhomogeneous (CSA, heteronuclear dipolar coupling and first order quadrupolar coupling) depending on how they behave under MAS: the distinction is subtle and originates in the quantum mechanics. Homogeneous interactions are not refocused by MAS, whereas the inhomogeneous interactions are refocused every rotor cycle, which is seen as rotary echoes. This explains why moderate spinning does not produce spinning sidebands in a ^{1}H spectrum in the same way it does in a ^{13}C spectrum.

Figure 2.3 demonstrates the effects of spinning on a sample with moderate inhomogeneous interactions and a T_2 of 2 ms. The green lines show the FID and spectrum of a static sample. The lineshape is broad due to internal interactions which cause the signal to decay more quickly. It is important to note that T_2 remains unaffected; it is the dephasing that is rapid and causes broad lines in the spectrum. The red lines show the FID and spectrum of a sample spinning fast relative to the internal interactions. The internal interactions have been averaged to zero and no longer influence the spectrum. This means that the linewidth is only affected by the T_2 relaxation time, i.e. the irreversible decay of magnetisation in the xy plane. The black lines show the FID and spectrum of a sample being spun at a rate similar to that of the interactions. The interactions have not been fully averaged so the signal rapidly decays. However, under MAS, the evolution of the magnetisation is refocused over a rotor period, forming rotary echoes in the FID. These are seen as a series of spinning sidebands, where the width of each band is determined by the T_2 relaxation time and the overall pattern width determined by the initial decoherence.

There are however other factors that also contribute to broadening. The widths of NMR resonances can be broken down into homogeneous and inhomogeneous contributions. In solution-state spectra, the homogeneous linewidth is the result of the T_2 relaxation, and the inhomogeneous linewidth is caused by magnetic field inhomogeneities. In solid-state spectra, there are many more factors that determine the width of resonances, a brief overview of which is given below.

Just as in solution, the homogeneous linewidth is determined by the T_2 relaxation, which is the overall loss of phase coherence and the cause of irreversible decay of magnetisation in the xy plane. However, in solids it is difficult to determine whether the cause of this decay is due to T_2 relaxation or residual dipolar coupling. For example, static ^{1}H linewidths are broad not because of a short T_2 but because of strong homonuclear dipolar couplings between protons causing rapid dipolar dephasing.

Inhomogeneous contributions are also more complex in solid-state NMR. In solution, each site has an identical environment and spectra have narrow resonances with a

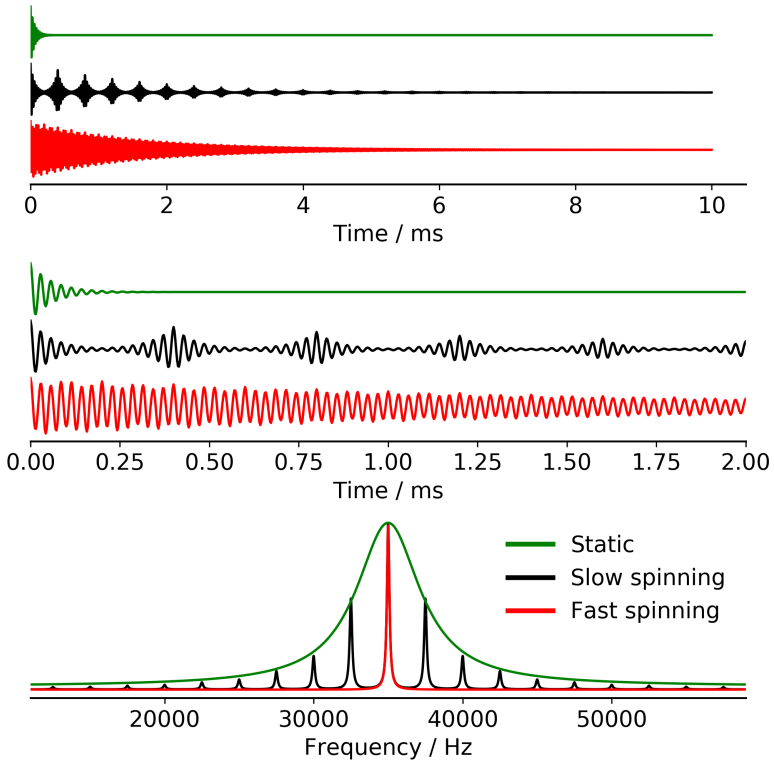

Figure 2.3: Schematic demonstration of the effects of spinning on inhomogeneous interactions. Whole (top) and magnified (middle) FIDs and spectrum (bottom).

defined chemical shift. In solids, particularly amorphous solids, the local environment of a site can vary significantly and so the chemical shift distribution will be broader. Magnetic field inhomogeneity is likely to have a negligible effect on solid-state spectra since there are so many other significant causes of line broadening in the solid state. For this reason, shimming the probe is less of a priority in solid-state NMR compared to solution state.

The overall lineshape of a resonance is a combination of the homogeneous and inhomogeneous lineshapes contributions, however the observed spectrum will primarily be a result of the most dominant contribution in the system of interest. The effect of changing experimental parameters differs depending on what the most dominant contribution is. For example, the linewidths in non-crystalline samples have significant inhomogeneous contributions from the variable environments of each site. Additionally, aromatic systems have a large anisotropy of the bulk magnetic susceptibility, which also contributes to inhomogeneous broadening. This type of broadening will scale with magnetic field strength, which explains why for systems dominated by inhomogeneous broadening, there is no benefit in terms of spectral resolution going to higher magnetic fields.[1] Dilute spins, such as ^{13}C or ^{15}N, are affected by the heteronuclear dipolar coupling and hence the linewidths are very sensitive to the efficiency of the ^{1}H decoupling. This is why CH_2 resonances are often broader than CH or unprotonated carbons and hence faster MAS does not significantly narrow ^{13}C or ^{15}N resonances. However, spectra of abundant spins, such as ^{1}H, ^{19}F or

^{31}P, often benefit from fast MAS since the dominant contribution to the overall linewidth is strong homonuclear couplings that are reduced by increased spinning speeds.

Just as changing experimental parameters has different effects on linewidths depending on the dominant contribution, the effects of molecular motion on linewidths also depends on the dominant contribution in the individual system. Molecular motion drives T_2 relaxation so in the absence of coherent[†] interactions, linewidths of static molecules will be narrower. However, as explained above, the dominant factors contributing to linewidth are usually due to internal interactions and not T_2. For example, with static ^{1}H spectra the dominant contribution is homonuclear dipolar coupling between protons. Any motion which averages this dipolar coupling, i.e. motion above approximately 10 kHz, will have the effect of reducing the linewidth. Different types of motions, such as isotropic motion or rotation about an axis, will average the homonuclear dipolar coupling by different amounts and cause the linewidth to reduce in a predictable way, as discussed in Chapter 4.

For proton decoupled ^{13}C/^{15}N spectra, the effect of motion is a little more complex. Molecular motion at a similar rate to the RF (typically 60 – 100 kHz) will disrupt the averaging of the RF radiation which causes the decoupling to be less effective and so lines will be broader. Similarly, motion on the order of the MAS rate (typically 10 kHz) can disrupt the refocusing of the magnetisation every rotor period which also causes line broadening. Both types of interference-based broadening can be used to estimate a rate of motion if the extreme narrowed line is measured at a different temperature. There are cases when lines are so broad that they are no longer visible. This is difficult to overcome, since the experimental range of both decoupling power and MAS rate is extremely limited. Usually the best tactic in this instance is to change the temperature to take the rate of molecular motion outside of the interference range.

Lineshapes for quadrupolar nuclei may be dominated by the quadrupolar interaction. This can lead to very broad patterns that are experimentally difficult to record. Deuterium, however, has a particularly small quadrupole moment giving quadrupole coupling constants (C_Q) around 200 kHz, making it particularly amenable to NMR study.

2.4.2.1 Quadrupoles

As stated previously, a nucleus with spin I will have $2I + 1$ orientations each with degenerate energy. The Zeeman effect splits the energy levels equally when placed in a magnetic field. This is given by Equation 2.9, where ω_0 is the splitting, γ is the magnetogyric ratio and $\boldsymbol{B}_0$ is the static field. For spins that are greater than a $\frac{1}{2}$, the first order quadrupolar interaction modifies each spin level which results in the splitting no longer being equal, as shown in Figure 2.4. A single crystal with spin 1 would have two peaks split by $2\omega_\mathrm{Q}$, which is equal to $\frac{3}{4}C_\mathrm{Q}$. In a powder this becomes a Pake doublet due to powder averaging, see

[†]Coherent interactions/processes refer to interactions that are not random so can in principle be reversed. These include all internal interactions, magnetic field inhomogeneities and chemical shift distribution which can be refocused with an echo. Molecular motion is an example of an incoherent process because it is inherently random.

Figure 2.5, with the horn separation equal to $2\omega_Q$ in the absence of motion. ω_Q is given in Equation 2.10 where C_Q is the quadrupolar coupling constant, θ and ϕ give the polar angles between the static magnetic field and the X–D bond, and η_Q is the asymmetry parameter.

$$\omega_0 = \gamma B_0 = 2\pi\nu_{\mathrm{NMR}} \tag{2.9}$$

$$\omega_Q = \frac{3C_Q}{4I(2I-1)} \times \frac{1}{2}(3\cos^2\theta - 1 + \eta_Q \sin^2\theta \cos 2\phi) \tag{2.10}$$

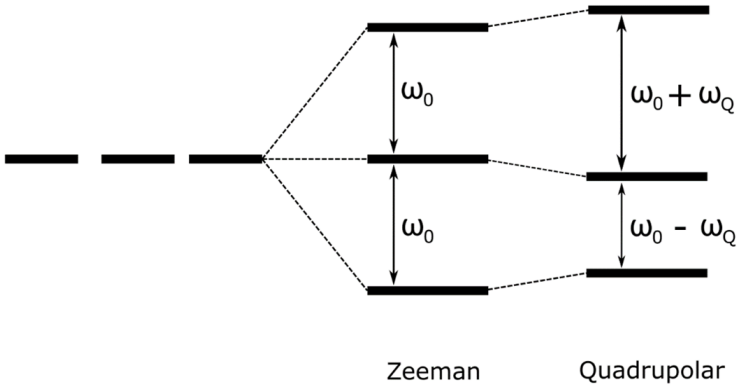

Figure 2.4: Energy level diagram for a spin 1 system. ω_0 is the splitting due to the Zeeman interaction and is given in Equation 2.9. ω_Q is the change of each splitting that is due to the quadrupolar interaction and is given in Equation 2.10.

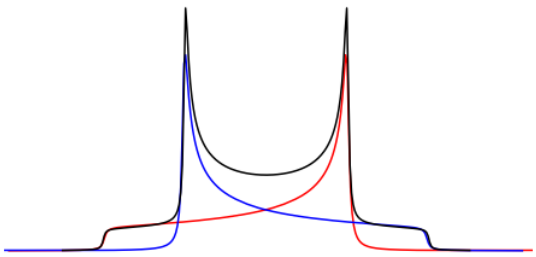

Figure 2.5: A Pake doublet.

Like other interactions, first order quadrupolar coupling has a $3\cos^2\theta - 1$ dependence so can, in principle, be spun out by MAS. However in practice this is unlikely to ever be practically feasible because of the size of the coupling. There is also a second order quadrupolar interaction, which further affects the positions of the energy levels, however it is negligible for nuclei with small quadrupolar coupling constants and so ignored here. The first order quadrupolar coupling is independent of field and the second order term depends inversely on field, which is why larger magnetic fields are advantageous when studying most quadrupolar nuclei.

Quadrupolar lineshapes are directly affected by different types of molecular motion. For deuterium, a spin-1 nucleus, axially symmetric motions such as C_n jumps, where $n \geq 3$, conventional Pake doublets are seen because $\langle \eta_Q \rangle = 0$. For the non-axially symmetric cases, which include C_2 jumps, $\langle \eta_Q \rangle \neq 0$ so the powder patterns are different and hence the Pake doublet is altered. Figure 2.6 shows a typical bandshape for molecules undergoing a 2-site and a 3-site jump.

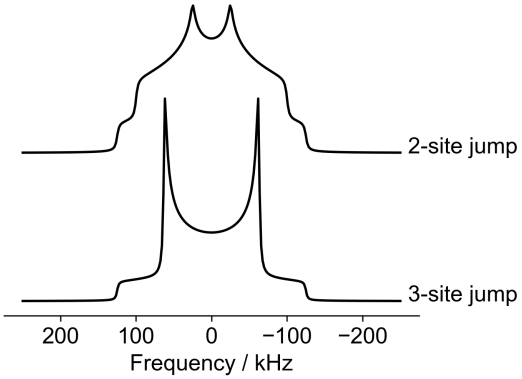

Figure 2.6: Simulated deuterium spectra of a 40 ° 2-site and 3-site jump in the fast limit (10 MHz). Initial parameters: $C_Q = 200$ kHz, $\eta_Q = 0$.

The cone angle[‡] has a significant impact on the spectra. The spectra of a 3-site jump, shown in Figure 2.7a, are identical to the static spectrum reduced by a factor of $(3\cos^2\theta - 1)/2$ where θ is the cone angle. The spectra of 2-site jumps are also scaled by the angle of rotation but this dependence is more complex in cases where $\eta_Q \neq 0$, as shown in Equation 2.10. At cone angles <15 ° the pattern is not greatly affected.

The spectra shown in Figure 2.6 are simulations of molecules in the fast limit. For samples with intermediate motions, distorted spectra are produced. This creates an additional layer of complexity when trying to fit deuterium lineshapes, however in principle it does allow for the determination of both the type and the rate of motion.

[‡]Molecular motion is often described with a cone angle which describes the motion of the C–D bond on a cone. In this model, θ is defined as half the opening angle of the cone.

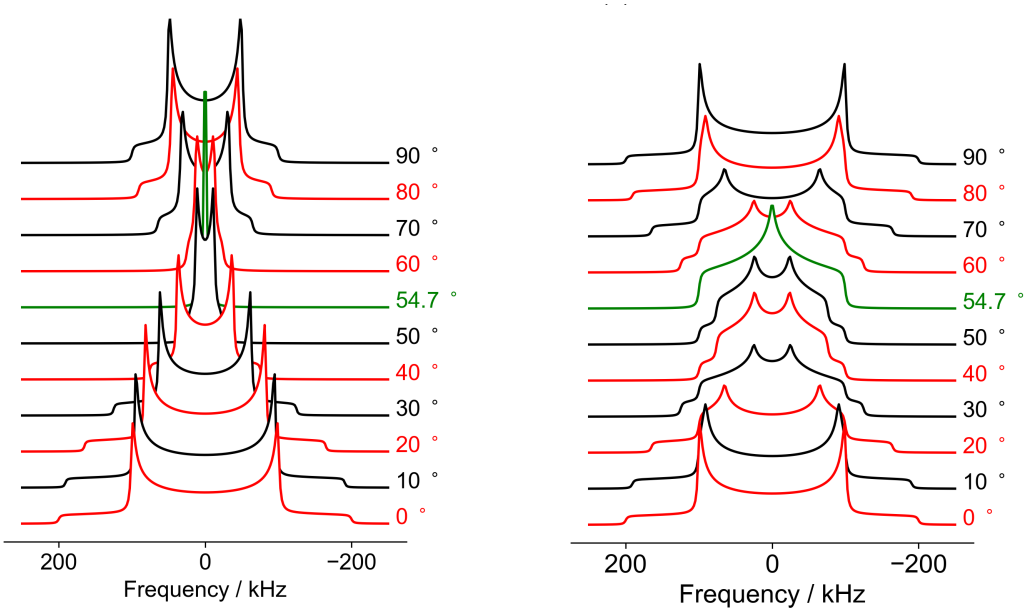

(a) 3-site jump.

(b) 2-site jump.

Figure 2.7: Simulated deuterium spectra with variable cone angles in the fast limit.

Chapter 3

Experimental Techniques

3.1 Temperature Calibration

The temperature of a sample inside a rotor cannot be measured directly. Instead, a thermocouple positioned near the rotor measures the temperature of the outgoing gas stream. However, this may not give an accurate representation of the sample temperature.

To record an accurate temperature of the sample, the temperature of each probe at a given set temperature was calibrated using methanol (180 – 300 K) and ethylene glycol (300 – 380 K). The shift difference was measured between ^{1}H signals and the true temperature calculated from Equations 3.1 and 3.2 which are given in the Bruker VT-calibration manual.

$$T(\mathrm{K}) = 466.4 - 101.24 \times \delta(\mathrm{ppm}) \tag{3.1}$$

$$T(\mathrm{K}) = 403.0 - 29.46\delta(\mathrm{ppm}) - 23.83 \times \delta(\mathrm{ppm})^2 \tag{3.2}$$

Linear regression was used to give the equations for calibrated temperatures, these are given in Equations 3.3 and 3.4 for static samples in the 5 mm static probe on the 400 MHz spectrometer and static samples in the 4 mm MAS probe on the 500 MHz spectrometer respectively.

In all subsequent documentation of temperature, calibrated temperatures have been reported, for temperatures above 380 K values were extrapolated. For spinning samples, there will be additional heat generated from friction. However since both ethylene glycol and methanol are liquids, the sample could not be spun in the probe without leakage. Previous calibrations with lead nitrate have shown an increase of 10(2) K for 10 kHz spinning speed.[16] Hence Equation 3.5 has been used to calibrate experiments taken at 10 kHz MAS spectra on the MAS probe. Uncertainties calculated from error propagation indicate that the calibrated temperatures are accurate to 4 K (ν = 400 MHz, static, static probe), 3 K (ν = 500 MHz, static, MAS probe) and 5 K (ν = 500 MHz, MAS = 10 kHz, MAS probe). Uncertainties may be larger above 380 K due to extrapolation. There will also

be thermal gradients within the rotor with variation increasing with larger rotor sizes and MAS rate. The thermal gradient has been estimated to be up to 4 K for a 4 mm sample spun at 10 kHz.[17] In relaxation measurements, these uncertainties from temperature measurements have not been included in uncertainty of rate calculations for simplicity.

$$T_{\text{calib}}(\text{K}) = 1.461(7) \times T_{\text{set}}(\text{K}) - 134(3)\ \text{K} \tag{3.3}$$
$$\nu = 400\,\text{MHz, Static, Static probe}$$

$$T_{\text{calib}}(\text{K}) = 1.268(5) \times T_{\text{set}}(\text{K}) - 74.1(18)\ \text{K} \tag{3.4}$$
$$\nu = 500\,\text{MHz, Static, MAS probe}$$

$$T_{\text{calib}}(\text{K}) = 1.268 \times T_{\text{set}}(\text{K}) - 64(4)\ \text{K} \tag{3.5}$$
$$\nu = 500\,\text{MHz, MAS} = 10\,\text{kHz, MAS probe}$$

The gradients in Equations 3.3 – 3.5 are unexpectedly large however the calibrations have subsequently been confirmed from known phase transitions of diamantane in Chapter 4 and HMF in Chapter 5.

3.2 Relaxation

3.2.1 Measuring T_1

There are two main methods of recording T_1 relaxation times: saturation recovery and inversion recovery. Saturation recovery uses DE to saturate spins and observe how they return to equilibrium. It is used for recording ^{1}H T_1 relaxation times and can be used for ^{13}C relaxation times if there is sufficient signal with DE. It has the advantage of not requiring a long recycle delay since the spins are saturated at the start of each sequence. Inversion recovery inverts the signal and observes how it returns to equilibrium. It has the advantage of observing a larger signal range, fully negative to fully positive, however the time between pulses must be at least 5 $\times$ T_1 to allow signals to fully relax.

3.2.1.1 Saturation Recovery

Saturation recovery uses multiple 90 ° pulses in quick succession to saturate the spins. They are then left to recover during time τ, after which a 90 ° pulse is applied and the signal recorded, as shown in Figure 3.1a. This is fitted using python to Equation 3.6 (where S_∞ is the maximum signal strength) in order to determine T_1. For proton relaxation, the signal is acquired after a solid echo shown in Figure 3.1b. For ^{13}C relaxation, proton decoupling is used throughout the acquisition time.

$$S(\tau) = S_\infty\left(1 - \exp\left(-\frac{\tau}{T_1}\right)\right) \tag{3.6}$$

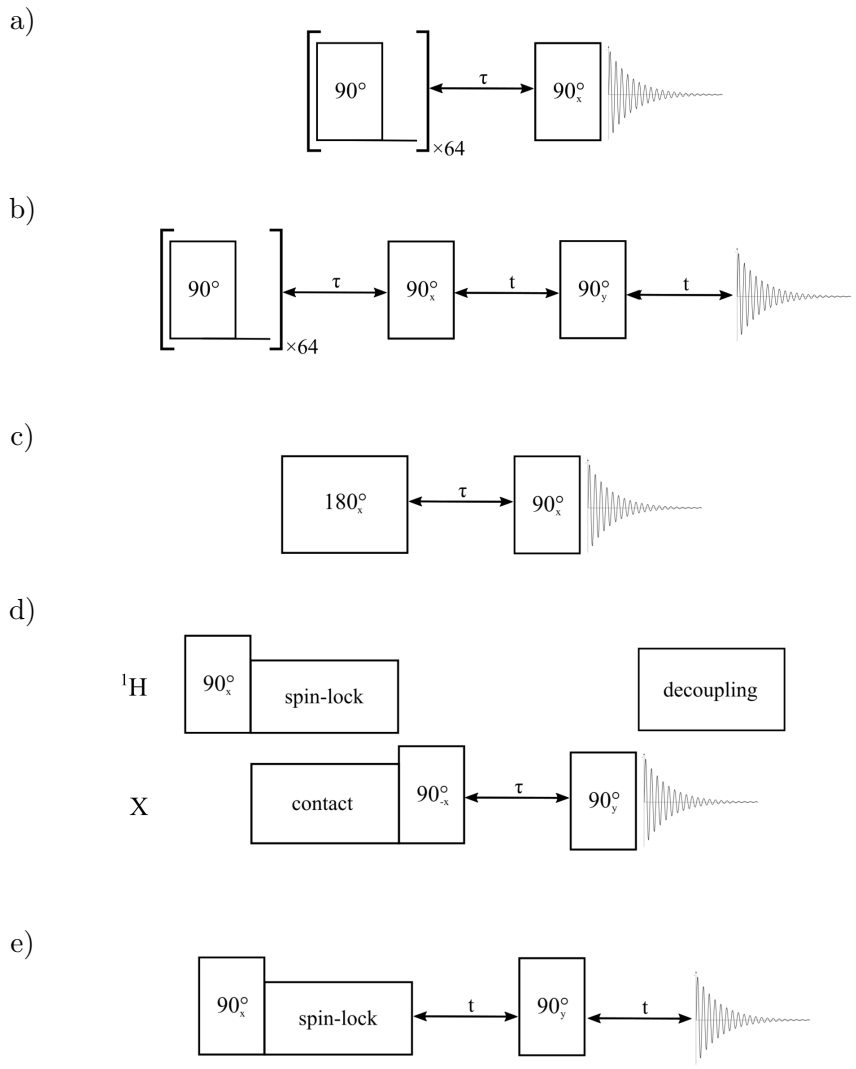

Figure 3.1: Pulse sequences used for measuring relaxation times: a) saturation recovery; b) saturation recovery with a solid echo; c) inversion recovery; d) Torchia; and e) pulse sequence for measuring $T_{1\rho}$ relaxation times by varying the spin-lock pulse duration. Echo delay = t and variable delay = τ.

3.2.1.2 Inversion Recovery

Inversion recovery places the magnetisation in the $-z$ axis with a 180 ° pulse. The magnetisation relaxes during time τ after which a 90 ° pulse is applied and the signal recorded as shown in Figure 3.1c. The recovery is fitted in python to the Equation 3.7. This experiment was used to measure the relaxation of dilute spins through a CP experiment.

$$S(\tau) = S_\infty \left(1 - 2\exp\left(-\frac{\tau}{T_1}\right)\right) \tag{3.7}$$

The Torchia pulse sequence is often used instead and is shown in Figure 3.1d. It results in spectra with only positive peaks which decay according to the Equation 3.8.

$$S(\tau) = S_0 \exp\left(-\frac{\tau}{T_1}\right) \tag{3.8}$$

3.2.2 Measuring $T_{1\rho}$

Proton $T_{1\rho}$ values were acquired by varying the duration of the spin-lock pulse and measuring the signal intensity with a solid echo, as shown in Figure 3.1e. The signal intensity, $S(\tau)$, was plotted as a function of the duration of the spin-lock pulse, τ. The signal decays according to Equation 3.9 where S_0 is the signal at $\tau = 0$.

$$S(\tau) = S_0 \exp\left(-\frac{\tau}{T_{1\rho}}\right) \tag{3.9}$$

There are multiple factors to be considered when choosing an appropriate list of variable delays for T_1 or pulses for $T_{1\rho}$. Firstly, if time permits, and signal-to-noise ratio sufficient, 16 increments are ideal, more is better if trying to fit to two exponentials. Secondly, the longest pulse (or delay) should be at least 3 $\times$ the longest T_1 (or $T_{1\rho}$), so that the majority of the decay or rise is recorded. Lastly, increments should be chosen approximately equally spaced in log(time) such that any sample with multiple decays would be equally well characterised. For example, to measure the relaxation of a sample with a T_1 of 10 s, the following delays would be ideal: 0.10, 0.15, 0.20, 0.30, 0.50, 0.80, 1.1, 1.7, 2.6, 3.8, 5.8, 8.6, 13, 20, 30 and 50 seconds.

3.3 Recycle Delay

NMR is an insensitive technique and so experiments are repeated, and each FID summed, in order to improve signal-to-noise ratio. Signal strength is proportional to the number of repetitions, n, however the noise in the spectrum is random so will increase proportionally with $\sqrt{n}$. Hence increasing the number of repetitions, increases the signal-to-noise ratio.

The time between each experiment is known as the recycle delay and getting it right allows for the maximum signal-to-noise ratio to be acquired in a given period of time. It is determined by T_1 since it is necessary for the bulk magnetisation to return to equilibrium before the next pulse can be applied. Waiting longer between repetitions allows for more signal to be acquired with each repetition but fewer repetitions to be performed in a set period of time. Figure 3.2 shows the balance of these factors. The blue line shows that the longer the recycle delay, the greater the signal acquired per repetition and has been calculated from Equation 3.10. It is typical to wait 5 $\times$ T_1, equivalent to 99.3 % of the maximum, for experiments which require a 'fully' recovered signal. This is balanced by the number of repetitions that can be acquired in a set period of time. The green line shows that the shorter the recycle, the greater the signal acquired because there is a greater number of repetitions per unit time. This increased number of repetitions causes a huge

rise in the noise acquired which initially drops faster than the signal acquired per unit time (red line). This causes a peak in the signal-to-noise ratio when the recycle delay is $1.26 \times T_1$, as shown with the black line.

$$M_z(t) = M_0\left(1 - \exp\left(\frac{-t}{T_1}\right)\right) \tag{3.10}$$

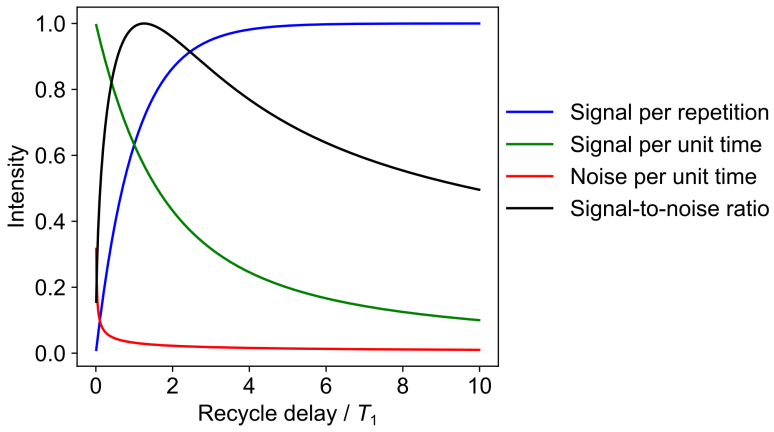

Figure 3.2: Signal intensity for a given recycle delay.

Table 3.1 shows that the maximum signal-to-noise ratio is unexpectedly tolerant to different recycle delays. By using a recycle delay between 1.00 and 1.57 $\times$ T_1, 99 % of the maximum signal-to-noise ratio will be obtained. The third column is useful when the T_1 value is unknown and the recycle delay is determined by running an optimisation experiment i.e. keeping all parameters the same and varying the recycle delay. The maximum signal-to-noise ratio is acquired when the signal strength is 72 % of the maximum. This is only true for experiments where the recycle delay is the rate determining step such as a standard CP spectrum. For experiments with long delays, such as relaxation measurements, there may be signal-to-noise improvements from using a longer recycle delay.

All spectra in this thesis use an 'approximately optimised' recycle delay. This equates to a recycle delay between $1.0 \times T_1$ and $1.6 \times T_1$ if known, or 63 – 79 % of full signal otherwise.

Table 3.1: Signal-to-noise ratio for a given total experiment time.

S/N % of max	**Recycle delay / T_1**	**% Full signal**
90	0.57	43
95	0.73	52
99	1.00	63
100	1.26	72
99	1.57	79
95	2.08	88
90	2.59	92

3.4 Fitting Quadrupolar Lineshapes

As described in Section 2.4.2.1, quadrupolar spectra have characteristic lineshapes for reorientation-type motions which depend on cone angle and the symmetry of the jump. Spectra in the slow or fast limit (<1 kHz or >10 MHz) are easy to directly fit using SOLA in TopSpin, which will fit the spectrum to a C_Q and an η_Q. However, for molecules with intermediate motion, there are no options for fitting the resulting spectrum. Instead, a model must be suggested from which a spectrum is predicted at various rates. The two programs used in this work are EXPRESS[18] and Weblab.[19] These programs predict spectra from Markovian jump dynamics and produce almost identical results but differ in the input requirements as well as their ease of use. Weblab simulates molecular motion based on jumps around a cone which is easy to visualise and only requires the input of a cone angle. EXPRESS works off polar coordinates which is often more complex but can be used more universally to describe any motion.

Chapter 4

Exploring Second Moments as a Tool for Understanding the Dynamics in Diamondoids

Diamondoids are a series of saturated hydrocarbon molecular cages with a structure that can be superimposed onto a 3D diamond lattice. Adamantane is the smallest, consisting of alternating CH and CH_2 groups, forming a single caged unit. Each subsequent diamondoid contains an additional face-fused adamantane unit, as shown in Figure 4.1. The lower diamondoids (adamantane, diamantane and triamantane) have only one isomer, but as they get larger, they have an increasing numbers of isomers. Diamondoids up to 11 caged units have been found in minute quantities in crude oil, with the majority being substituted and unsubstituted adamantanes and diamantanes.[20] The lower diamondoids can also be synthesised through thermodynamically controlled carbocation rearrangement. However this is not possible for larger diamondoids due to the large number of polycyclic precursors which become trapped in local minima.[21]

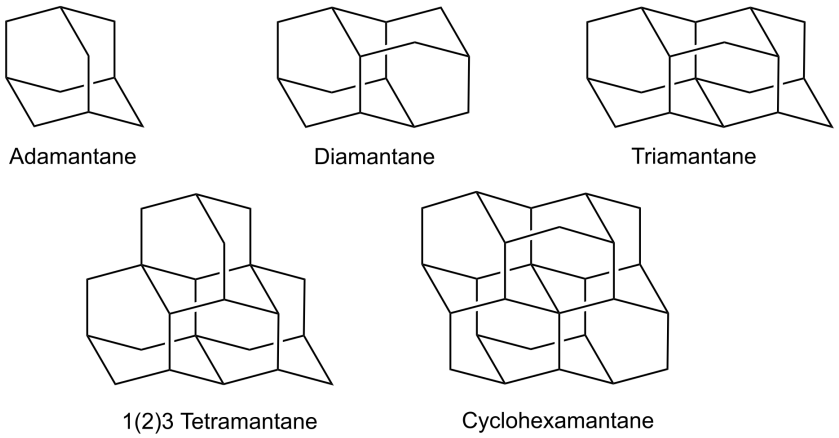

Figure 4.1: Skeletal structures of a selection of diamondoids

Due to their six or more linking groups, molecular stiffness and unique thermal and chemical stability, diamondoids have been used in a variety of fields and in many different ways. For example, in polymers they can improve thermal stability by impeding degradation reactions from either nucleophilic or electrophilic attack.[22] In the field of nanotechnology, just like fullerenes, the multiple linking groups make diamondoids useful molecular building blocks, allowing the construction of 3D structures.[23]

There is also research into diamondoids in the oil and gas industry mainly to reduce their costly impacts. There are many unwanted organic molecules within oil, but most will crack at high temperatures. Diamondoids are uniquely stable and have higher melting points meaning they can precipitate in pipelines leading to problems in the extraction, processing and transport of oil.[24] Conversely, diamondoids have also been used to fingerprint, identify and estimate the degree of oil cracking in underground oil reservoirs.[25,26]

There are several reasons why diamondoids are an interesting class of molecules when studying dynamic molecules. Firstly, they are rigid carbon cages, meaning molecular motions affect the whole molecule. It is unusual for a system to have the whole molecule affected by the same motion and not have analyses complicated by additional sub-group motion, such as methyl group rotation. Secondly, the weak intermolecular interactions allow for significant molecular motions at experimentally accessible temperatures. Adamantane, for example, is used as a reference sample in solid-state NMR, as the rapid isotropic tumbling at room temperature gives very sharp NMR lineshapes. Finally, they are a series of molecules with increasing sizes, which allows methodology to be tested on similar but different test compounds.

This chapter focuses on the dynamics of four diamondoids: diamantane, triamantane, 1(2)3 tetramantane and cyclohexamantane. Diamantane has been previously well characterised,[27] but larger diamondoids have not, largely because they are very difficult molecules to obtain. Only very small quantities of samples were available (approximately 40, 20 and 5 mg of triamantane, 1(2)3 tetramantane and cyclohexamantane respectively) and so the interest is showing how well we can understand these materials based on only milligrams of material. Initially the discussion focuses on how relaxation measurements can be used to understand the nature of the motions as well as giving activation energies and rates of motion. The latter section seeks to determine if the gaps in understanding from relaxation measurements can be filled with data from second moments - a historical method of summarising ^{1}H lineshapes. The methods used to measure a second moment from a spectrum are discussed, before applying the different methods to static ^{1}H lineshapes of each diamondoid. Finally these values are compared with simulated values, calculated based on static and fast rotation about specified axes, to reveal whether the second moments still have utility.

4.1 Background

4.1.1 Second Moments

The linewidths of ^{1}H solid-state spectra are dominated by dipolar couplings between ^{1}H spins. These dipolar couplings between protons are typically very strong, meaning ^{1}H lineshapes are typically broad and featureless. However, this does not mean they are without use. Since molecular motions reduce the effect of dipolar couplings on a spectrum, the ^{1}H linewidth is a direct probe of molecular motion. For a static system, or one with dynamics significantly less than 50 kHz, the ^{1}H lineshape will appear as a classic 'static' pattern – a broad lineshape typically greater than 50 kHz. As molecular motion increases, the dipolar couplings are averaged causing a reduction of the linewidth. At the extreme, a system undergoing isotropic rotation where molecules move relative to one another, the dipolar contribution to linewidth will be reduced to zero. In this instance, the linewidth would be less than a few kHz.

Second moments are a method of describing the lineshape with a single number, typically in Hz^2 but historically in Gauss^2 or G^2. For years second moments were used as the main indicator of molecular motion in solids.[28] They fell out of favour with two major technological improvements, relaxation measurements and alternative nuclei. There are several valid reasons for this: relaxation times are sensitive to a much greater range of motions compared to linewidths and give better insights of motional parameters such as activation energy and correlation times; and alternative nuclei often give dynamic information which was site specific and hence can be used to deduce the type of motion. Under many circumstances these newer methods will be more informative. Nevertheless, second moments do retain some important advantages. The first is that the second moment is dependent on the geometry of motion and hence second moments can be used to verify different models of rotation without ^{2}H labelling.[28] ^{1}H relaxation times will give motional parameters, but will give no information about the type of motion. Other advantages include experimental simplicity: ^{1}H has the highest receptivity of any nucleus so signal-to-noise ratio is high; there is no requirement for CP and there is no MAS; and static probes can often operate over a wider temperature range. It is often not possible to get a full relaxation curve due to temperature restrictions from the equipment or the sample and even with a full relaxation curve, interpreting relaxation times can be difficult (as discussed in Chapter 6).

The challenge associated with second moments can be divided into two areas: determining the second moment of a spectrum and the theoretical calculation. The experimental determination of a second moment from a spectrum is an unexpectedly difficult task. Explanations in the literature can be vague and the calculation of second moments by direct integration of the lineshape is highly unstable. The theoretical calculation is relatively simple for static molecules and involves a pair-wise sum of all the intra and inter ^{1}H – ^{1}H interactions. The challenge arises when determining how these interactions, in particular, the intermolecular interactions, are affected by molecular motions.

As explained, historically second moments are typically quoted in G^2. G is an old unit for magnetic field strength equal to 1×10^{-4} T. Before Fourier transform NMR became the standard, spectra were obtained through continuous wave NMR where the response is measured at various field strengths, measured in G, using a fixed ν_{RF}. Hence old spectra were plotted in terms of G instead of ppm or kHz. In NMR magnetic field strengths and frequencies are often used interchangeably; an 11.7 T magnet will be described as a 500 MHz which technically describes the ^{1}H Larmor frequency at that field. The formula for the conversion is given by Equation 4.1 where ν_{NMR} is the resonance frequency, γ is the magnetogyric ratio and $\boldsymbol{B}_0$ is the field strength.

$$\nu_{NMR} = \frac{\gamma}{2\pi} B_0 \tag{4.1}$$

For ^{1}H:

$$\gamma/(2\pi) = 42.58\,\text{MHz}\,\text{T}^{-1}$$

$1\,\text{G} = 1 \times 10^{-4}\,\text{T}$. Hence:

$$\gamma/(2\pi) = 4.258\,\text{kHz}\,\text{G}^{-1}$$

With magnetic fields, $42.58\,\text{MHz}\,\text{T}^{-1}$ can be used to convert magnetic fields in T to ^{1}H Larmor frequencies in MHz. With ^{1}H second moments, $(4.258\,\text{kHz}\,\text{G}^{-1})^2$ can be used to convert G^2 to kHz^2. In other words:

$$M_2(\text{kHz}^2) = 18.13\,\text{kHz}^2\,\text{G}^{-2} \times M_2(\text{G}^2) \tag{4.2}$$

4.1.2 Diamantane

Diamantane is the second member in the diamondoid series and consists of two face-fused adamantane cages. It belongs to the D_{3d} point group and has one C_3 axis and three equivalent C_2 axes. It was initially called congressane after it was chosen as the congress emblem of the 1963 London IUPAC meeting and attending chemists were challenged to synthesise it. Upon the discovery of further diamondoids, the name was changed to fit into a logical naming sequence. Diamantane is the largest diamondoid which is commercially available. The crystal structure was determined in 1965 by Karle et. al and is shown in Figure 4.2.[29]

As had already been reported with adamantane, diamantane was found to have multiple solid-solid phase transitions below its melting point at 518 K.[30] These were first reported by Clark et. al at 415 K and 447 K[31] from differential scanning calorimetry (DSC) but later revised by Spinnella et. al to 407 K and 440 K.[23] This was confirmed by Jenkins et. al by Raman spectroscopy, as well as reporting a low transition at 35 K.[32] The phases of diamantane are summarised in Table 4.1.

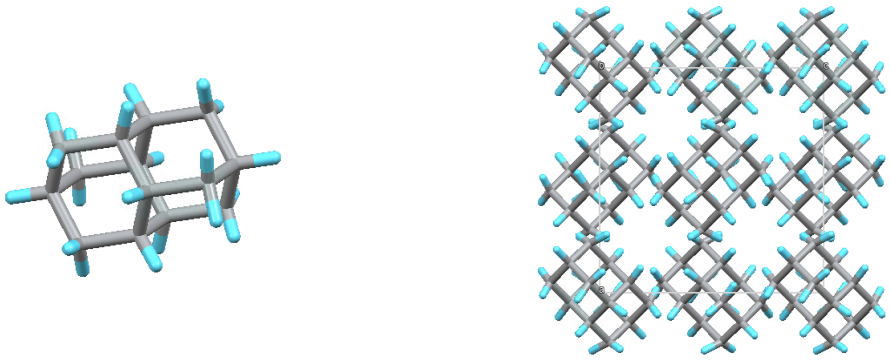

Figure 4.2: Crystal structure of diamantane, refcode CONGRS.[29]

Table 4.1: Phases of diamantane.[23]

Phase	**Temperature range**
IV	Below 35 K
III	35 - 407 K
II	407 - 440 K
I	440 - 518 K

Solid-state NMR data was reported in 1978 by Britcher and Strange.[27] They used static ^{1}H second moments and relaxation times to explore the dynamics of diamantane in phases I, II and III. These results are shown in Figures 4.3 and 4.4.

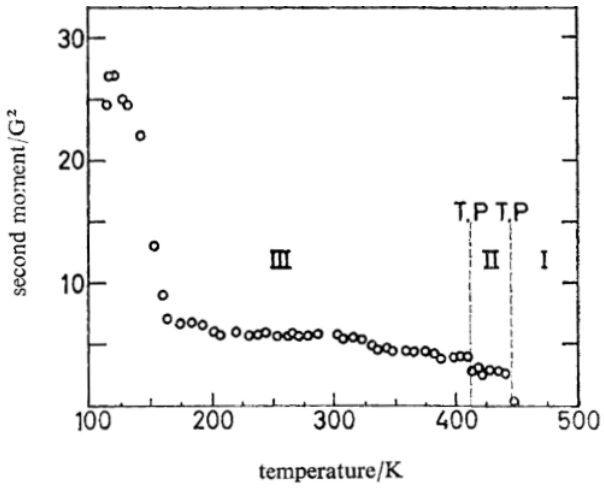

Figure 4.3: Second moment data given in G^2 at 14.3 MHz from Britcher and Strange.[27] TP is the transition point.

Many examples in the literature do not give methods for calculating second moments and most do not give uncertainties on values, however Britcher and Strange did give some information on both counts. Second moments were calculated by fitting the FIDs, with and without a solid echo, to a Gaussian to calculate a second moment (see Section 4.4.1 for more details). They described difficulties with this method due to "the

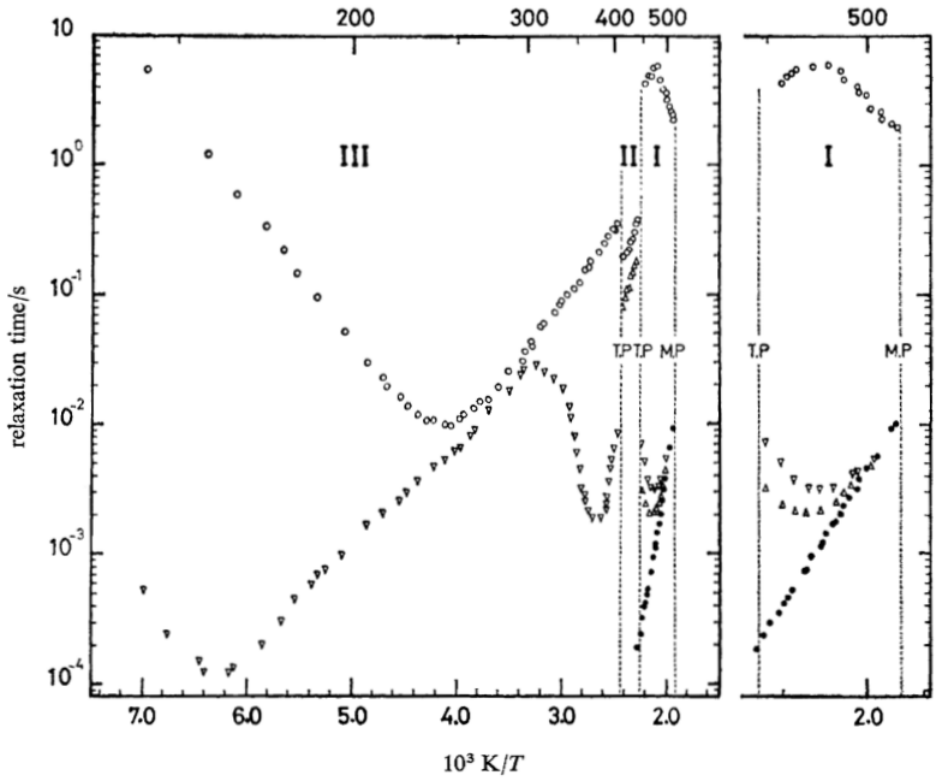

Figure 4.4: ^{1}H relaxation measurements of diamantane: T_1 at 14.3 MHz (○) and $T_{1\rho}$ at 43 kHz (▽) and 31 kHz (△) from Britcher and Strange.[27] T_2 relaxation measurements (•) given in phase I are not discussed here. TP and MP are the transition point and melting point respectively.

effect of higher moments and the fact that the echo peak occurs at a time which is not exactly twice the pulse-to-pulse interval".[27] With this in mind, but without further information given, errors were estimated to be 15 % with a solid echo and 25 % without for their experimental conditions. Given that static ^{1}H lineshapes typically have good signal-to-noise ratio, these error value estimations are large suggesting that absolute values of M_2 are intrinsically difficult to measure robustly. Second moments and their uncertainties reported by Britcher and Strange are summarised in Table 4.2, given in G^2 and converted to kHz^2 for future comparison.

Table 4.2: Second moments of diamantane determined by Britcher and Strange.[27]

Temperature / K	**Phase**	M_2 **/ G^2**	M_2 **/ kHz^2**
95 – 135	III	26.2(6.6)	480(120)
200[a]	III	5.3(8)	96(14)
350[a]	III	4.3(7)	78(13)
409[a]	II	2.7(5)	49(9)
442.5	I	0.54(4)	9.8(7)

[a] Reported the lowest temperature of a plateau region. M_2 given at that temperature.

Britcher and Strange recorded the second moments of diamantane which showed significant drops at each phase transition. Within phase III there were two steep drops indicating the introduction of motions at specific temperatures. Between the drops, plateau regions show steady reductions in second moments indicating an overall increase in motion. Some conclusions were made with confidence: between 95 – 135 K the second moment was consistent with the value for the rigid lattice; and there was no isotropic rotation in phases II and III since the second moments were greater 20 kHz^2. However, by their own admission, conclusions about specific motions were difficult since the estimation of the intermolecular component of second moment was crude. Multiple principal axes of reorientation are proposed including around a space conserving C_3 axis, a perpendicular C_2 axis as well as an 'L' and an 'M' axis, as shown in Figure 4.5. It is suggested that the plateau between 200 – 300 K is due the C_3 rotation. The possible additional plateau at 350 K which "may exist although this is uncertain due to the scatter in the data" is assigned to an 'L' axis rotation which is in effect a wobble about a C_3 axis.[27]

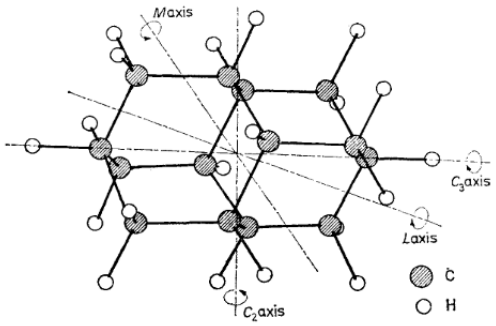

Figure 4.5: Principal axes of rotation given by Britcher and Strange.[27]

^{1}H T_1 and $T_{1\rho}$ relaxation times were also used to analyse the dynamics. Below 300 K, the gradients of both the $\log_{10}$(relaxation time) vs reciprocal temperature plots have the same gradient suggesting that the two relaxation measurements are sensitive to the same motion. Above 300 K, a new relaxation mechanism becomes predominant with the $T_{1\rho}$ relaxation times showing a second minimum at 373 K. The motion associated with this minimum has a much greater activation energy measured to be 94(10) kJ mol^{-1}. They attribute this, along with a small drop in the second moment at 350 K, to a rotation about the 'L' axis.

Conclusions about the motion in phase II were difficult to draw. It appeared that both T_1 and $T_{1\rho}$ relaxation times were affected by the same motion with an activation energy of 55(5) kJ mol^{-1}. It was suggested that this could be the 'L' axis motion with the barrier significantly reduced in the new phase.

Based on the significant reduction of second moments in phase I, it is reasonably assumed that there is diffusion behaviour in this temperature region. Britcher and Strange calculated the mean residence time, τ in this region using T_2 and $T_{1\rho}$ measurements at 43 kHz^2 and 31 kHz^2 and plotted against reciprocal temperature to calculate an activation

energy in this region of 99.7(1) kJ mol^{-1}. This value is very similar to the activation energy found from the $T_{1\rho}$ relaxation in the higher temperature region of phase III. Although not mentioned in the paper, it is possible that the $T_{1\rho}$ above 300 K in phase III is sensitive to the beginning of the diffusion behaviour.

4.1.3 Triamantane

Triamantane is the third member of the diamondoid series and consists of three face-fused adamantane cages. It belongs to the C_{2v} point group and has one C_2 axis and two mirror planes. The crystal structure of triamantane[33] determined by Khusnutdinov et. al is shown in Figure 4.6. The C_2 axis remains in the crystal symmetry.

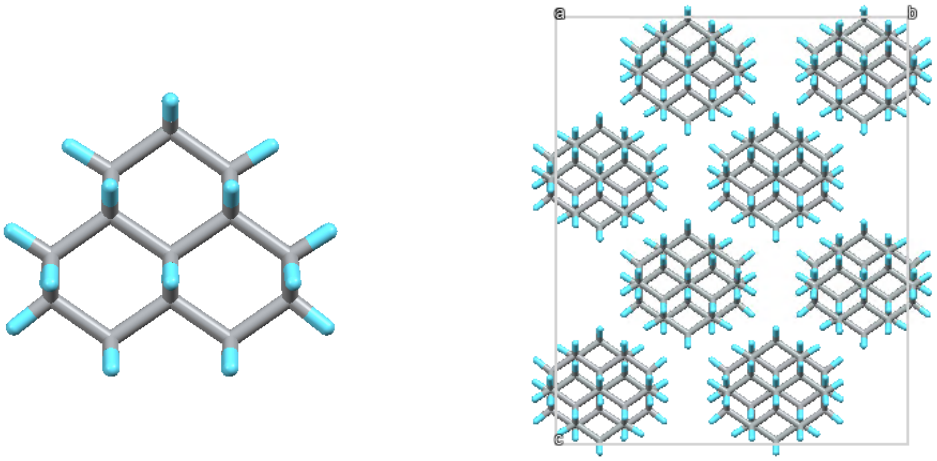

Figure 4.6: Crystal structure of triamantane at 120 K, refcode TRIAMT01.[33]

Solution-state NMR has been reported for triamantane and a ^{13}C spectrum was assigned from homonuclear correlation spectroscopy (COSY) and heteronuclear multiple bond coherence (HMBC).[33,34] There have been no solid-state NMR of triamantane results published. Triamantane was first synthesised in 1966 by Schleyer et. al by an acid catalysed rearrangement of an isomeric precursor.[35] They reported a melting point of 494 K which was confirmed by Burns et. al who also found a solid-solid transition at 428 K.[36] Using X-ray diffraction (XRD) Cernik et. al found a gradual transition from an ordered phase at 273 K to a disordered phase at 303 K which had an increasing proportion of molecules re-orienting about one axis.[37]

4.1.4 1(2)3 Tetramantane

1(2)3 tetramantane is one of the three geometric isomers which consist of four face-fused adamantane cages. It belongs to the C_{3v} point group and has one C_3 axis.

Literature of the higher diamondoids is much more limited due to rarity of samples. Solution-state NMR has been reported and a ^{13}C spectrum has been assigned from COSY and HMBC spectra.[38] There have been no solid-state NMR of 1(2)3 tetramantane results published. The crystal structure of 1(2)3 tetramantane shown in Figure 4.7 was determined using single-crystal X-ray diffraction (SCXRD) by Dmitry Yufit (internal communication).

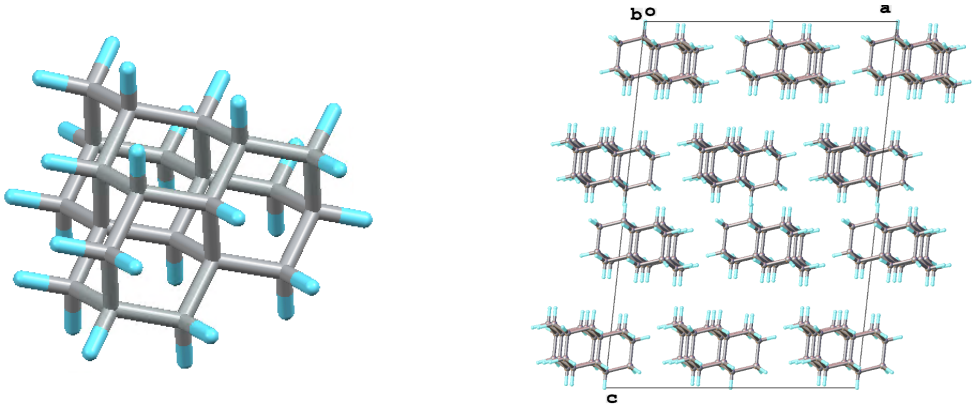

Figure 4.7: Crystal structure of 1(2)3 tetramantane at 120 K, refcode 16srv328.[39]

4.1.5 Cyclohexamantane

Cyclohexamantane is a highly symmetrical, large diamondoid containing six face-fused adamantane cages arranged in a circle. Just like diamantane, cyclohexamantane belongs to the D_{3d} point group and has one C_3 axis and three equivalent C_2 axes. It cannot currently be synthesised and is ultra rare in oil (less than 1 ppb).[40] Due to the monumental number of intermediate structures and precursor molecules that would be formed during the formation of cyclohexamantane in petroleum, it is assumed that its formation would be on the order of billions of years. Based on this kinetic difficulty, it is assumed the only available source ever of cyclohexamantane will be oil.[40] The crystal structure of cyclohexamantane determined by Dahl et al. is shown in Figure 4.8. The C_3 axis remains in the crystal symmetry.

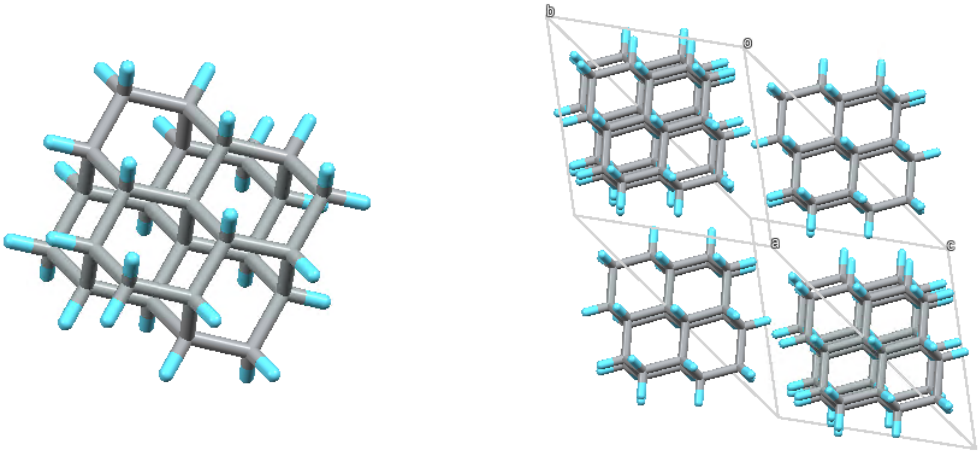

Figure 4.8: Crystal structure of cyclohexamantane at 120 K, refcode UJISAH.[40]

4.2 Experimental Methods

Samples of diamantane, triamantane, 1(2)3 tetramantane and cyclohexamantane were packed into 4 mm zirconia rotors. In contrast to diamantane, which is available commercially, there were extremely limited quantities of triamantane, 1(2)3 tetramantane and cyclohexamantane samples available (approximately 40, 20 and 5 mg respectively). Hence the limited volume of each sample were sealed inside a Kel-F (polychlorotrifluoroethylene) sample insert, before packing into the zirconia rotor. For ^{1}H experiments, the 4 mm zirconia rotors were placed in a 5 mm glass holder, to ensure the filled rotor was in the centre of the coil. The ^{13}C shift scale was referenced with respect to neat tetramethylsilane (TMS) by setting the highest frequency peak of adamantane to 38.5 ppm.

Static ^{1}H spectra and ^{1}H T_1 and $T_{1\rho}$ relaxation measurements were obtained using a Bruker Avance III HD spectrometer operating at 400.17 MHz and a static 5 mm probe. ^{13}C MAS spectra and ^{13}C T_1 relaxation measurements were obtained using a Bruker Avance III HD spectrometer at a frequency of 125.65 MHz using a Bruker 4 mm MAS probe.

^{1}H T_1 relaxation times were measured using a saturation recovery sequence and a solid echo with a 15 µs inter-pulse echo delay. ^{1}H $T_{1\rho}$ relaxation times were measured by varying the spin-lock time and measuring the signal with a solid echo also with a 15 µs inter-pulse echo delay. The ^{13}C T_1 relaxation times of diamantane and 1(2)3 tetramantane were measured using saturation recovery for diamantane and the high temperature phase of 1(2)3 tetramantane and a Torchia sequence for the low temperature phase.[41] The integrated peak areas were plotted as a function of delay time (T_1) or pulse duration ($T_{1\rho}$) and were used to fit to either a single rising exponential (saturation recovery) or decaying exponential ($T_{1\rho}$ measurement and the Torchia sequence).

The diamantane, triamantane, 1(2)3 tetramantane and cyclohexamantane spectra for second moment analysis were recorded using a solid echo with a 15 µs inter-pulse echo delay. Diamantane and 1(2)3 tetramantane spectra were obtained from a saturation

recovery sequence by extracting the most relaxed spectrum with the longest recovery time. Triamantane, 1(2)3 tetramantane and cyclohexamantane showed significant signal from the sample insert. Triamantane spectra were taken with and without inversion recovery (IR) with delays between 0.5 – 1 s in order to approximately null this more rapidly relaxing component. An example spectrum from each plateau region from triamantane (with and without IR) have been selected for methodology determination. The procedures were subsequently applied to diamantane, 1(2)3 tetramantane and cyclohexamantane.

4.3 Relaxation Times and ^{13}C Spectra

^{13}C spectra of diamantane, triamantane, 1(2)3 tetramantane and cyclohexamantane taken at 253 K are shown in Figure 4.9. The ^{13}C linewidth of diamantane is very narrow (full width at half maximum (FWHM) $\approx$ 0.07 ppm / 8 Hz) and the approximately-optimised recycle delay is low (4 s) indicating that diamantane is highly mobile at this temperature. The other diamondoids have wider linewidths (FWHM $\approx$ 0.2 – 0.6 ppm / 25 – 75 Hz) and approximately-optimised recycle delays of 200 s which is typical of static solids.

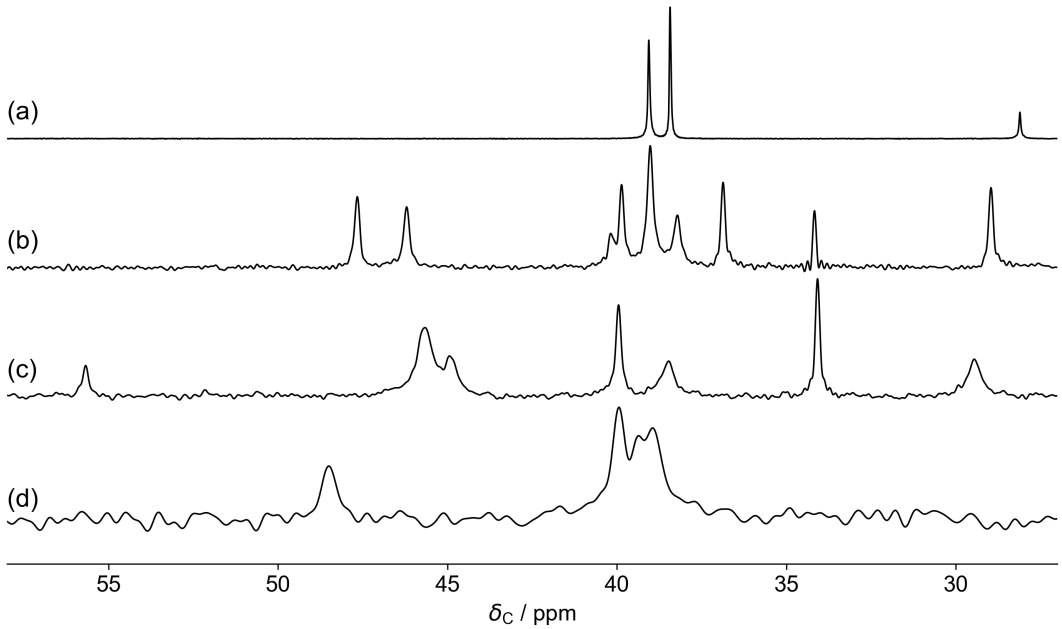

Figure 4.9: ^{13}C CPMAS spectra acquired at 125.65 MHz and 253 K. (a) Diamantane: 16 transients; 4 s recycle delay; MAS rate = 4 kHz. (b) Triamantane: 16 transients; 120 s recycle delay; MAS rate = 10 kHz. (c) 1(2)3 tetramantane: 16 transients; 120 s recycle delay; MAS rate = 10 kHz. (d) Cyclohexamantane: 1536 transients; 120 s recycle delay; MAS rate = 10 kHz. (a), (b) and (c) taken from reference 42.

^{13}C assignments are given in Table 4.3 using the numbering given in the skeletal structures in Figure 4.10. For details about assignments of diamantane, triamantane and 1(2)3 tetramantane see reference 42. For details of the cyclohexamantane assignment see Section 4.3.1.

Table 4.3: Diamondoid ^{13}C assignments of spectra at 253 K. For each the left column shows chemical shifts / ppm and the right column shows carbon assignment based on numbering given in Figure 4.10 and multiplicity.

Diamantane		**Triamantane**		**1(2)3 tetramantane**		**Cyclohexamantane**	
39.1	2 (CH_2)	47.7	6 (CH)	55.7	1 (CH)	48.6	2 (CH)
38.4	3 (CH)	46.2	2 (CH_2)	45.6	5 (CH)	40.0	3 & 3X (CH)
28.1	1 (CH)	40.2	8 (CH_2)	45.1	3 (CH_2)	39.3	1 (Q)
		39.9	5 / 5X (CH)	40.1	6 (CH)	38.9	4 (CH_2)
		39.0	5X / 5 (CH)	38.6	7 (CH_2)		
		39.0	4 / 4X (CH_2)	34.2	2 (Q)		
		38.2	4X / 4 (CH_2)	29.6	4 (CH)		
		36.9	7 (CH)				
		34.2	1 (Q)				
		29.0	3 (CH)				

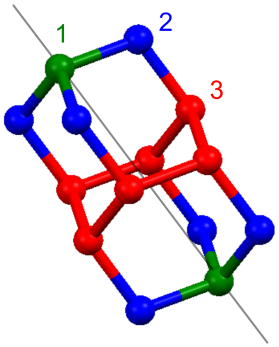

(a) Diamantane with C_3 axis.

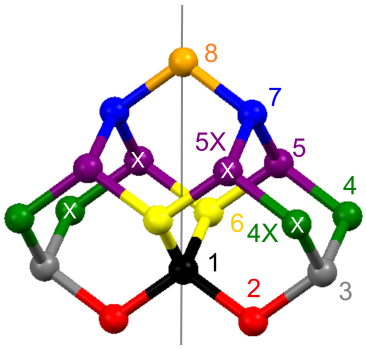

(b) Triamantane with C_2 axis.

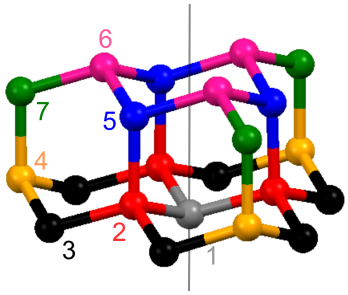

(c) 1(2)3 tetramantane with C_3 axis.

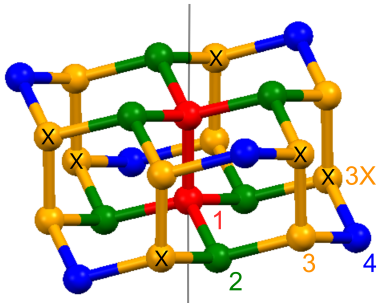

(d) Cyclohexamantane with C_3 axis.

Figure 4.10: Diamondoid ^{13}C assignments with principle rotation axes of symmetry shown. Colours indicate molecular symmetry. X indicates atoms that are not strictly related by symmetry in the crystal structure.

4.3.1 Cyclohexamantane

The spectrum given in Figure 4.9 is the first reported solid-state spectrum of cyclohexamantane. Despite over 51 h accumulation time, the signal-to-noise is low reflecting the ultra-low sample volume (approximately 5 mg). The solution-state NMR spectrum, reported by Dahl et. al, had three resonances at 47.34, 38.58, 37.81 ppm which were assigned to carbon 2, 4 and 3 respectively.[40] Using the solution assignment, the assignment is given and recorded in Table 4.3. The signal-to-noise in the spectrum is low, hence the presence of a weak peak that is indistinguishable from the noise can not be ruled out.

Sample volume was too small to attempt dynamic studies. It is possible to infer that cyclohexamantane is static at 253 K since, as stated above, the width of the resonances in the ^{13}C spectrum and the approximately-optimised recycle delay is typical of static solids.

4.3.2 Diamantane

^{1}H T_1 and $T_{1\rho}$ relaxation times are given Figure 4.11. The raw data is taken from reference 42 however the data has been re-analysed. For the $T_{1\rho}$ relaxation times, the whole of phase III has been fitted simultaneously to two motions with the same ν_1. As described in more detail in Chapter 5, this simultaneous fitting significantly changes the fitted parameters and gives the most accurate values.

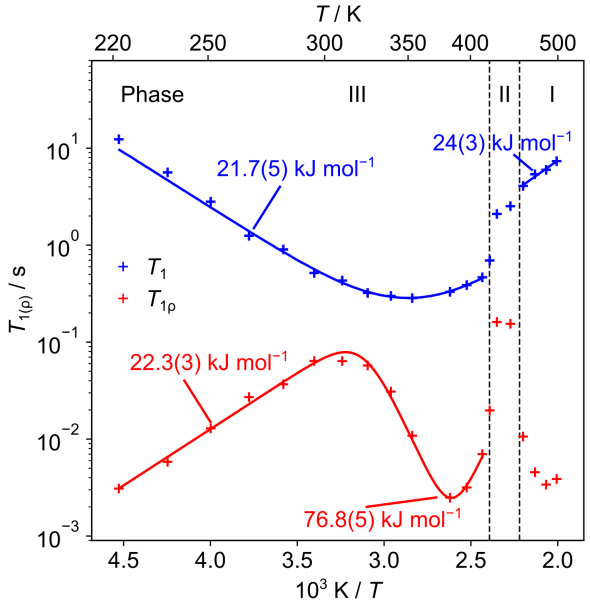

Figure 4.11: ^{1}H T_1 at 400.17 MHz (blue) and $T_{1\rho}$ at 50 kHz (red) relaxation time constants of diamantane as a function of temperature. Error bars are not shown as they are of a similar magnitude to the size of symbols used. $T_{1\rho}$ data fitted to two motions simultaneously. Data from reference 42.

The results obtained are very consistent with the Britcher and Strange paper.[27] The activation energies, E_a, derived from T_1 and $T_{1\rho}$ in phase III are in excellent agreement (21.7(5) kJ mol^{-1} and 22.3(3) kJ mol^{-1}), and in reasonable agreement with the results of

Britcher and Strange (20.4(4) kJ mol^{-1}). As noted before, a new relaxation mechanism becomes predominant above 320 K. This was also in reasonable agreement with Britcher and Strange (76.8(5) kJ mol^{-1} and 94(10) kJ mol^{-1}). The T_1 fitting in phase I could be a continuation of the same motion measured in phase III, with a slightly altered rate in the higher phase. Relaxation measurements in phase II are unreliable as the material was changing rapidly in this relatively small temperature region.

The ^{13}C T_1 relaxation times are shown in Figure 4.12 and the phase III fits are shown in Table 4.4. As expected for a rigid molecule, each carbon site fits to the same E_a and $\log_{10}(\tau_0)$, within the uncertainty. The parameter $\log_{10}(A$ / Hz) is a scaling constant and not expected to be consistent between fits. It is clear from the remarkably similar fitted parameters, that ^{13}C T_1 and ^{1}H T_1 and the ^{1}H $T_{1\rho}$ (below 270 K) are all sensitive to the same fast motion which is around 30 MHz at 250 K and 1500 MHz at 400 K.

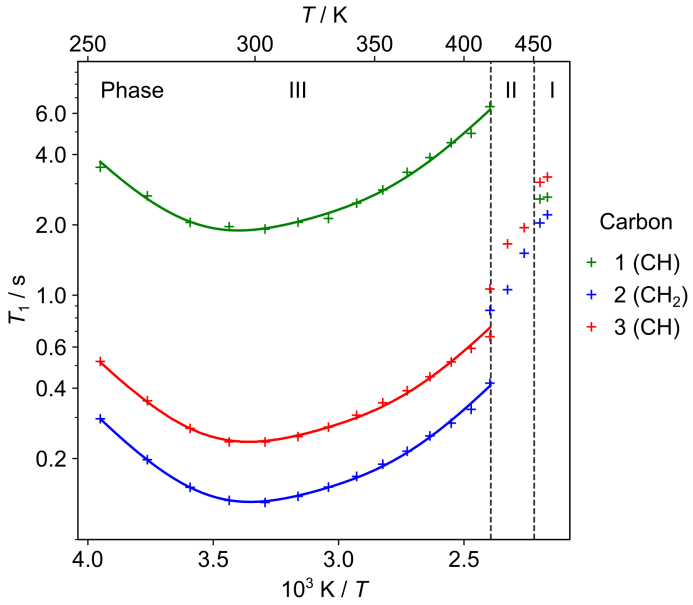

Figure 4.12: ^{13}C T_1 relaxation times of each ^{13}C site of diamantane at 125.65 MHz and MAS rate of 10 kHz. Curves were fitted to an Arrhenius model with fitted values given in Table 4.4. Data and fits from reference 42.

Table 4.4: Fitted values of the ^{13}C T_1 relaxation times in Phase III.

	E_a / kJ mol^{-1}	$\log_{10}(\tau_0$ / s)	$\log_{10}(A$ / Hz)
Carbon 1 (28 ppm)	21.4(4)	−12.79(7)	8.048(6)
Carbon 2 (39 ppm)	21.96(19)	−12.85(4)	9.209(3)
Carbon 3 (38 ppm)	21.7(3)	−12.80(5)	8.952(4)

The ^{13}C relaxation also provides direct evidence of a C_3 rotation. As explained in Section 2.2, ^{13}C T_1 relaxation of alkyl carbons is controlled by ^{13}C−^{1}H dipolar interactions. For a molecule undergoing isotropic motion, it is expected that a carbon with more attached protons would relax faster than one with fewer. Since molecular motions modify

the $^{13}C-^{1}H$ dipolar interaction, a carbon with a C–H bond parallel to the rotation axis will relax more slowly than a carbon with a non-parallel C–H bond where the orientation changes relative to the field changes with the molecular motion. In phase III, carbon 1 relaxes much more slowly than carbon 2 and 3 which, as explained above, is strong evidence that the fast motion observed by the relaxation is a C_3 rotation about the axis which runs through the C–H bonds on carbon 1. The C–H bonds of carbon 2 and 3 are not pointing along the C_3 axis and hence they relax more quickly than carbon 1. Carbon 1 relaxation is likely driven by the longer CH couplings, hence the relaxation has the same temperature dependence as carbons 2 and 3.

In phase I, relaxation times are much more similar, with the CH_2 relaxing the fastest. This is consistent with isotropic motion since there is no specific direction of motion so no carbon relaxes particularly slowly. As with the ^{1}H relaxation data, phase II was difficult to draw a conclusion.

^{13}C spectra varied slightly as a function of temperature. Above 373 K, there was broadening of the carbon 1 resonance, as shown in Figure 4.13, which could indicate the presence of further motion on the 10s of kHz timescale. This would be consistent with the additional motion seen in the ^{1}H $T_{1\rho}$ relaxation.

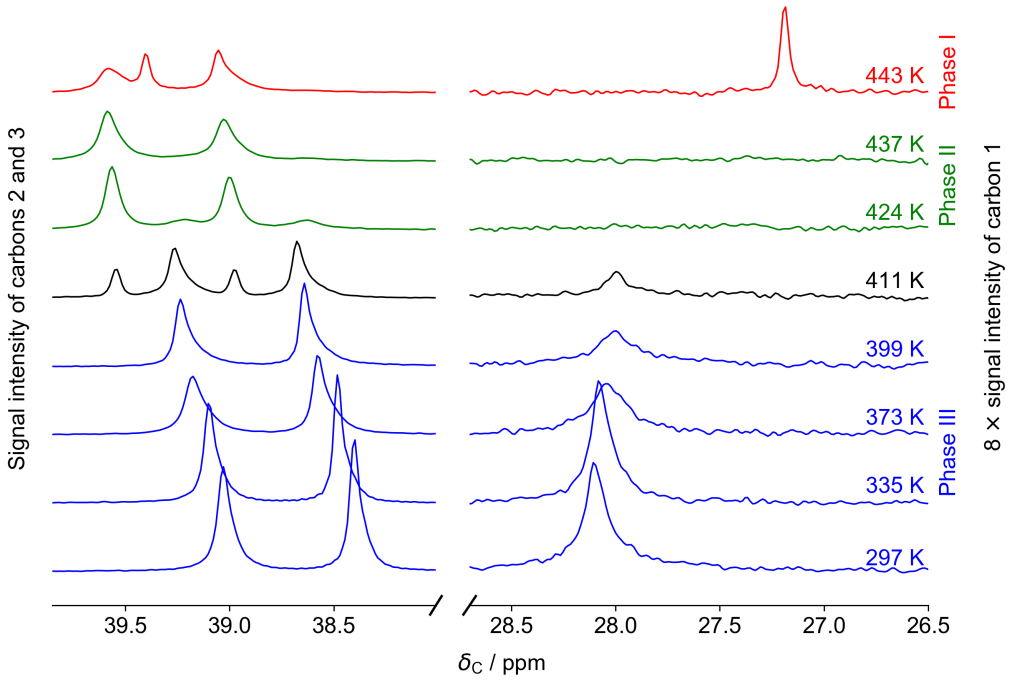

Figure 4.13: DE spectra of diamantane at 125.65 MHz. Recorded with 16 transients and a MAS rate of 4 kHz. Data from reference 42.

4.3.3 Triamantane

Well-resolved ^{13}C CP spectra of triamantane could only be obtained up to 278 K. Above this temperature, signals became broader as shown in Figure 4.14, which also shows that between 300 – 400 K, a ^{13}C spectrum of triamantane could not be obtained. Above the phase transition at 434 K (and to a lesser extent up to 20 K below the phase transition), DE spectra could be obtained. These spectra had the hallmarks of being a highly mobile system: the linewidth was narrow at 0.04 ppm (5 Hz) and had an approximately-optimised recycle delay of 5 s.

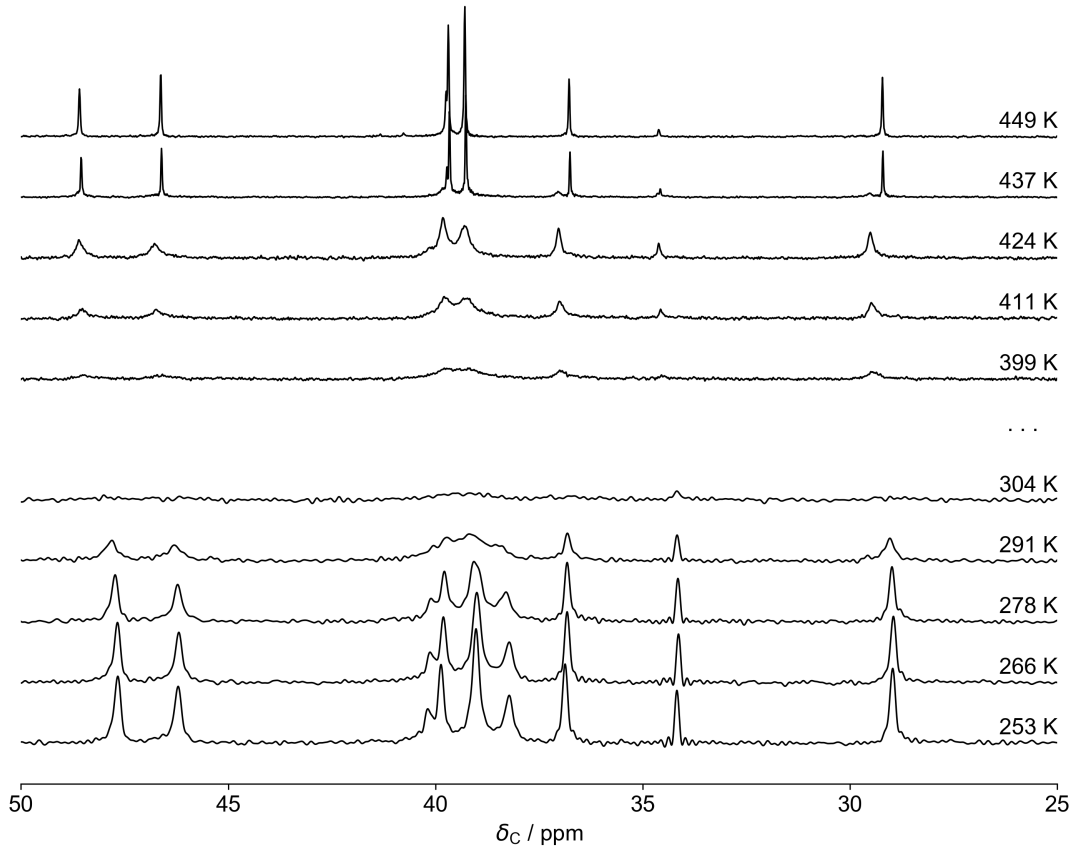

Figure 4.14: ^{13}C spectra of triamantane acquired at 125.65 MHz. The top five spectra are recorded using DE with 128 transients, a 5 s recycle delay and MAS rate = 4 kHz. The lower five spectra are recorded with CP using a 500 µs contact time, 16 transients, a 200 s recycle delay and MAS rate = 10 kHz. Data from reference 42.

Figure 4.15 gives the ^{1}H T_1 and $T_{1\rho}$ relaxation times of triamantane at 400.14 MHz and 50 kHz respectively. Fitting the full $T_{1\rho}$ curve gives the following motional parameters: $E_a = 54.3(17)\,\mathrm{kJ\,mol^{-1}}$ and $\log_{10}(\tau_0\ /\ \mathrm{s}) = -14.1(3)$. This indicates the presence of a motion with a rate ranging from 1 kHz – 3 MHz between 275 – 410 K. This is fully compatible with the T_1 data which is starting to detect a motion on the MHz time scale above 300 K with $E_a = 54.7(6)\,\mathrm{kJ\,mol^{-1}}$, i.e. as with diamantane, both ^{1}H relaxation types are picking up the same molecular motion.

The $T_{1\rho}$ data can help explain the difficulty obtaining ^{13}C signal in two ways. Firstly it shows that there is a motion around 10s of kHz with rates of motion calculated to be 10 – 100 kHz between 305 – 340 K. When there is molecular motion on the order of the MAS rate or the decoupling, there can be an interference, leading to broadening signals, as described in Section 2.4.2. Additionally, $T_{1\rho}$ times are very short: a minimum of 200 µs at 335 K and below 1000 µs between 300 – 380 K. A low ^{1}H $T_{1\rho}$ will reduce the ability to transfer magnetisation during the spin-lock period of CP. Both factors can reduce signal and are ultimately determined by molecular motion around 10s of kHz.

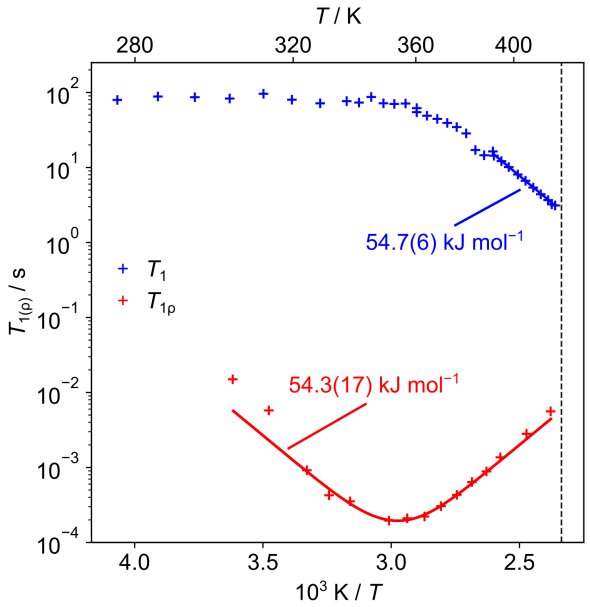

Figure 4.15: ^{1}H T_1 at 400.17 MHz (blue) and $T_{1\rho}$ at 50 kHz (red) relaxation time constants of triamantane as a function of temperature. $T_{1\rho}$ curve fits to relaxation model to give the following motional parameters: $E_a = 54.3(17)\,\mathrm{kJ\,mol^{-1}}$ and $\log_{10}(\tau_0 \,/\, \mathrm{s}) = -14.1(3)$. T_1 data taken by Jack Brash.[43] Error bars are not shown as they are of a similar magnitude to the size of symbols used.

Recording a robust set of ^{13}C T_1 relaxation times was difficult due to the lack of measurable ^{13}C signal between 300 – 400 K and unfavourable experimental parameters outside that temperature range, such as long ^{1}H T_1 relaxation below 300 K. However, ^{13}C relaxation times may not have provided any information on the geometry of the dynamics in this case since there are no C–H bond vectors parallel to any axis or pseudo-axis of symmetry (for axes see Figure 4.29 on page 62).

4.3.4 1(2)3 Tetramantane

^{1}H T_1 and $T_{1\rho}$ relaxation times are given in Figure 4.16 with activation energies of the linear sections displayed on the figure. The activation energies obtained, from T_1 relaxation times, above and below the phase transition at 375 K are consistent ($\approx 21.6(6)$ kJ mol^{-1}), which may indicate sensitivity to the same motion but with a sudden increase in rate above the phase transition; the sign of the gradients are consistent with this. However without rate information from relaxation curves it is difficult to confirm. Above the phase transition, $T_{1\rho}$ relaxation times were difficult to measure as they were significantly longer than the safe limit of approximately 50 ms.

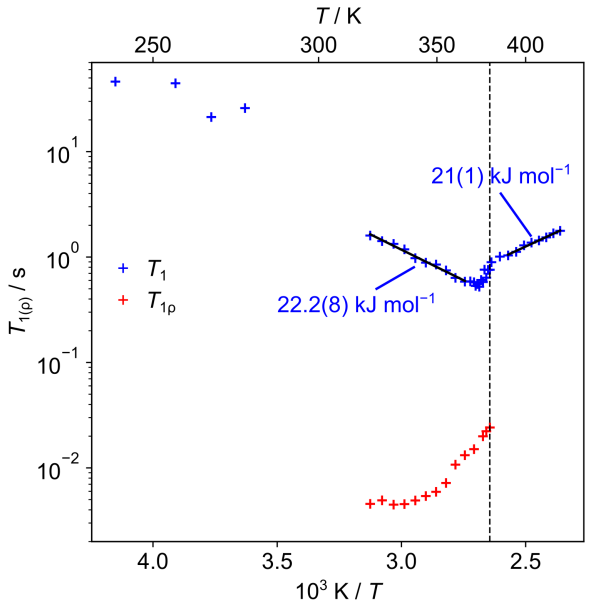

Figure 4.16: ^{1}H T_1 (blue) and $T_{1\rho}$(red) relaxation times of 1(2)3 tetramantane at 400.17 MHz. Data taken by Jack Brash.[43] Activation energies of linear T_1 regions are given.

As shown in Figure 4.17, the ^{13}C spectra of 1(2)3 tetramantane are not observable at 285 K which, as with triamantane, likely indicates the presence of a motion on the 10s of kHz timescale around this temperature. However, unlike triamantane, signal quality was reduced over only 40 K (265 – 305 K) meaning trends in ^{13}C relaxation times could be seen above 310 K.

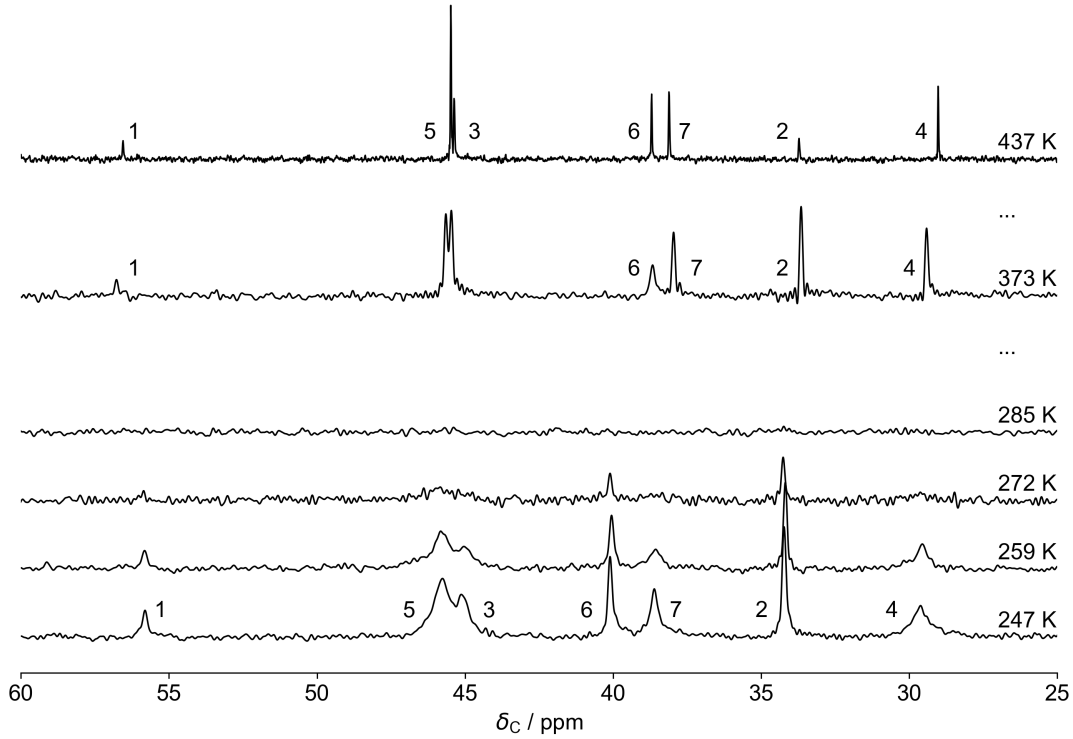

Figure 4.17: ^{13}C spectra of 1(2)3 tetramantane acquired at 125.65 MHz. 437 K spectrum recorded by DE and a 6 s recycle delay and MAS rate = 4 kHz. Lower five spectra recorded with CP and MAS rate = 10 kHz. 373 K used a 6 s recycle delay and the others used a 70 s recycle delay. Data from reference 42.

Figure 4.18 shows the ^{13}C T_1 relaxation times of 1(2)3 tetramantane. Activation energies from individual carbon sites are given in Table 4.5 however caution should be used since the data is not as clean as the diamantane equivalent due to significantly lower signal strength. The data does however provide convincing evidence about the type of motion present. Above the phase transition, the relaxation times were highly dependent on the nature of the carbon i.e. the quaternary ($\curlyvee$) relaxed much more slowly than the methine carbons ($\times$) which relaxed more slowly than the methylene carbons (+). As with the diamantane data, this indicates that the molecule is undergoing isotropic rotation. The situation is different below the phase transition, where carbons with C–H bonds pointing parallel to the C_3 axis (lime green) relax more slowly than those with ^{1}H atoms pointing non-parallel (pink).

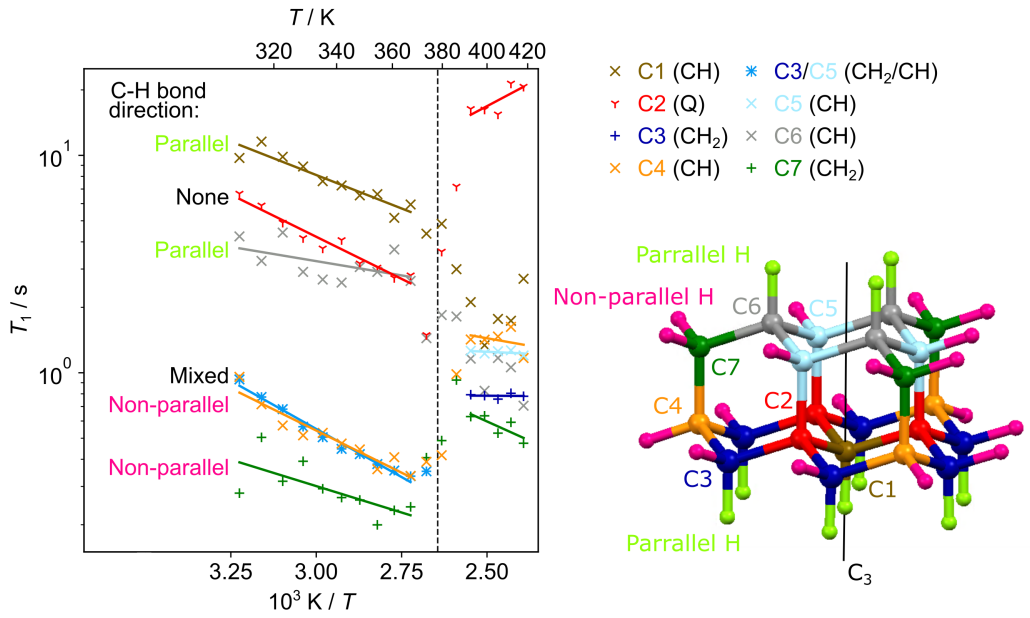

Figure 4.18: ^{13}C T_1 relaxation times of 1(2)3 tetramantane at 125.65 MHz. Below the phase transition a Torchia sequence was used with time delays between 0.01 – 20.24 s used in 16 steps with 64 transients in each and a recycle delay of 8 s. Above the phase transition saturation recovery was used with a saturation train of 64 pulses. Each temperature had recovery times from 0.01 – 48 s in 16 increments with 32 transients in each. Activation energies are given in Table 4.5. Note that below the phase transition, the values associated with carbons 3 and 5 are plotted as one (mid-blue) due to significant peak overlap. Above the phase transition these peaks were resolved and hence were plotted separately (dark blue and cyan). Markers indicate the nature of the carbon: ϒ = quaternary, × = CH, + = CH_2, and ✳ = one peak associated with multiple carbons.

Table 4.5: Activation energies of each carbon in 1(2)3 tetramantane from the ^{13}C relaxation given in Figure 4.18 below the phase transition.

Carbon	E_a / kJ mol^{-1}
1	11.7(15)
2	14.8(12)
3/5	16.9(8)
4	14.9(17)
6	5(3)
7	9(3)
Average[a]	15(2)

[a] Excluding carbon 6 and 7 due to larger standard error.

4.3.5 Relaxation Summary

Full ^{1}H and ^{13}C T_1 and ^{1}H $T_{1\rho}$ relaxation times of diamantane could be measured and this gave good insight into both the rates and types of motion present. As summarised in Table 4.6 there is remarkable consistency of the fitted motional parameters in the low temperature phase giving $E_a = 21.7(5)\,\mathrm{kJ\,mol^{-1}}$. The ^{13}C T_1 relaxation showed that this motion is a C_3 rotation. The ^{1}H $T_{1\rho}$ relaxation times were sensitive to an additional higher-energy motion above 320 K. Previous literature attributed this to an 'L'-type rotation, but it could be the start of molecules self diffusing.

In contrast, it is not possible to get a complete picture of the dynamics of triamantane through relaxation. ^{1}H $T_{1\rho}$ relaxation showed that there was a motion on the 10s kHz timescale with $E_a = 54.3(17)\,\mathrm{kJ\,mol^{-1}}$, however there is no evidence relating to the type of motion present.

1(2)3 tetramantane also has relaxation times which give an indication of activation energies, although there was no relaxation minimum meaning exact rates could not be obtained. However, ^{13}C relaxation did show that there was a C_3-type motion below the phase transition.

Table 4.6: Calculated activation energies of each diamondoid by relaxation type over specific temperature ranges.

Sample	**Temperature range / K**	**Relaxation type**	E_a / **kJ mol^{-1}**	**log$_{10}$(τ_0 / s)**
Diamantane	250 – 410	^{13}C T_1	21.1(4)	−12.76(6)
		^{1}H T_1	21.7(5)	−12.85(8)
		^{1}H $T_{1\rho}$	22.3(3) 76.8(5)	- −15.97(7)
	450 – 490	^{1}H T_1	24(3)	-
Triamantane	275 – 420	^{1}H $T_{1\rho}$	54.3(17)	−14.1(3)
	385 – 425	^{1}H T_1	54.7(6)	-
1(2)3 tetramantane	310 – 370	^{13}C T_1	15(2)	-
		^{1}H T_1	22.2(8)	-
	390 – 425	^{1}H T_1	21(1)	-

4.4 Second Moments

The following is based on the article: 'Revisiting the Van Vleck second moment for characterizing molecular motion in organic solids'.[44] New methodology has been developed by Simone Sturniolo and Paul Hodgkinson for simulating second moments of molecules undergoing fast motion.

Section 4.3 has shown how relaxation measurements can be used to determine not only motional parameters, but also indicate the types of motion present. It has also shown that there are circumstances where ^{13}C data is unattainable, for example if there is interference between the molecular motion and MAS, or if low signal-to-noise ratio makes measurements impractical. The purpose of this section is to investigate second moments from a modern perspective and investigate if they can be used to corroborate the information from relaxation or, ideally, extend understanding. In the context of diamondoids specifically, the aim is discover the nature of the motion in triamantane. Initially the focus of this section is on how second moments are measured from spectra with the various different methods discussed using triamantane spectra and FIDs as examples. Then the second moments of each diamondoid are compared to calculations from simulations to ascertain likely motions of the diamondoids within each temperature range.

4.4.1 Quantification of Second Moments

Second moment experiments were common in the early days of NMR before MAS and alternative nuclei measurements became the norm. In the literature there is often little explanation of how they are calculated and such explanations are often shrouded in old fashioned terms and techniques. Determining second moments from experimental spectra is not as simple as it may seem. There are multiple methods used within the literature and each method has specific difficulties which lead to either systematic errors or sensitivity to the chosen fitting/integration range. The methods evaluated below are:

The 'Gaussian' Method

The simplest method involves fitting a spectrum, $S(\nu)$, to a Gaussian:

$$S(\nu) = A \exp\left(-\frac{(\nu-\nu_0)^2}{2\sigma^2}\right) \tag{4.3}$$

where $S(\nu_0)$ is the centre of the lineshape, and A is an arbitrary intensity factor and $M_2 = \sigma^2$.[45] For example, this approach has been used to fit ^{1}H linewidths under MAS to second moments,[46] but is only applicable when the lineshape has a strong Gaussian character. It has been found that spectra fit well to a Gaussian when dynamics are present but not isotropic motion. Examples of diamantane and triamantane spectra in an intermediate temperature are shown in Figure 4.19. When samples were static, or

rotating near isotropically or showing self-diffusion character, spectra fitted less well to a Gaussian as shown in Figure 4.20. Spectra of molecules undergoing isotropic motion or self-diffusion show significant Lorentzian character where the signal decay is exponential and dominated by relaxation.

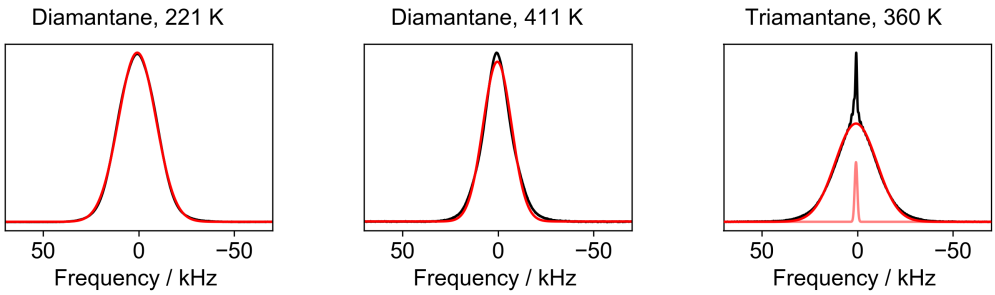

Figure 4.19: Intermediate temperature static ^{1}H spectra (black) fitting well to Gaussians (red/pink). Diamantane at 221 K and 411 K fitted to one Gaussian and triamantane at 360 K fitted to two Gaussians to account for the narrow signal from the insert.

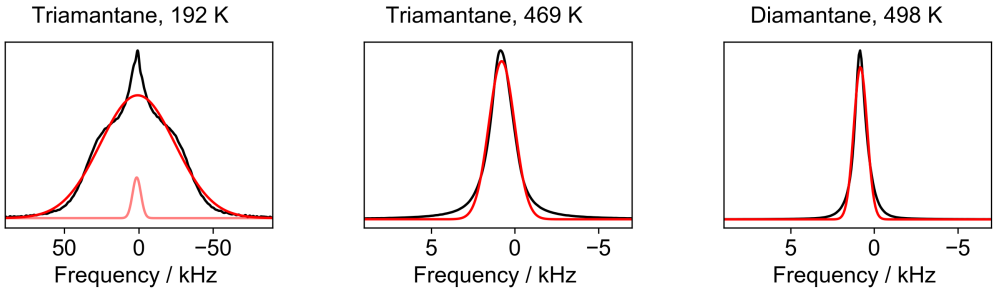

Figure 4.20: Low and high temperature static ^{1}H spectra (black) fitted poorly to Gaussians (red/pink). Triamantane at 192 K fitted to two Gaussians to account to the narrow signal from the insert and diamantane at 498 K and triamantane at 469 K fitted to one Gaussian.

The 'Gaussian' method for FIDs

A related alternative is to fit the time-domain signal, $A(t)$, to a Gaussian:

$$A(t) = A_0 \exp\left(-\frac{(t-t_0)^2}{2{\sigma_t}^2}\right) \tag{4.4}$$

where $A(t_0)$ is the echo peak, and A_0 is an arbitrary intensity factor and $M_2 = (2\pi\sigma)^{-2}$. As before, this method is only applicable when the lineshape has a strong Gaussian character. Fitting in the time domain may be able to 'filter out' narrow signal by fitting only the initial decay and is less affected by imperfect baselines. This approach was seen in several earlier studies including the diamantane system in Britcher and Strange.[27]

The 'Integral' Method

For spectra which are non-Gaussian, one option for determining the second moment is to integrate the spectrum directly:

$$M_2 = \frac{\int_{-\infty}^{\infty} S(\nu)(\nu - \nu_0)^2 \, d\nu}{\int_{-\infty}^{\infty} S(\nu) \, d\nu} \tag{4.5}$$

This approach is applicable generally and has been used, for example, in recent studies using second moments on complex materials,[47] but is extremely sensitive to the choice of integration limits and to spectral noise in the outer parts of the spectrum.

This method is very sensitive to the insert signal, not directly through the 'second moment' part of Equation 4.5 or the numerator (since the squared nature of the equation makes the outer part of the spectrum account significantly more), but indirectly through the normalisation factor (the denominator). This would lead to a considerable underestimation of the second moment if signal from non-sample origin is not appropriately considered.

One solution is to experimentally reduce the signal from the insert through an IR sequence. This inverts the insert signal with a 180 ° pulse and a delay selected to invert the narrow, fast relaxing signal. In theory, this leaves only the signal from the sample but getting a perfect inversion in reality is difficult.

There are further problems arising from the integration method: noise and small baseline imperfections which are illustrated in Figure 4.21. While the normal integration (red dotted line) converges smoothly with the integration range, the weighting by the square of the frequency in Equation 4.5 means M_2 becomes very sensitive to noise in the outer parts of the spectrum, as well as small changes in the baseline. This means that the second moment is not guaranteed to converge, as shown by the blue dotted line, and its integral has very poor numerical stability. In order to provide some kind of quantification of the uncertainty when using this approach, M_2 has been evaluated with different integration limits corresponding to 97 %, 98 %, 99 % and 99.5 % of the conventional integral.

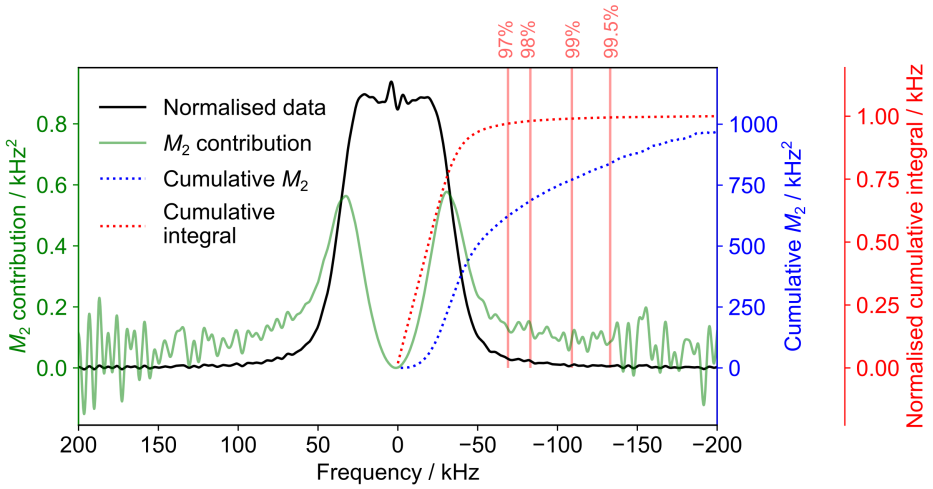

Figure 4.21: Static ^{1}H IR spectrum of triamantane at 192 K, with insert signal suppressed by IR, showing the second moment contribution of each point (green), and integrated contribution to the second moment (blue) and normalised spectral integral (red) as a function of integration width, which is symmetrical about the mid frequency.

The 'M_2M_4' Expansion for FIDs

A general approach to non-Gaussian lineshapes is to fit the time-domain signal to:

$$1 - \frac{t^2}{2!}M_2^\omega + \frac{t^4}{4!}M_4^\omega - \frac{t^6}{6!}M_6^\omega + ... \tag{4.6}$$

where $M_{2/4/6}^\omega$ are second and higher order moments expressed in angular frequency.[48] In practice, the convergence of this series is poor, and the results are very sensitive to the range of the FID that is fitted. Figure 4.22 illustrates this, where time domain data (black) are fitted to a power series of moments (red) as given by Equation 4.6 from $t = 0$ to the value on the x axis. Fitting to a short interval with relatively little signal evolution leads to a large standard error on the fit. Fitting out to 36 µs however introduces significant systematic error; the upturn at the end shows the deviation between the data and the polynomial model. Excluding very short fitting intervals with large uncertainties (8 µs) and those which show systematic deviations at the end of the fitting (35 µs and longer) gives a moderately consistent estimate of M_2.

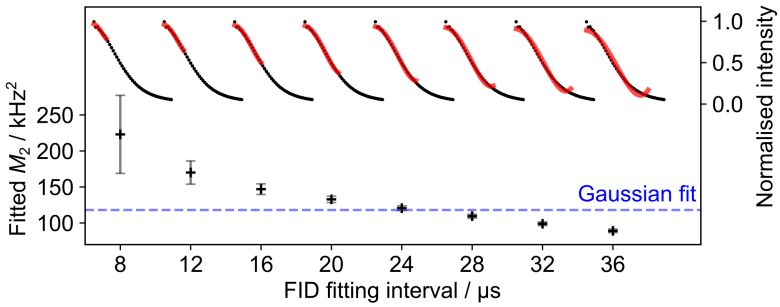

Figure 4.22: FID of triamantane at 360 K (black) and its fitting to Equation 4.6 (red) between $t = 0$ and an increasing fitting interval shown on the x axis. Error bars show the uncertainty on the fitted M_2 from the least-squares regression.

4.4.1.1 Methodology Exploration

Within the temperature range measured, ^{1}H spectra of triamantane changes considerably, from a broad static pattern at 192 K, to a dynamically averaged spectrum at 360 K, to a very narrow, highly dynamic spectrum at 469 K. The signal of non-sample origin due to low sample volume is visible below 420 K. Figure 4.23 shows the fits using each method discussed in Section 4.4.1 for the spectra, and FIDs of triamantane taken at three different temperatures with and without IR. The 'raw' fitted values from these graphs are given in Table 4.7 with the calculated second moments given in Table 4.8.

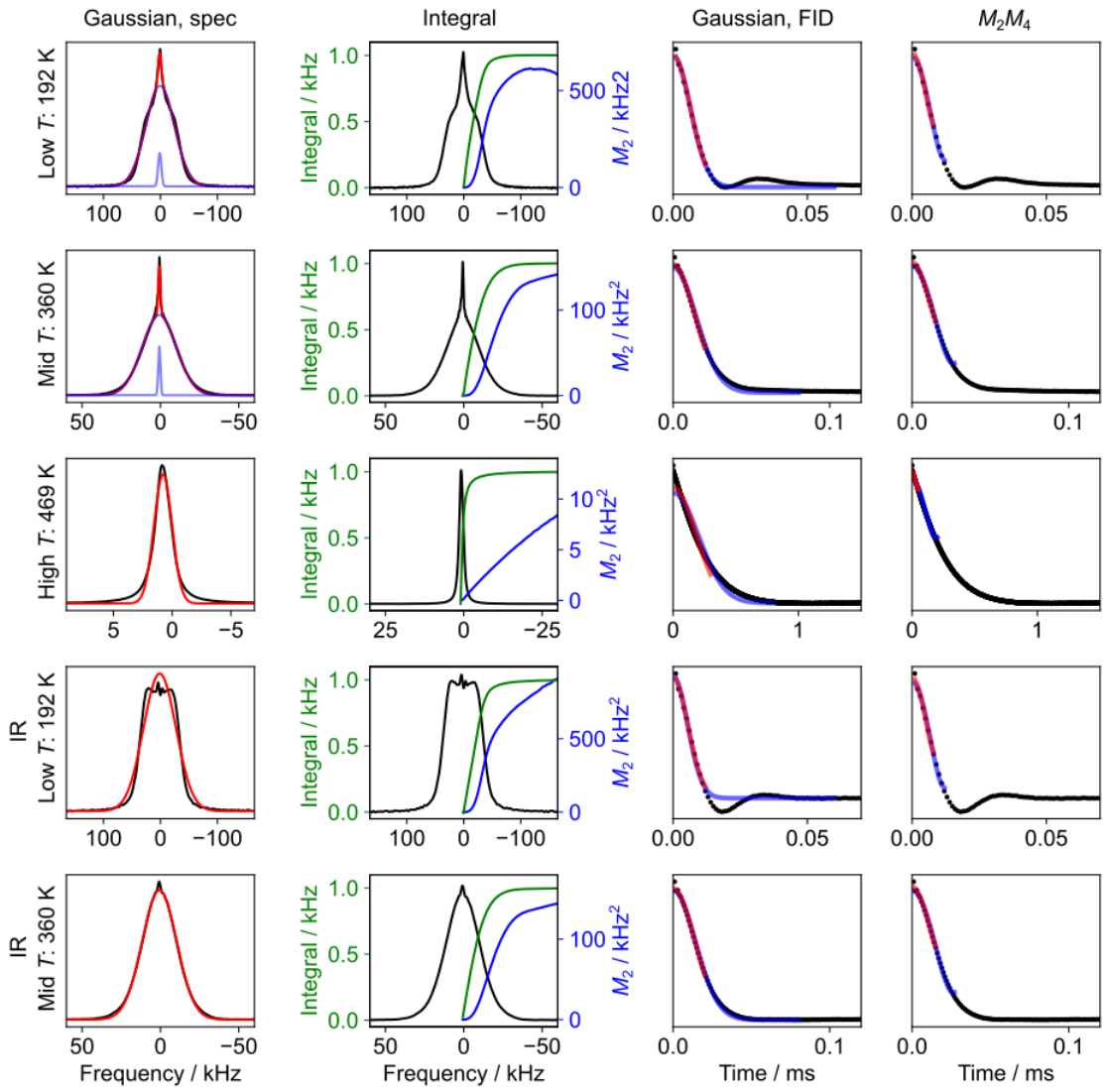

Figure 4.23: Static ^{1}H spectra and FIDs of triamantane with (lower two rows) and without (top three rows) an IR sequence, corresponding to the low, mid and high T. The columns correspond to different second moment fitting methods. Column 1: Gaussian fitting (red) of the spectrum (black) and insert signal (blue). Column 2: second moment (blue) and integral (green) as a function of integral width with overlaid spectrum (black). Column 3: Gaussian fitting (red and blue) of different fitted regions of the FID (black). Column 4: M_2M_4 method, both FID fits showing the smallest fitted region (red) and the largest region (blue).

Table 4.7: Triamantane M_2 'raw' fits at three temperatures. Top three rows are without IR, lower two are with IR.

	Spectrum			**FID**[a]	
	Gaussian σ **/ kHz**[b]	**Integration** M_2 **/ kHz^2**		**Gaussian** σ **/ µs**	M_2M_4 $(2\pi)^2 M_2$ **/ Hz^2**
Low T **192 K**	25.11(3) (2.80(3))	97% = 460 99% = 529	98% = 492 99.5% = 554	*12, 60 µs* 6.41(11) 6.38(10)	*8, 12 µs* $2.8(3) \times 10^{10}$ $2.16(12) \times 10^{10}$
Mid T **360 K**	10.872(7) (0.686(3))	97% = 105 99% = 124	98% = 114 99.5% = 128	*30, 80 µs* 14.41(15) 14.75(12)	*18, 28 µs* $5.24(10) \times 10^9$ $4.24(9) \times 10^9$
High T **469 K**	0.7811(11)	97% = 2.37 99% = 4.58	98% = 3.08 99.5% = 6.13	*300, 800 µs* 179.4(14) 203.7(12)	*50, 200 µs* $2.07(13) \times 10^8$ $5.27(10) \times 10^7$
IR					
Low T **192 K**	28.50(8)	97% = 622 99% = 761	98% = 678 99.5% = 835	*12, 60 µs* 5.52(10) 5.36(15)	*8, 12 µs* $3.2(4) \times 10^{10}$ $2.51(14) \times 10^{10}$
Mid T **360 K**	10.994(6)	97% = 113 99% = 130	98% = 121 99.5% = 138	*30, 80 µs* 14.20(8) 14.37(7)	*18, 28 µs* $5.31(10) \times 10^9$ $4.38(9) \times 10^9$

[a] FID fits are at two fitting ranges, both starting at $t = 0$ s and ending at the values given in italics.

[b] Fitted to one or two Gaussians. When fitted to two Gaussians, both σ values are given with the top being the sample value and the lower being the insert value.

Table 4.8: Triamantane M_2 results by method (in kHz^2) calculated from the 'raw' results given in Table 4.7. Uncertainties in brackets represent a strict error determined from least squares fitting. Uncertainties denoted by ± are estimated from the extreme fitted values.

	Spectrum		**FID**	
	Gaussian[a]	**Integration**[b]	**Gaussian**[c]	$\boldsymbol{M_2 M_4}$[c]
Low *T*: 192 K	630.3(12)	490 ± 40	620 ± 20	630 ± 90
Mid *T*: 360 K	118.18(15)	114 ± 9	119 ± 3	120 ± 13
High *T*: 469 K	0.634(2)	3.6 ± 1.6	0.70 ± 0.08	3.3 ± 1.9
IR				
Low *T*: 192 K	812(4)	680 ± 70	860 ± 30	720 ± 90
Mid *T*: 360 K	120.88(13)	121 ± 9	124 ± 2	122 ± 11

[a] Values and uncertainties from least-squares fitting.
[b] Value from '98 %' integration. Uncertainty from ('99 %' − '97 %')/2
[c] Value from $(M_{2\mathrm{A}} + M_{2\mathrm{B}})/2$. Uncertainty from $(M_{2\mathrm{A}} - M_{2\mathrm{B}})/2$ where $M_{2\mathrm{A}}$ and $M_{2\mathrm{B}}$ are the largest and smallest fitted values respectively given in Table 4.7.

The lowest temperature spectrum is consistent with a static lineshape and does not fit well to a Gaussian. Fitting the spectrum or FID to a Gaussian results in systematic errors which become more substantial when squared (since $M_2 = \sigma^2$). These systematic errors will not be reflected in the estimated uncertainty. Fitting different regions of the FID does give a larger and slightly more realistic uncertainty but is much smaller than the 15 – 25 % error assumed by Britcher and Strange.[27] For the low and mid temperature measurements, each method gave very similar values with the exception of the integration method for the spectra without IR. As explained above, it is expected that this method will underestimate the second moment in spectra with significant signal of non-sample origin.

The simplest method of calculating second moments is fitting the lineshape to a Gaussian. Difficulties arise when lineshapes deviate significantly from Gaussian, which was most noticeable in the slow limit of triamantane, as shown in Figure 4.23 (column 1, row 1 and row 4) and the limit of self diffusion/isotropic motion (column 1, row 3). Fitting the FID to a Gaussian requires arbitrarily chosen fitting regions for non-Gaussian lineshapes. Recording more of the echo rise as well as the decay may have helped with this. All FIDs here were recorded with a 15 µs inter-pulse echo delay (D6), a pre-acquisition delay of 10 µs (DE) and an additional delay (D7) of 5 µs i.e. recording starts at the assumed echo peak at twice the inter-pulse delay. A brief retrospective experiment with different decay times showed that this affected the result by approximately 6 % as shown in Figure 4.24 and Table 4.9.

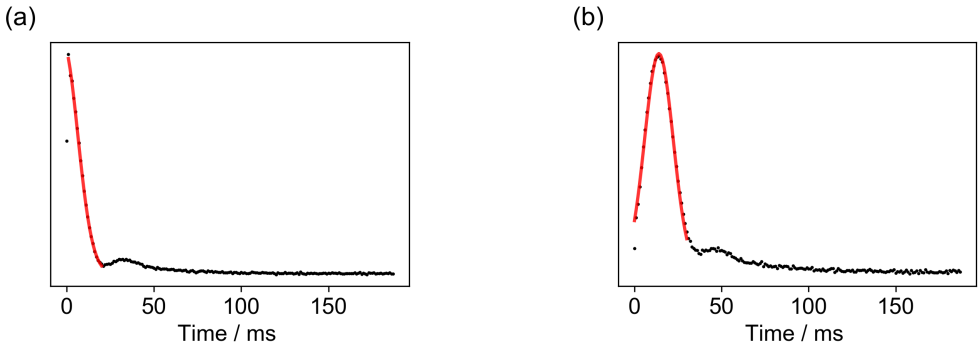

Figure 4.24: FIDs taken with different delay periods. Delays and fit given in Table 4.9.

Table 4.9: Second moments of diamantane with different delay periods.

	D6	**D7**	**DE**	$\boldsymbol{\sigma}$ **/ kHz**	$\boldsymbol{M_2}$ **/ kHz^2**
a)	15	5	10	8.47(19)	72(3)
b)	20	0	5	8.22(12)	68(2)

4.4.1.2 Proposed Methodology Guidelines

From the triamantane results discussed above, the following second moment fitting guidelines are proposed. These guidelines are followed in Section 4.4.2 with diamantane, 1(2)3 tetramantane and cyclohexamantane.

For spectra which are very Gaussian in nature the simplest and best method is to fit the spectrum to a Gaussian lineshape. This method is the most objective as it requires no arbitrarily chosen fitting ranges, however it may give a small uncertainty. This small statistical uncertainty will not reflect the overall uncertainty which arises from other factors such as changes in the spectrum from increased libration.

Where spectra do not fit well to a Gaussian, calculating M_2 from a Gaussian fit will not give an accurate result, and the errors will not reflect the systematic errors present. In which case the two options for fitting are the integration method or the M_2M_4 method.

If spectra are excellent quality i.e. the baseline is flat, the noise is low and there are no spectral features from anything other than the sample, the best method is to integrate. There will always be an element of choice, for example 98 % or 99.5 % but the difference between these values will be small with excellent quality spectra. This method cannot be used if there is signal from anything other than the sample, as discussed above, without first attempting to remove it (experimentally or digitally).

If spectra are less than excellent quality, the reserve technique to use is the M_2M_4 expansion. This method is less affected by imperfect baselines or additional narrow signals than the integration method, and can provide a reasonable estimation of an error. As before, there will always be choice in terms of fitted region, however this is the least worst option in this case.

4.4.2 Second Moment Results

4.4.2.1 Diamantane

Figure 4.25 shows the second moments of diamantane, determined by fitting the spectrum to a Gaussian. Selected spectra fitted with each of the four discussed methods are given in Appendix A, however the alternative methods were not used for spectra with strong Gaussian character. The static limit was not able to be measured due to temperature limits of the equipment used. All spectra recorded in phase III and II were dynamic and fitted well to a Gaussian lineshape. As is the case for triamantane, the spectrum at high temperature is narrow and does not fit to a Gaussian. There are plateau regions highlighted in grey separated by sections with steeper drops indicating the emergence of a new type of motion. The gradual drops within a plateau region are due to the increase in wobbling and librational motions.

The plateau regions documented in Table 4.10 are given as a range of values within a temperature region. The values are based on a Gaussian fit of the spectra except for the high temperature region for which an estimated maximum M_2 from all methods given in Table A.2 in Appendix A.

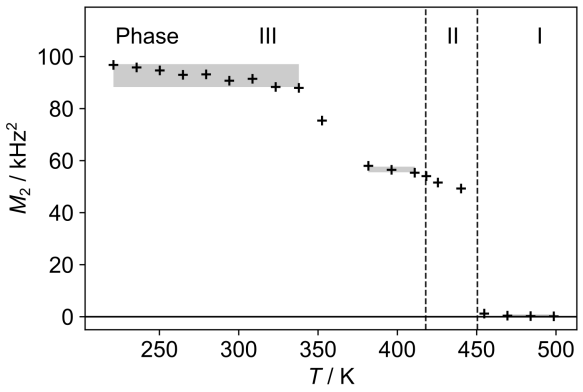

Figure 4.25: Diamantane second moments as a function of temperature determined by fitting spectra to a Gaussian. Grey areas indicating plateau regions. Fitting uncertainties were significantly smaller than the marker size.

Table 4.10: Second moments of diamantane.

Temperature / K	**Phase**	M_2 **/ kHz^2**
221 – 338	III	97 – 88[a]
382 – 411	III	58 – 55[a]
461 – 499	I	<0.8[b]

[a] Range from individual Gaussian fits.
[b] Estimated maximum from all fitting methods.

The experimental second moments documented in Table 4.10 are almost identical to the values given by Britcher and Strange (repeated in Table 4.11). The lowest temperature

measured here is in excellent agreement with the Britcher and Strange value of 96(14) kHz at 200 K and the highest temperature value is described as rapidly approaching zero. While there are not enough values recorded in phase II to show a reliable plateau region, the two values that were recorded at 51.6 and 49.3 kHz^2 are in agreement with the 49(9) kHz^2 by Britcher and Strange. The only discrepancy was the drop in the second moment within phase III which was very subtle in the literature: 'a plateau of about [78 kHz^2] may exist although this is uncertain due to the scatter in the data'.[27] This was clear in the data here and showed a more significant drop to 58 – 55 kHz^2.

Table 4.11: Second moments of diamantane determined by Britcher and Strange.[27]

Temperature / K	**Phase**	M_2 **/ G²**	M_2 **/ kHz²**
95 – 135	III	26.2(6.6)	480(120)
200[a]	III	5.3(8)	96(14)
350[a]	III	4.3(7)	78(13)
409[a]	II	2.7(5)	49(9)
442.5	I	0.54(4)	9.8(7)

[a] Reported the lowest temperature of a plateau region. M_2 given at that temperature.

4.4.2.2 Triamantane

Second moments of triamantane as a function of temperature are given in Figure 4.26. Unlike diamantane which showed significant dynamics even at the coldest experimental temperature recorded, the motion of triamantane was (at least mostly) frozen out below 300 K. These static spectra did not fit well to a Gaussian, and hence the values given in Figure 4.26 are from the M_2M_4 method. Spectra above 325 K showed strong Gaussian character hence second moments were estimated from fitting the spectra to Gaussian, or Gaussians where an insert signal was seen. Values are summarised in Table 4.12.

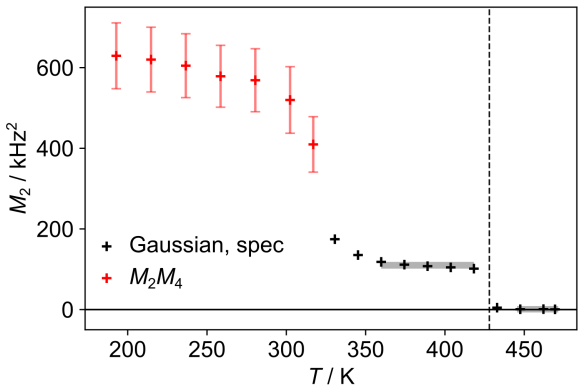

Figure 4.26: Triamantane second moments as a function of temperature. Above 325 K spectra are fitted to a Gaussian. Below 325 K the M_2M_4 method is used. Grey areas indicating plateau regions. Uncertainties from the Gaussian fits were significantly smaller than the marker size.

Table 4.12: Second moments of triamantane.

Temperature / K	M_2 **/ kHz^2**
192	630 ± 90[a]
360 – 418	117 – 101[b]
447 – 469	<6[c]

[a] M_2M_4 fit of FID at 192 K which is assumed to be representative of the low temperature plateau.
[b] Range from individual Gaussian fits.
[c] Estimated maximum from all fitting methods.

4.4.2.3 1(2)3 Tetramantane

Second moments of 1(2)3 tetramantane as a function of temperature are given in Figure 4.27. Overall patterns were similar to triamantane, with the spectra fitting to a Gaussian when there was some dynamic averaging.

Broad spectra consistent with static molecules were observed at the coldest temperature recorded, but there was not a distinct plateau as observed with triamantane, perhaps indicating that the motion of the molecules was not fully frozen at 192 K. This could be because a rotation about the C_3 axis requires less physical space than the C_2 rotation of triamantane and does not break the symmetry, unlike the pseudo-C_2 rotation of triamantane (see Figure 4.29 for axes).

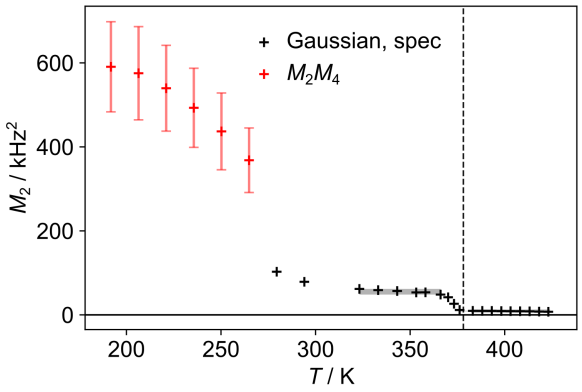

Figure 4.27: 1(2)3 tetramantane second moments as a function of temperature. Above 280 K spectra are fitted to a Gaussian. Below 280 K the M_2M_4 method is used. Grey areas indicating plateau regions. Uncertainties from the Gaussian fits were significantly smaller than the marker size.

Table 4.13: Second moments of 1(2)3 tetramantane.

Temperature / K	M_2 **/ kHz^2**
192	590 ± 110[a]
323 – 366	62 – 48[b]
376 – 423	7.8 – 9.0[b]

[a] M_2M_4 fit of spectrum at 192 K.
[b] Range from individual Gaussian fits.

4.4.2.4 Cyclohexamantane

The second moments of the cyclohexamantane as a function of temperature are given in Figure 4.28. The second moments gradually reduced but were consistent with a static sample throughout the temperature range measured here.

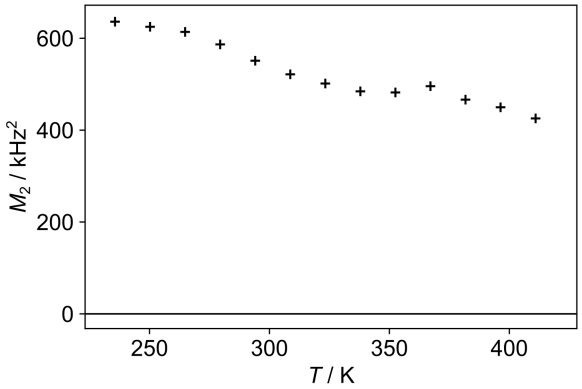

Figure 4.28: Cyclohexamantane second moments as a function of temperature using the Gaussian fitting method.

Table 4.14: Second moments of cyclohexamantane.

Temperature / K	M_2 **/ kHz^2**
236 – 411	636 – 426[a]

[a] Range from individual Gaussian fits.

4.4.3 Second Moment Calculations

It is prohibitively difficult to determine precise ^{1}H lineshapes theoretically due to the significant number of dipolar coupling calculations required in a real system. However, there have been several approaches to estimate a theoretical second moment. Van Vleck laid down the mathematical theory in 1948 where fundamental equations were set out for the analytical determination of second moments of static molecules.[49] However practical applications of the second moment require calculation of the second moment in the presence of dynamics. In the 1970s, papers such as Britcher and Strange were calculating

the intramolecular component of second moments in dynamic molecules, however intermolecular remained difficult and approximate reduction factors were used.[27] Roman Goc released numerous papers between 1983 and 2005 calculating second moments of various molecules with different types of internal rotations.[50–56] Here a numerical approach was used to calculate all the dipolar couplings in an individual crystalline orientation which were then averaged over a type of motion. This was then repeated for many powder orientations which made the calculation slow and cumbersome. Goc released the only publicly available code for calculating second moments, however it is restricted to 3-fold diffusion rotation and is Fortran-based.[57]

The calculations used here go back to the fundamentals determined by Van Vleck who derived the second moment on the basis that dipolar interactions are symmetric tensors aligned along the internuclear vector. While this approach was sufficient for static molecules, dynamic molecules have tensors which are not always symmetric and require asymmetry parameters. The new formulae given in reference 44 rederive the formulae that Van Vleck used but include an asymmetry parameter. This second moment, given as a function of orientation, can then be averaged over all angles giving the powder average which can be calculated analytically.

4.4.3.1 Implementation

Atomic coordinates of a sample are determined by SCXRD which is typically run at 120 K. As found previously,[58] using uncorrected ^{1}H positions lead to unreliable results as the second moments are very sensitive to ^{1}H positions, which are not well determined by XRD in general. Hence the ^{1}H positions were relaxed using CASTEP.[59] In the case of diamantane, for example, the second moment was over-estimated by about 15 % using the diffraction co-ordinates. In contrast, there was negligible difference in calculated M_2 values depending on whether just ^{1}H positions or all atomic positions were relaxed. The values shown in Table 4.15 are for structures with ^{1}H positions only relaxed. Axes and pseudo-axes of rotation are given in Figure 4.29.

Due to the similarities in the structures between the diamondoids, there are consistencies in the calculated M_2 values. Static second moments were between $360-400\,\mathrm{kHz}^2$, with the biggest variation coming from the reduced intramolecular component of cyclohexamantane due to the increased distances between ^{1}H atoms within the larger molecule. Rotation about the C_3 axis in diamantane, 1(2)3 tetramantane and cyclohexamantane gave a reduction of 75 – 80 % from the static value. Rotation about the C_2 axis in diamantane, triamantane and cyclohexamantane gave a reduction of around 50 % from the static value. Combining a C_2 (or pseudo-C_2) axis with a perpendicular C_3 axis did lead to a further small reduction from a C_3 alone of between 10 – 20 %. In the case of triamantane, three orthogonal C_2-like motions can be proposed. Note that any pair of C_2-like motions is equivalent to the third, and so there is no physical significance to considering all three motions simultaneously, and the same value of M_2 is obtained if two C_2-like motions are

Table 4.15: Calculated powder-averaged M_2 values for different motional models based on the axes given in Figure 4.29. Molecules included up to a radius of 20 Å.

	Intramolecular / kHz^2	**Intermolecular / kHz^2**	**Total / kHz^2**
Diamantane			
Static	263.1	137.1	400.2
C_3	67.8	35.4	103.2
C_2	165.5	43.0	208.4
C_3 + C_2	67.8	16.5	84.2
L	186.8	52.7	239.5
C_3 + L	48.1	25.7	73.8
Triamantane			
Static	260.7	128.7	389.4
C_2	147.9	42.0	189.9
Pseudo-C_2 (long)	165.7	46.6	212.3
Pseudo-C_2 (short)	173.3	43.8	217.1
C_2 + one pseudo-C_2[a]	113.1	18.7	131.9
1(2)3 Tetramantane			
Static	272.5	127.3	399.8
C_3	62.8	22.3	85.1
Pseudo-C_2	167.4	71.5	239.0
C_3 + pseudo-C_2	62.7	14.9	77.6
Cyclohexamantane			
Static	231.6	127.8	359.5
C_3	50.5	22.0	72.4
C_2	141.1	40.1	181.1
C_3 + C_2	50.5	10.8	61.3

[a] C_2 + pseudo-C_2 (long) = C_2 + pseudo-C_2 (short) = pseudo-C_2 (short) + pseudo-C_2 (long) = C_2 + pseudo-C_2 (short) + pseudo-C_2 (long)

considered. The diamantane results also contain a non-orthogonal 'L' axis, as suggested by Britcher and Strange, which runs between the bisection of a C1–C2 bond and the centre of mass.

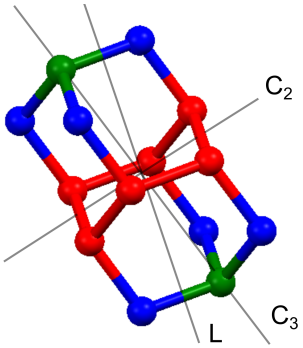

(a) Diamantane with the C_3 axis, 'L' axis and one of the three equivalent C_2 axes drawn.

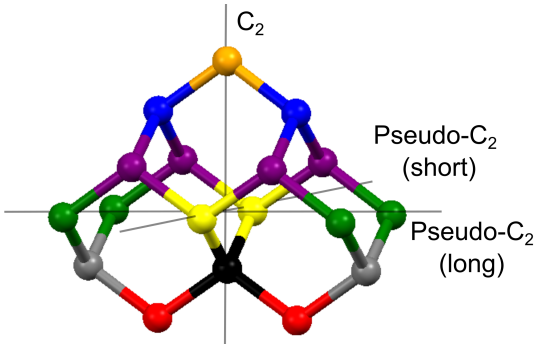

(b) Triamantane with the C_2 axis and the two pseudo-C_2 axes drawn.

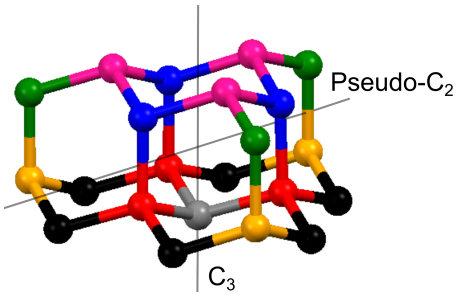

(c) 1(2)3 tetramantane with the C_3 axis and one of the three equivalent pseudo-C_2 axes drawn.

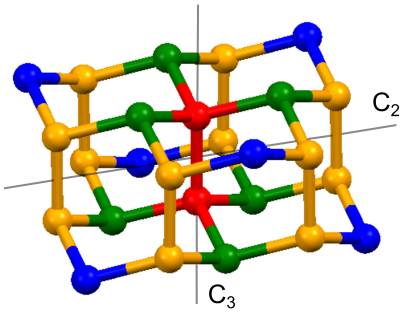

(d) Cyclohexamantane with the C_3 axis and one of the three equivalent C_2 axes drawn.

Figure 4.29: Diamondoid axes and pseudo-axes of symmetry.

4.4.4 Experimental and Simulation Comparison

Table 4.16 summarises the experimental second moments of individual temperatures and at plateau regions. Different potential motions for each temperature region are also suggested based on the calculated M_2 values. The regions with ultra low second moments ($<10\,\mathrm{kHz}^2$) have not been included since lineshapes are increasingly determined by relaxation and develop Lorentzian characteristics, hence second moment analysis is inappropriate.

Overall, there is a distinct difference between dynamic regions, where experimental and calculated values are similar, and static regions, where the difference is much more significant. In general, experimental values are expected to be a little lower than simulated due to additional librational motions as well as expansion in the structures acquired by SCXRD at 120 K. This is seen in the dynamic regions however the static experimental values ($\approx 620\,\mathrm{kHz}^2$) are significantly higher than the predicted ($\approx 400\,\mathrm{kHz}^2$). Additionally, the experimental values are quoted at the coldest value experimentally achievable and hence are not likely to represent the largest M_2 value in the plateau. The discrepancy between the experimental and calculated values may come from the solid echo itself. Solid echoes, which are typically used to acquire ^{1}H signals under static conditions, result in

a signal that is not an exact match of the 'true' FID,[60] in contrast to the refocusing of frequency dispersion by a spin echo. This introduces systematic errors in the M_2 values obtained by fitting echo decays, which increase rapidly with the echo period.[48] Although the echo period used in this study (15 µs) is not much larger than used in other studies, e.g. 10 µs in reference 47, it is plausible that these effects explain the inconsistent values of M_2 obtained in the low temperature limit.

Table 4.16: Experimental M_2 values at plateaus and best match from calculated values. Lowest temperature and corresponding M_2 is underlined highlighting the value least affected by additional librational motion.

	Experimental M_2 / kHz^2	**Calculated M_2 / kHz^2**
Diamantane		
221 – 338 K	97 – 88	C_3 axis: 103.2
382 – 441 K	58 – 55	C_3 + C_2: 84.2 or C_3 + L: 73.8
Triamantane		
192 K	630 ± 90	Static: 389.4
360 – 418 K	117 – 101	Two C_2 axes: 131.9
1(2)3 Tetramantane		
192 K	590 ± 110	Static: 399.8
323 – 366 K	62 – 48	C_3 axis: 85.1 or C_3 + pseudo-C_2 axis: 77.6
Cyclohexamantane		
236 – 411 K	636 – 426	Static: 359.5

As shown in Table 4.16, the motion of diamantane at 221 K is consistent with the rapid dynamics about its C_3 symmetry axis shown by ^{13}C relaxation studies in Section 4.3.2. The dynamics in the higher temperature regime at 382 K indicates that the molecules are constrained, but are undoing significantly more motion than at 221 K. This motion has previously been described in terms of rotation about an additional 'L' axis tilted away from the symmetry axis.[27] Another possible scenario is that there are occasional flips of the molecule around its C_2 axis, which is compatible with a jump-only value of M_2 of 83.5 kHz^2.

In the case of triamantane, the second moment results show that the dynamics of the molecule likely involves jumps about multiple C_2/pseudo-C_2 axes. The energetic barriers are expected to be lowest for the symmetry-preserving C_2 and the symmetry-breaking 'top over bottom' flip of the molecule about the long molecular axis. As in the case of diamantane, the experimental second moment in the high temperature regime is significantly smaller than the prediction from an idealised motion, due to overall libration. This picture is consistent with diffraction data in which a gradual order-disorder transition between 273 – 300 K was found to be associated with an additional pseudo-mirror plane corresponding to a symmetry-breaking flip of the molecules.[37] It is important to note that the diffraction data is not sensitive to the symmetry-preserving C_2 motion and so the NMR data, via the second moments, is providing a more complete picture of the dynamics

in this sample.

For 1(2)3 tetramantane, the second moments show that there is a C_3 motion above 323 K. This is consistent with the picture from ^{13}C relaxation. However, it is impossible to discriminate between a standalone C_3 motion (85.1 kHz^2) and a C_3 + a pseudo-C_2 motion (77.6 kHz^2) due to the closeness in the two values.

The second moment data of cyclohexamantane has shown that the molecules are static in the temperature range 236 – 411 K. In a sample where most types of data such as ^{13}C spectra or ^1H relaxation as a function of temperature is too time intensive to measure, simple ^1H spectra as a function of temperature have provided insight into the dynamics (or lack of dynamics) in this system.

4.5 Conclusion

Diamondoids are an interesting series of highly symmetrical hydrocarbon cages with significant molecular motions in the solid state. Relaxation measurements have proven very useful for determining activation barriers and rates of motion. ^{13}C T_1 relaxation in particular has provided valuable information to characterise the C_3 motions present in diamantane and 1(2)3 tetramantane. However, for triamantane relaxation could not determine the nature of the motion. It is in this case the second moments proved useful and found there was likely a combination of C_2/pseudo-C_2 jumps.

There are situations when ^{13}C relaxation might not provide useful information. The most obvious is if a ^{13}C spectrum is not obtainable either due to motional interference, as was the case for triamantane, or too small sample volume, as was the case for cyclohexamantane. Additionally, relaxation times can struggle to distinguish large and small amplitude motions, for example, a small wobble-type motion could be misinterpreted as a large-angle, jump-type rotation.

There are also instances where interpreting second moment data is difficult. For example in the case of 1(2)3 tetramantane, the differences in second moment between different C_3/C_3 + pseudo-C_2 motions were small and hence it is not realistic to distinguish between very similar motional models using second moment data.

On balance, second moments have been shown to be a useful complementary tool for studying molecular reorientation in organic solids. It is hoped that with the publicly available script,[61] and the modern discussion on how to calculate a second moment from a spectrum, second moments could become more routinely used to fill gaps in data from modern methods.

Chapter 5

Examining the Dynamics in Hydrazinium Magnesium Formate

5.1 Metal Organic Frameworks

Metal organic frameworks (MOFs) are a group of crystalline materials that consist of transition-metal cations connected by multidentate ligands. The periodic arrangement of the metal nodes bonded through organic linkers creates a cage-type structure with significant voids, meaning MOFs have the largest surface areas of any porous material.[62] These cavities or channels allow for the uptake of large volumes of gases and hence application-driven research on MOFs is often focused on their potential use as materials for gas capture,[63] gas separations,[64] chemical sensing[65] and catalysis.[66]

The incorporation of guest molecules as an intrinsic element of the material, and not a target of an application, is comparatively less utilised.[67] These guest incorporations can create materials with new properties distinct from the components in isolation. Unlike the MOFs used in gas sorption, where MOF – guest interaction is typically weak, structural guests can have much stronger interactions with the host framework. These stronger interactions can alter many aspects of the material properties such as electronic states and luminescence behaviour.[68]

This chapter will discuss the dynamics found in hydrazinium magnesium formate (HMF), a MOF which exhibits complex, phase-dependent dynamics of both the included hydrazinium ions and the formate framework. It was described by Chen et al. as having relaxor ferroelectric behaviour, a specific type of ferroelectric behaviour with unusual dielectric properties.[69] The aim of the work is to discover the origins of the relaxor ferroelectric behaviour by uncovering the dynamics of the hydrazinium cation using multiple solid-state NMR techniques alongside alternative methods to build a picture of the dynamics above and below the phase transition.

5.2 Relaxor Ferroelectrics

Capacitors are a vital component to store electrical energy in all modern electrical devices, from mobile phones to microwaves to cars. Almost all capacitors are made of at least two electrical conductors separated by an electrical insulator, known as a dielectric. This allows a positive charge to build up on one conductor and a negative charge to build up on the other. All dielectric materials are electrical insulators meaning there will be no flow of charge when placed in an electric field, however there are changes on an atomic scale. Dielectrics exhibit electric polarisation meaning that electrical charges, such as electrons or ions, are displaced in the direction of the field. This polarisation can be reversed with an opposing applied electric field.

While many materials will be polarised by an applied electric field, ferroelectrics are a specific type of dielectric which can have a non-zero polarisation when no electric field is applied. Unlike linear dielectrics where the polarisation in the material only depends on the direction and magnitude of the field, ferroelectricity also depends on the history of the material. This is shown in Figure 5.1 which demonstrates the effect of increasing the electric field on polarisation on different types of dielectrics. For a linear dielectric, there is no hysteresis, meaning that polarisation of the material is not dependent on the material's electrical history, as demonstrated in Figure 5.1a. When the electric field is removed, a linear dielectric material will return to the original non-polarised state. This is in contrast to the hysteresis loop in a ferroelectric, shown in Figure 5.1b, where there is a lag in the polarisation when the electric field is changed.

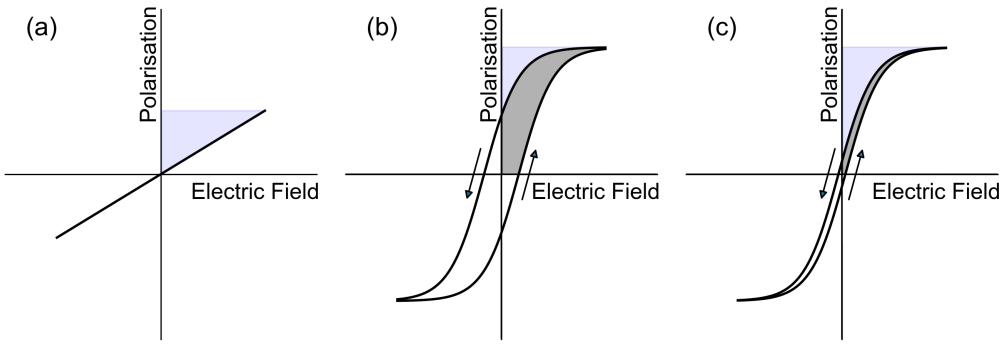

Figure 5.1: Representation of the typical polarisation vs electric field hysteresis loops and energy storage characteristics of three dielectric materials: (a) linear dielectric; (b) ferroelectric; and (c) relaxor ferroelectric. Total shaded area represents the stored energy. The darkest shaded area is the energy lost. Demonstration only, not to scale, reproduced from reference 70.

As a result of the ferroelectric hysteresis, ferroelectrics exhibit large energy losses which is shown by the darker shaded area in Figure 5.1b. Since linear dielectrics have no hysteresis loops, they usually exhibit much higher efficiencies as capacitors than ferroelectrics. Because of this, significant research has gone into improving linear dielectrics.[71] However, the permittivity, corresponding to the slope of the polarisation curves, is often

much lower in linear dielectrics meaning the overall storage capability, denoted by the total shaded areas in Figure 5.1, is lower.

Relaxor ferroelectrics are a type of ferroelectric which also have a non-linear polarisation with respect to electric field. However, unlike other ferroelectric materials they have near negligible hysteresis, as shown in Figure 5.1c, meaning they have much greater efficiency. Relaxor ferroelectrics have the advantage of the high permittivity of the ferroelectrics as well as the efficiency similar to linear dielectrics. It is for this reason that relaxor ferroelectrics are gaining in popularity for capacitor materials.[70]

The behaviour of each type of dielectric is typically explained through the domain structures in the material. Linear dielectrics exhibit constant permittivity due to the lack of any permanent dipoles. Ferroelectrics are said to have large polar domains which will lag behind the applied field leading to the large hysteresis curves. In comparison, relaxor ferroelectrics are said to have less long-range order and are often explained through the existence of 'polar nanoregion regions' which are nanoscale polar domains within a non-polar average structure. This reduces the cooperative coupling among ferroelectric domains, hence the smaller hysteresis in a relaxor ferroelectric.[72]

Typically ferroelectric materials only show ferroelectric behaviour below a certain temperature known as their Curie temperature (T_c). Above this temperature the material has a paraelectric structure where the material contains permanent dipoles but no ferroelectric domains. This results in non-linear permittivity with respect to the electric field but the material returns to a non-polar state upon removal of the field as shown in Figure 5.2. This first-order phase transition is due to free energy. At low temperatures, the splitting into ferroelectric domains reduces electrostatic energy of the spontaneous polarisation charges, however, as the temperature increases this energy is offset by the energy required to form the domain walls.[73]

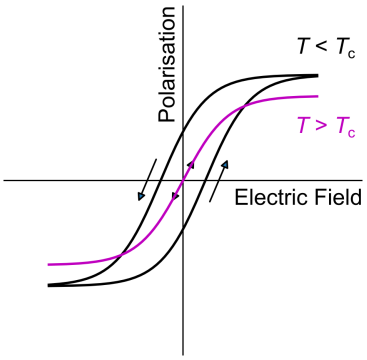

Figure 5.2: Representation of the polarisation vs electric field of a ferroelectric above (magenta) and below (black) the Curie temperature. Reproduced from reference 74.

Relaxor ferroelectrics show different temperature-dependent permittivity to ferroelectrics. One of the requirements of a relaxor ferroelectric, as set out by Cross, is that the temperature-dependent dielectric permittivity is a broad maximum described as a diffuse phase transition.[75] This broad maximum has been attributed to a distribution in the

Curie temperatures in each polar nanoregions by Ahn et al.[76] This is demonstrated in Figure 5.3b and is one explanation for understanding the broad temperature dependence in relaxor ferroelectrics. However it should be highlighted there are many models and explanations for relaxor ferroelectric materials without any consensus.[76]

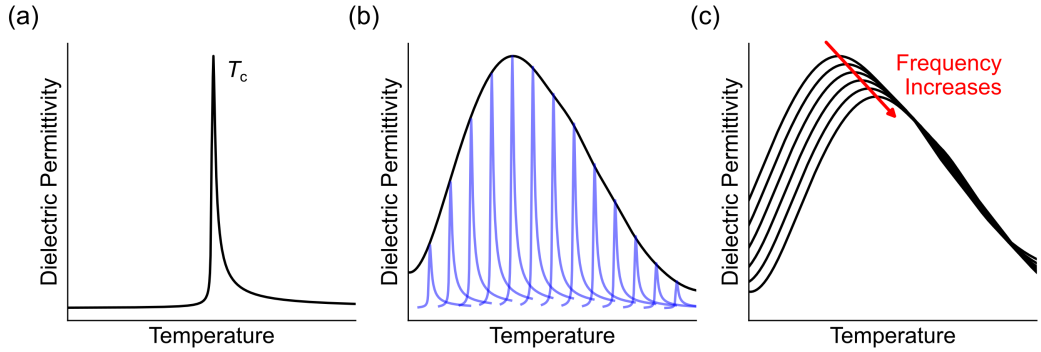

Figure 5.3: Representation of the temperature-dependent dielectric permittivity for: (a) a ferroelectric; (b) a relaxor ferroelectric showing the characteristic broad dependence; and (c) a relaxor ferroelectric showing the dependence on electric field frequency. Reproduced from reference 76.

The second requirement of a relaxor ferroelectric is that the temperature for the maximum dielectric permittivity is dependent on the frequency of the applied field.[75] This is demonstrated in Figure 5.3c and is attributed to the motion of boundaries between the ordered polar regions and the disordered non-polar regions.[76]

The origins of relaxor ferroelectric behaviours are not entirely understood, but explanations are almost always associated with disorder in some form. In perovskite oxides the behaviour is said to be the result of the relative displacement of ions from a dopant which induces static disorder of perovskite cations. The chemical inhomogeneity results in apparent 'polar nanoregions' or nanoscale polar domains within a non-polar average structure, as described earlier.[77] While the perovskite structure is most associated with relaxor ferroelectrics, there are other structures with different proposed mechanisms. For example, Rochelle's salt has hydrogen bond-driven relaxor behaviour where dynamic protons in hydrogen bonds trigger the ferroelectric ordering of the lattice.[78] There are also examples of conformational disorder in polymers where it is the chain chirality which drives the relaxor effects.[79]

Berlie et al. studied the dynamics and structure of an organic molecular solid $TEA(TCNQ)_2$.[80] They reported the notable similarities in the pattern of $R_{1\rho}$ $(= {T_{1\rho}}^{-1})$ at 50 kHz and the dielectric relaxation also at 50 kHz, as shown in Figure 5.4. This similarity indicated that both techniques were measuring the same process and hence they concluded that the relaxor ferroelectric properties were a consequence of the thermally activated barrier of the dynamic molecules.

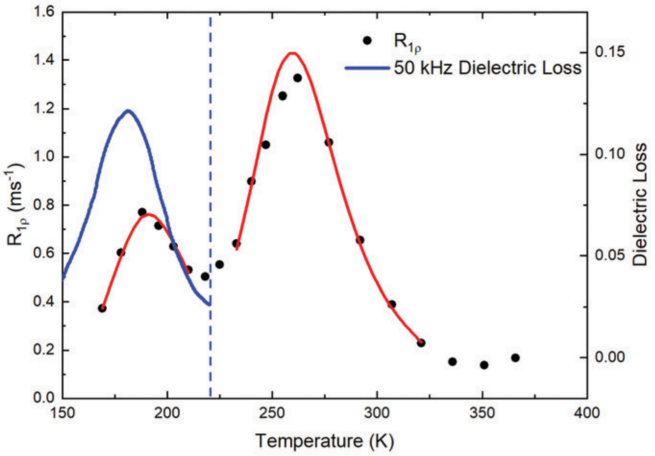

Figure 5.4: The temperature dependence of $R_{1\rho}$ at 50 kHz and dielectric losses also at 50 kHz of $TEA(TCNQ)_2$, showing remarkable similarities. Red lines show the relaxation fitting. Taken from reference 80.

5.3 Hydrazinium Magnesium Formate

HMF, or $(NH_3NH_2)Mg(HCO_2)_3$, is a MOF with a chiral hexagonal structure with six coordinated magnesium ions connected in an octahedral pattern through formate linkers in an *anti-anti* coordination mode. Formate, $HCOO^-$, is the simplest carboxylate linker and can adopt various bridging modes, as shown in Figure 5.5 and is a good hydrogen-bond acceptor. Hydrazinium ions (structure shown in Figure 5.6) exist in hexagonal channels throughout the framework.[69] The MOF was found to exhibit relaxor ferroelectric behaviour and unlike most materials, the relaxor behaviour was above its phase transition. The following section is a summary of the work reported by Chen et al. focusing on how the structure of HMF, determined by X-ray crystallography and physical measurements, were used to explain the relaxor-like behaviour they found.[69]

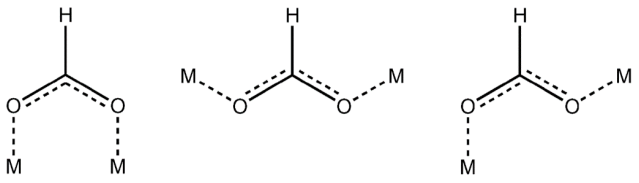

Figure 5.5: Different possible coordination modes of the formate anion: *syn–syn*, *anti–anti* and *syn–anti*.

Chen et al. were the first to use hydrazinium as a cationic component and template to synthesise a new class of ammonium metal-formate frameworks of $[NH_2NH_3][M(HCOO)_3]$ where M = Mn^{2+}, Zn^{2+}, Co^{2+} or Mg^{2+}.[69] Usually ammonium metal-formate frameworks are isostructural with different metal ions but here they formed two different structures: Mn^{2+} and Zn^{2+} had a perovskite structure and Co^{2+} and Mg^{2+} a chiral framework. This

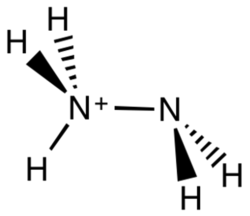

Figure 5.6: Structure of a hydrazinium ion.

is likely due to the intermediate size of the hydrazinium ion; the [AmineH][M(HCOO)$_3$] framework tends to adopt the perovskite structure for larger amine groups, such as $CH_3NH_3^+$, $(CH_3)_2NH_2^+$, $CH_3CH_2NH_3^+$, $(CH_2)_3NH_2^+$, $C(NH_2)_3^+$ and $(NH_2)_2CH^+$, whereas it tends to adopt the chiral framework for smaller amine groups such as NH_4^+ and $HONH_3^+$.

DSC traces of the four compounds synthesised by Chen et al. are shown in Figure 5.7 with the HMF compound of interest shown in blue (other metal ions also drawn). The endo/exothermic peaks were observed at 349 K and 347 K respectively i.e. it had a thermal hysteresis of just a few kelvin. There were three peaks in the region of 300 – 350 K, indicating it may be a complex multi-step transition. The combined TGA-DSC (thermogravimetric analysis-DSC) showed that HMF decomposes at 450 K.

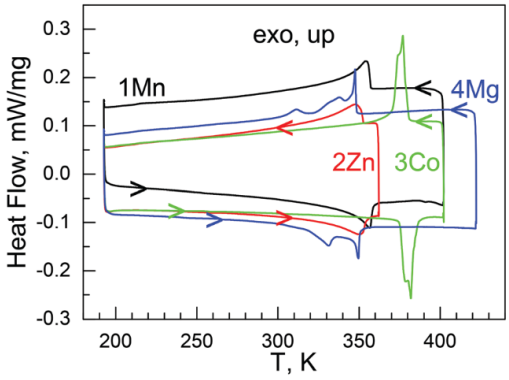

Figure 5.7: DSC traces of the four compounds, all first cycle. HMF shown in blue. Recorded by Chen et al.[69]

Chen et al. ran SCXRD at two temperatures: above and below the phase transition (400 K and 292 K). In both the high and low temperature structures, HMF contained octahedral magnesium atoms which connected to six others via *anti-anti* formate bridging linkers. Both structures had a metal–formate framework with hydrazinium molecules sitting within hexagonal channels. The space group changed from chiral orthorhombic space group in the low temperature phase to a polar hexagonal space group in the high temperature phase.

The definition of a chiral space group is complex but related to the molecular definition of having a non-superimposable mirror image. To be chiral, a space group must not contain a centre of inversion, a mirror plane or any rotation-reflection axes.[81] A polar space group is a crystal structure with a polar axis, which is the direction that cannot be

transformed into the opposite direction by any symmetry operation in the crystal class. Only crystals without a centre of symmetry can be polar since a centre of symmetry will transform a direction into the opposite one. Most crystal structures are neither polar nor chiral since approximately 78 % of structures in the Cambridge structural database are in centrosymmetric space groups.[82] Polar symmetry is considered rare. However many highly sought after properties of materials such as pyroelectricity, piezoelectricity and ferroelectricity are only allowed in polar space groups as they have the switchable polarisation characteristic required.[83]

Framework changes below and above the phase transition are reported to be small, however the cation undergoes a significant change, as shown in Figure 5.8. In the low temperature structure, cations lie approximately perpendicular to the hexagonal channels and are completely ordered in the lattice with adjacent cations oriented up and down. In the high temperature phase, the cation is said to become trigonally disordered, with cations lying approximately parallel to the channels. Hence the structural change from chiral orthorhombic space group, $P2_12_12_1$, to a polar hexagonal space group, $P6_3$, is described as being "triggered by the order–disorder transition of the cation".[69]

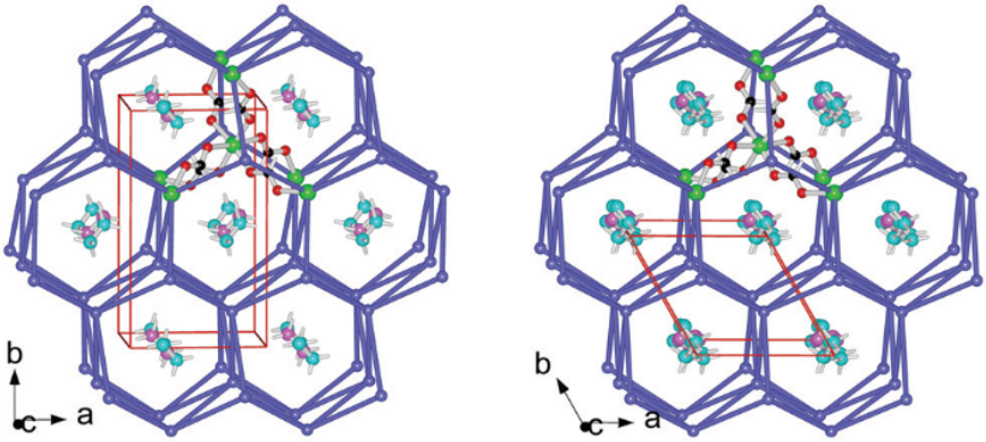

Figure 5.8: Structure of HMF below and above the phase transition, left and right respectively as determined by Chen et al. A small number of magnesium atoms shown as green balls, the rest as violet-blue balls. Formates shown as red and black balls or summarised by violet-blue lines. Hydrazinium molecules shown as cyan-purple.[69]

Experimental and simulated variable temperature powder X-ray diffraction (PXRD) patterns are shown in Figure 5.9 with the simulated patterns based on single crystal structures shown in colour. Asterisks highlight the subtle disappearances of some peaks above the phase transition between 340 – 350 K, which the authors put down to an increase in structural symmetry at high temperature.

The dielectric permittivity of HMF, given in Figure 5.10, shows dependence on electric field frequency. As the frequency increases, the rise in the permittivity is shifted to higher temperatures which is consistent with the relaxor-like behaviour. The derivative

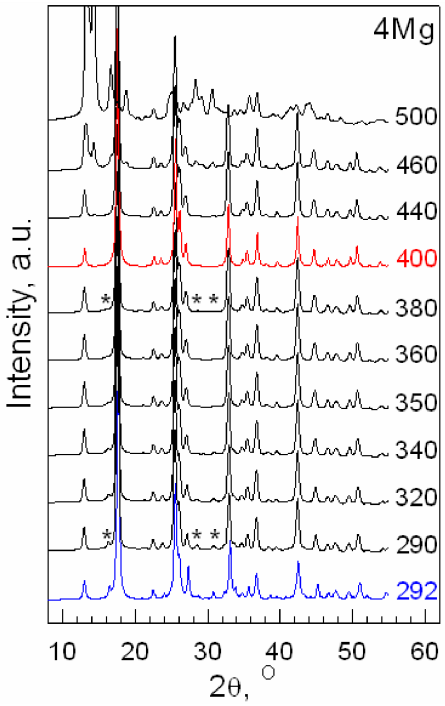

Figure 5.9: Variable temperature PXRD patterns for HMF, simulated patterns based on single crystal structures shown in colour. Temperatures given in K.[69]

plot at 1 MHz (inset) shows a complicated multi-step phase transition which is consistent with the DSC given in Figure 5.7. This relaxor-like behaviour was explained in terms of the structure of the cations. In the low temperature phase the cations are completely ordered in the lattice and hence the material is antiferroelectric. On heating, the weak hydrogen bonds and large voids in the framework allow the cations to become trigonally disordered. This creates a polar structure with all the cations aligning in the same direction within the channels. Fundamentally it is the order-disorder transition of the hydrazinium cations which creates the relaxor-like behaviour above the phase transition.

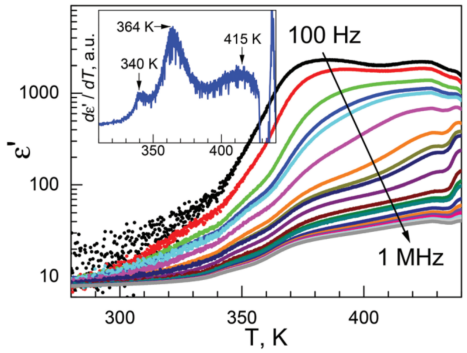

Figure 5.10: Temperature-dependent traces of the (real) dielectric permittivity (ϵ') on heating for HMF as a function of field frequency and inset $\mathrm{d}\epsilon'/\mathrm{d}T$ plot at a field of 1 MHz.[69]

In addition to the dielectric properties, Chen et al. described prominent anisotropic thermal expansion. It was found that with increasing temperature the channel diameters

reduced but channel lengths expanded. This reduction of channel diameter started gradually before the phase transition at 350 K and then increases considerably at the transition. It was suggested that the framework accommodates the motion of the hydrazinium ions which causes the anisotropic thermal expansion properties.

5.4 Experimental Methods

Samples of HMF and partially deuterated HMF (dHMF) were synthesised and provided by the group of Paul Saines, University of Kent. The synthesis of dHMF was designed such that only the hydrazinium cations were deuterated. The white powders of HMF and dHMF were packed into 4 mm zirconia rotors.

^{1}H NMR experiments were carried out on the HMF sample using a Bruker Avance III HD spectrometer at 400.17 MHz using a Bruker 5 mm static probe where, in the interests of sample conservation and preserving sample history, the packed rotor from MAS experiments was placed inside the 5 mm glass tube sample holder. ^{1}H spectra were acquired using a solid echo pulse sequence with an inter-pulse delay of 15 µs, and FWHM of resonances were determined using TopSpin 3.0.

Variable temperature ^{2}H, ^{13}C and ^{15}N NMR experiments were carried out using a Bruker Avance III HD spectrometer at frequencies of 76.71 MHz, 125.65 MHz and 50.64 MHz respectively using a Bruker 4 mm MAS probe. ^{2}H spectra were taken on static samples with a 90 ° static echo pulse (6.4 µs) and an inter-pulse delay of 55.2 µs. ^{13}C and ^{15}N spectra were acquired using 10 kHz MAS and CP. ^{2}H spectra were fitted to sums of quadrupolar lineshapes using SOLA in TopSpin 3.0.

5.5 Results

The following results are based on the article: 'A new avenue to relaxor-like ferroelectric behaviour found by probing the structure and dynamics of $[NH_3NH_2]Mg(HCO_2)_3$'.[84] *Diffraction studies were run and analysed by Thomas Hitchings and Paul Saines.*

5.5.1 Diffraction

In the low temperature structure, SCXRD confirms the structure reported by Chen et al. There is chirality in the framework and the hydrazinium ions lie perpendicularly in pores packed antiparallel to each other along channel direction. However, single-crystal neutron diffraction (SCND) showed additional disorder that could not be observed through XRD. The disorder was modelled by splitting the NH_2 group across two positions (N2a and N2b), as shown in Figure 5.11a. The two nitrogen positions had one associated distinct hydrogen position (H2a and H2b) and one hydrogen position between the nitrogen positions (H3). The nitrogen associated with the NH_3 end was not modelled with any significant disorder.

There is evidence of hydrogen bonds both between the cations and the formate as well as between NH_3 and NH_2 groups on adjacent cations. Disorder is also found in the framework with the hydrogen atoms in the three crystallographically distinct formate ions being modelled as split across two positions as shown in Figure 5.11b

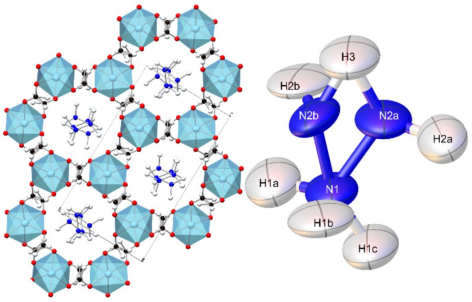

(a) Low temperature structure: cation disorder within channels.

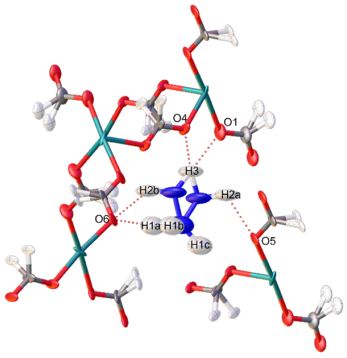

(b) Low temperature structure: cation and framework disorder.

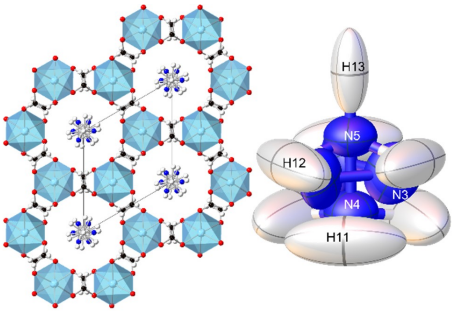

(c) High temperature structure: cation disorder within channels.

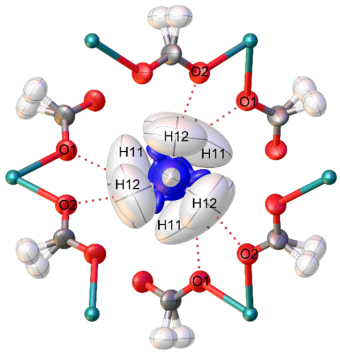

(d) High temperature structure: cation and framework disorder.

Figure 5.11: Crystal structures of HMF modelled from the SCND: (a) and (b) low temperature orthorhombic $P2_12_12_1$ crystal structures; and (c) and (d) high temperature hexagonal $P6_3$ crystal structures. Diagrams made by Tom Hitchings.[84]

In the high temperature structure, previous XRD studies from Chen et al. suggested a single N position in a $P6_3$ cell.[69] Modelling from SCND gave an additional two nitrogen positions, centered around the 3-fold axis which lies along the pore direction. This is shown in Figure 5.11c. The modelling shows a fraction of cations have reoriented along the pore direction, as was described by Chen et al., however the new modelling shows some hydrazinium ions remain perpendicular to the pore even in the high temperature phase. Full modelling of the SCXRD data in the high temperature phase is difficult due to the substantial disorder particularly of the perpendicular cations. There was also disorder on the formate ion as shown in Figure 5.11d. The diffraction study exhibits some residual scattering along the channel axis, as shown in Figure 5.12. This is ascribed to an additional H site between parallel cations but this is not directly observed in the NMR.

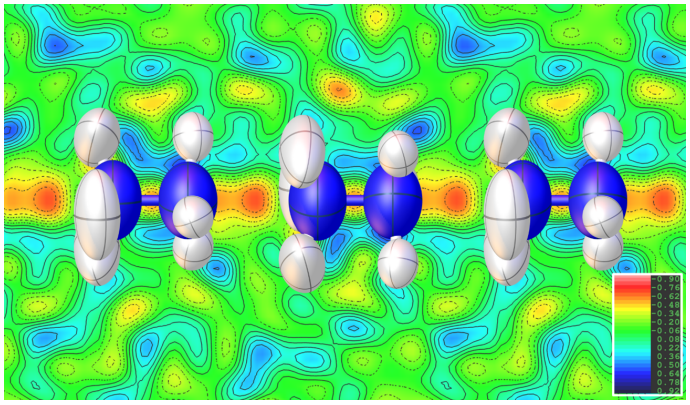

Figure 5.12: Scattering from SCND from parallel cation molecules in HMF. Experimentally observed nodes of negative scattering (red) between cations. The transient proton site between cations is omitted to display the residual negative scattering. Diagram made by Tom Hitchings.[84]

5.5.2 NMR

5.5.2.1 Lineshapes

Figure 5.13 gives the recorded ^{2}H and ^{13}C of dHMF and ^{15}N spectra of HMF at varying temperatures denoted by the position of the baseline with respect to the temperature scale on the vertical axis. The ^{2}H and ^{15}N spectra reflect changes in the dynamics of the cation, while the ^{13}C spectra are sensitive to changes to the host framework, as measured from the formate ion. There are three distinct temperature regions seen clearly in the ^{2}H and ^{13}C spectra and to a lesser extent the ^{15}N spectra. These regions, also observed in ^{1}H lineshape data (Figure 5.18 on page 80), match well to the behaviour observed in the DSC and the dielectric permittivity datasets given in Figure 5.7 Figure 5.10 respectively,[69] in which there is a complex multi-step transition between 300 and 350 K with the main phase transition at 350 K. There was no evidence of significant temperature hysteresis; spectra given were acquired with increasing temperature, however spectra taken with reducing temperatures were indistinguishable. This indicates there was no degradation of sample through heating cycles to temperatures no greater than 400 K.

There is evidence of the nature of the temperature transitions from the ^{13}C spectra. The intermediate region has features of both the high and low temperature regions consistent with a first order transition, but there is a clear evolution of the low temperature structure towards the high temperature limit, i.e. the intermediate region is not a simple first order transition involving separate domains of two materials.

As found in the diffraction, the low temperature structure has three crystallographically distinct formate ions in the unit cell. This is seen in the ^{13}C spectra with the two peaks seen in an approximate 2:1 ratio. However there is a continuous distribution of chemical shifts between 170 – 175 ppm, implying a distribution of local formate environments. This can only be explained in terms of significant static disorder of the framework in the low temperature region.

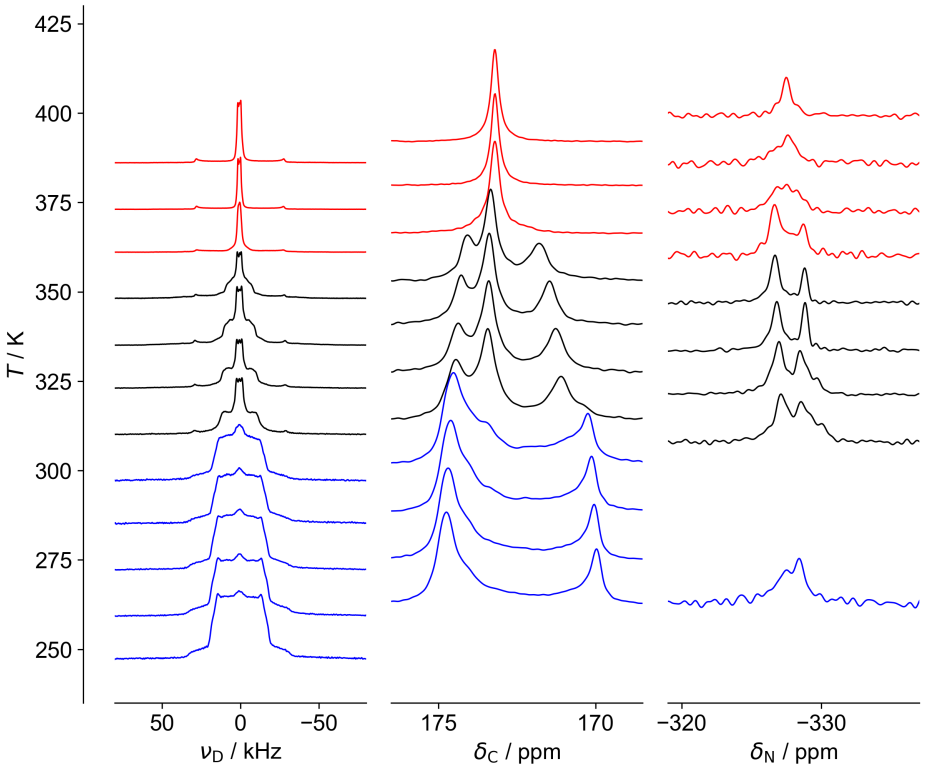

Figure 5.13: NMR spectra as a function of temperature (baseline of each spectrum indicates sample temperature). Left: ^{2}H static spectra of dHMF at 76.71 MHz. Centre: ^{13}C spectra of dHMF at 125.65 MHz and 10 kHz MAS. Right: ^{15}N spectra of HMF at 50.64 MHz and 10 kHz MAS. The three distinct temperature regimes observed are highlighted using colour: high temperature phase (red); low temperature phase (blue); and intermediate regime (black).

Due to intrinsically poor NMR receptivity, ^{15}N spectra have low signal-to-noise which can make the ^{15}N spectra more difficult to interpret. Sites have been fitted in Topspin 3.0 with fits shown in Figure 5.14 and fitted parameters are given in Table B.1 in Appendix B. The two peaks seen in the intermediate temperature region could be naively assigned to the NH_3 and NH_2 groups of hydrazinium ions. However, there are two distinct cation populations in the intermediate regions (see explanation below), and so it is likely that the two resonances actually refer to the two populations. This is supported by the fact that in the low temperature region, where there is only one type of hydrazinium ion present, the two peaks corresponding to the NH_3 and NH_2 groups are not well resolved. The most conclusive feature of the ^{15}N spectra is the distinctive coalescence of the two signals at approximately 370 K. This could be the two populations of hydrazinium ion exchanging at high temperatures. This exchange is slow at approximately 200 Hz, the linewidth of the coalesced peak, and hence not likely to be the H^+ exchange seen in the diffraction. Due to the relatively slow rate, the exchange is not expected to affect the ^{2}H spectra even at the highest temperature measured here.

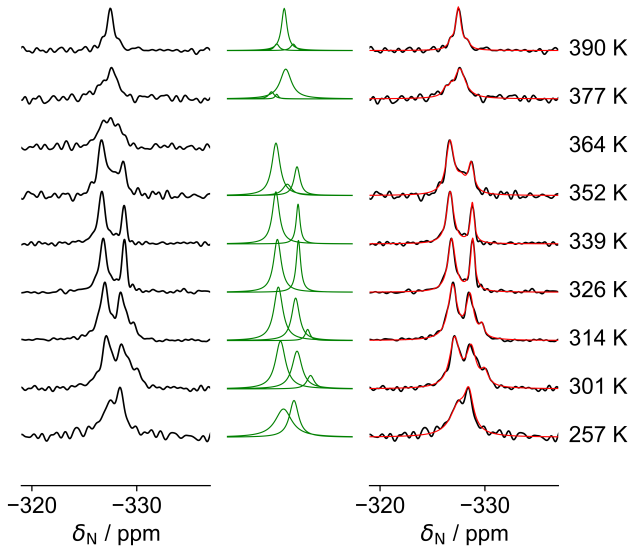

Figure 5.14: ^{15}N at 50.64 MHz and 10 kHz MAS spectra as a function of temperature. Left: ^{15}N data. Centre: fitted sites Right: overall fit (red) overlaid on spectra (black).

Figure 5.15 shows one characteristic ^{2}H spectrum for each temperature region. They were fitted using SOLA in TopSpin 3.0, with the fits summarised in Table 5.1. The lowest temperature spectrum (259 K) has been fitted to two sites: one with a C_Q of 43 kHz and a low asymmetry parameter, η (blue), and a second component with smaller C_Q (green) is required to fit the overall shape. Since it follows the outer shape of the experimental spectrum, the blue fitted values are given with confidence. The green fit is required to increase the central portion of the overall fit and hence is not a direct fit to any part of the experimental spectrum. This fit is given with much less confidence.

Table 5.1: Fitting parameters for the ^{2}H NMR spectra of Figure 5.15.

	259 K		**335 K**				**386 K**		
Fractional integral	0.68	0.32	0.17	0.58	0.23	0.01[a]	0.34	0.65	0.01[a]
$\boldsymbol{\delta_{iso}}$ **/ ppm**	6	7	4	10	9.4	8	3	9.1	9
$\mathbf{C_Q}$ **/ kHz**	43	20	77	21	5.0	0	75	3.0	0
$\boldsymbol{\eta_Q}$	0.13	0.8	0	0.2	0	0	0	0.03	0
LB[b]**/ kHz**	2	3	1.5	2.6	0.8	1.2	1.1	0.8	0.6

Fitting values are given to the number of significant figures required for a satisfactory visual fit of the data.

[a] Used to 'fit out' a zero-frequency component: not physically significant.

[b] Lorentzian line broadening.

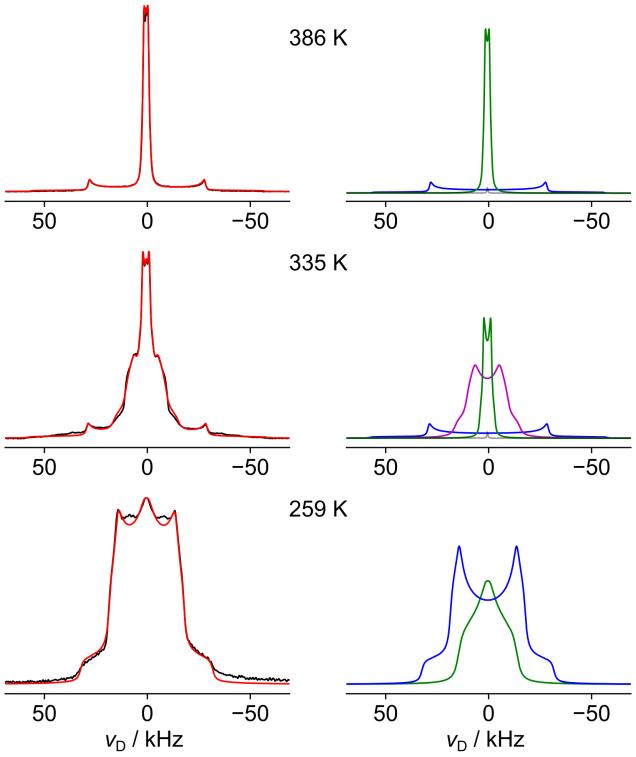

Figure 5.15: Fitting of representative ^{2}H NMR spectra of dHMF at 76.71 MHz from low, intermediate and high temperature regions. Left: experimental spectrum (black) and overall fitting (red). Right: individual fitting components: high C_Q (blue) and low C_Q (green). Additional components were required in some fittings: intermediate C_Q (purple) and a small zero-frequency spike (grey).

The 43 kHz C_Q, low η fit (blue) on the low temperature fit in Figure 5.15 likely corresponds to an N–D bond undertaking a symmetrical rotation which, based on the symmetry of the crystal and the molecule, will be a C_3 jump. A C_Q of 43 kHz is significantly smaller than would be expected for an isolated spin undertaking that motion (≈ 77 kHz[†]), however it is consistent with a strongly hydrogen bonded site undergoing a C_3 jump.[85] The lower C_Q, higher η fit (green) is more complex to explain. Figure 5.16 simulates the effect of η and C_Q of a 3-site jump with non-equal probabilities. The x axis varies by the population of A and the remaining population is shared between two other sites. A typical C_3 jump with equal populations is represented by A = 0.33, which gives $\eta = 0$ and $C_Q/C_Q(0) \approx 0.33$ as expected from the footnote. As the population is moved even a small amount away from three equal populations (e.g. A = 0.4) the η value becomes much larger very quickly. This mimics the motion of the ND_2 bonds (and the lone pair) in a non-symmetric potential and possibly explains the higher η value. The ratio between the low and high η sites is 0.68:0.32 which is different to the 0.6:0.4 expected from a straight division of NH_3 and NH_2 groups. This could be due to the errors of the fit of the high η

[†]A static deuterium lineshape is typically 200 kHz. In the event of a C_3 rotation this will be scaled by approximately $\cos(70.5\,^\circ) = 0.33$ resulting in a lineshape of 200 kHz × 0.33 = 77 kHz.

spectrum or experimental reasons such as relaxation losses in the echo period. Alternatively, it could be because 20 % of the ND_2 sites are in a symmetric potential resulting in a larger than expected low η site.

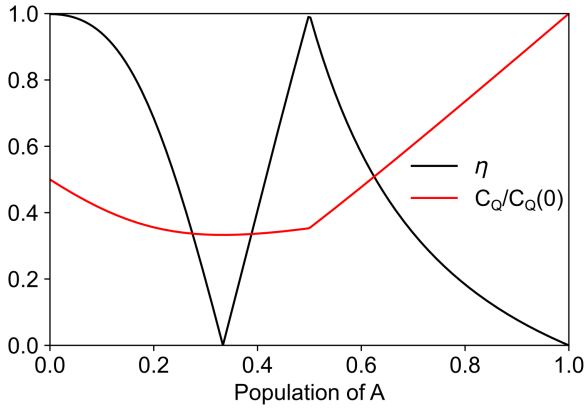

Figure 5.16: Dependence of the averaged quadrupolar coupling tensor in the limit of fast exchange between three sites as a function of the population of site A, the other two sites sharing the remaining population equally. The cone angle is 70.5 °. Data calculated using NMR Weblab.

The high temperature ^{2}H spectrum (386 K) in Figure 5.15 also fits to two components. The broader site (blue) again fits to a low η value and is consistent with a C_3 jump rotation. However the C_Q is larger than the low temperature fit (77 kHz vs 43 kHz) and is consistent with a rotation unhindered by hydrogen bonding. There is also a very narrow site ($C_Q \approx 3$ kHz) implying there is a very mobile component at this temperature undergoing (almost) isotropic rotation.

The intermediate temperature ^{2}H spectrum (335 K) in Figure 5.15 has both the site undergoing an unhindered C_3 jump and the isotropic site seen in the high temperature spectrum. Additionally there is an intermediate site which fits to a C_Q of 21 kHz. As seen in Figure 5.17, this is the only site which varies within a temperature region. This is likely attributed to an exchange-type process, happening around 200 kHz between 310 – 348 K. This could be an exchange between ND_2 groups in symmetric and asymmetric sites, as described in the low temperature fit. Alternatively, since there is no discrimination between the ND_2 and ND_3 sites in the intermediate and high temperature spectra (as there was in the low temperature) this could be from an exchange of H^+ intra- and/or inter-molecularly.

The relative intensities between sites should not be over interpreted. With an echo delay of 55 µs it is possible that different sites have different T_2 relaxation times and hence the ratio of integrals recorded here are not reflective of the true ratio. It should also be noted that MAS ^{2}H spectra were recorded, however no discrimination between sites were observed at any temperature.

The evolution of proton ^{1}H linewidths with temperature are given in Figure 5.18. Unlike the ^{2}H lineshapes, the ^{1}H data will have contributions from both the hydrazinium

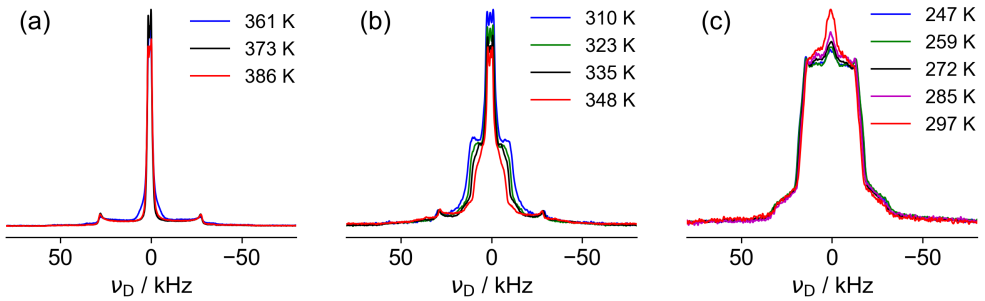

Figure 5.17: Overlaid ^{2}H spectra at 76.71 MHz with temperatures given on the right for (a) low temperature structure, (b) intermediate regime and (c) high temperature structure. Outer sections fixed by eye to allow relative spectral shape evaluations to be visible.

ion and the formate linker. Linewidths are analogous to the intermediate motions discussed in Section 4.4 showing that the ND_3 motion is fast even at 240 K. The gradual decrease of linewidth throughout the phases suggest the slow onset of an additional motion, be it from the hydrazinium ion or the formate linker. The sudden drops in the linewidth shows the MOF is entering a more dynamic phase.

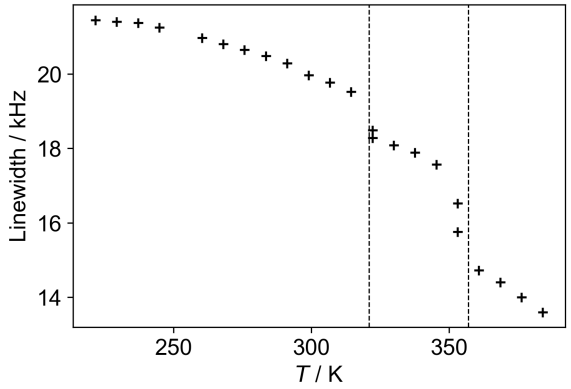

Figure 5.18: Static ^{1}H linewidth of HMF as a function of temperature at 400.17 MHz. Data taken by George Peat.[86]

5.5.2.2 Relaxation

Figure 5.19 shows the evolution of ^{1}H relaxation times as a function of temperature. Curves have been fitted based on Arrhenius equations and fitted parameters documented in Table 5.2. As discussed above with lineshapes, ^{1}H relaxation times could be sensitive to motions from the hydrazinium ion as well as the formate framework. Due to efficient ^{1}H spin diffusion, the measured relaxation rate will be a weighted sum of the relaxation rates of the different ^{1}H environments.

The minima in the T_1 and $T_{1\rho}$ relaxation times in the low temperature region likely correspond to the motions seen in the low temperature ^{2}H spectra. It is tempting to assume that the ^{1}H T_1 and $T_{1\rho}$ relaxation times are responding to the same motion since

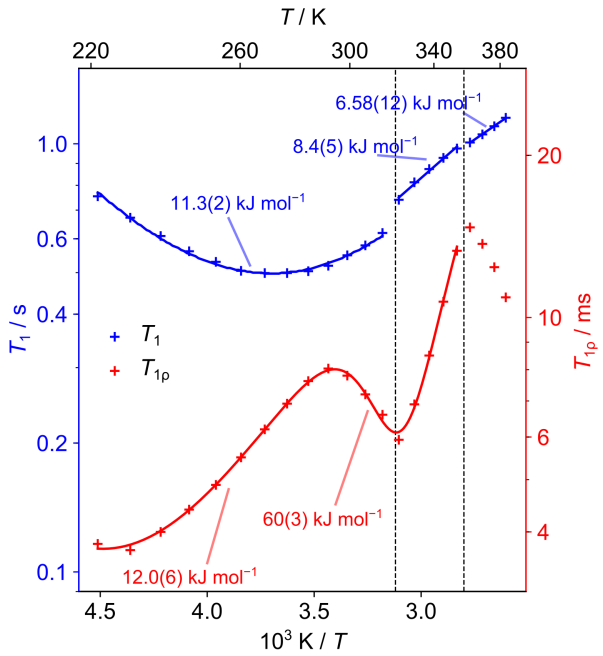

Figure 5.19: ^{1}H T_1 at 400.17 MHz (blue) and $T_{1\rho}$ at 50 kHz (red) relaxation time constants as a function of temperature. Error bars are not shown as they are of a similar magnitude to the size of symbols used. Curves show fits to relaxation models. $T_{1\rho}$ data fitted to two motions simultaneously, see Figure 5.20 for further explanation. Straight line fits for shorter data segments at higher temperatures are guides for the eye and these E_a values should be interpreted cautiously. Data taken by George Peat.[86]

the activation energies are compatible, however the rates of motion are not compatible: the rates over the temperature range 220 – 300 K are 200 – 1000 MHz for T_1 and 50 – 200 kHz for $T_{1\rho}$. If the rates of motion from the NH_3 end and NH_2 end of the cation were sufficiently different, it is possible the different relaxation types were detecting the rotation of different ends. More likely is that both relaxation types are detecting a superposition of both NH_3 and NH_2, and perhaps even a contribution from the formate in addition, therefore the activation energies are not physically meaningful.

There is a jump in the ^{1}H T_1 relaxation times at the lowest temperature transition which is consistent with a sudden increase in the rate of motion. However, the activation energies fitted in the mid and high temperature regions must be treated with particular caution, as there is not only contributions from the hydrazinium cations and the formate framework as before, but also potentially from different cation populations.

The $T_{1\rho}$ was fitted in the low and mid temperature regions (222 – 353 K) to two motions simultaneously i.e. two motions, each with a separate E_a and $\log_{10}(\tau_0)$ but a common $\nu_1 = 50$ kHz as summarised by Equation 5.1. Fitting two motions simultaneously significantly changed the fitted parameters as shown in Figure 5.20 and despite two plausible independent fits shown in Figure 5.20a, the fitted parameters are not physically meaningful as they have not accounted for the 12.0(6) kJ mol^{-1} motion in the lower temperature region. The 12.0(6) kJ mol^{-1} fit was unaffected by the simultaneous fitting

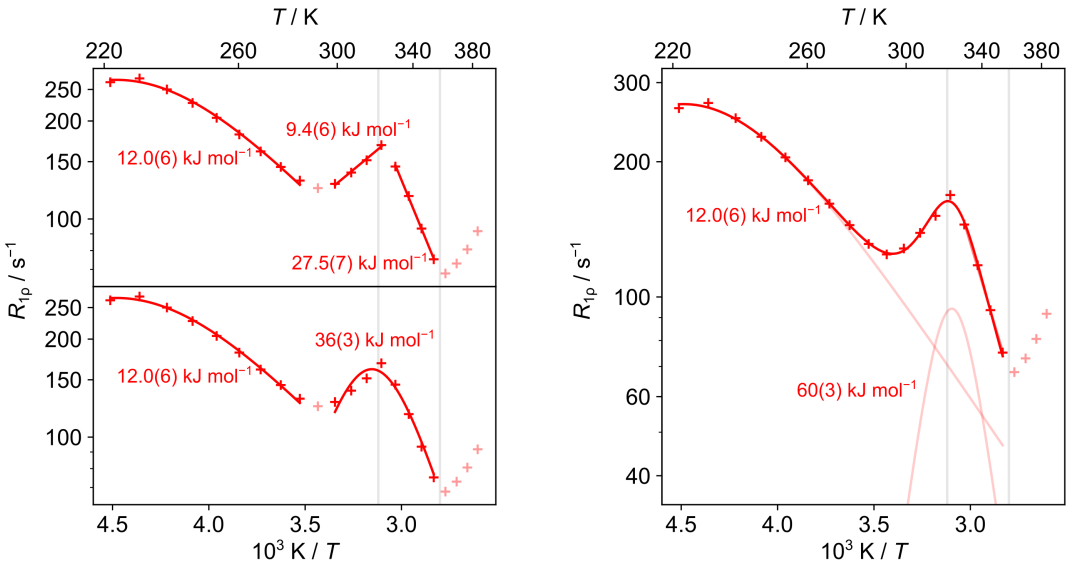

(a) Independent fittings.

(b) Combined fitting

Figure 5.20: Possible fits of the low and mid temperature region of ^{1}H $R_{1\rho}$. Left: two options (top and bottom) for fitting regions independently. Right: fitting the whole region simultaneously to two motions with a common ν_1, equivalent to T_1 plot in Figure 5.19. Pink lines show individual components which add (in $R_{1\rho}$) to give the overall fit.

because the higher energy motion quickly becomes insignificant away from its minimum.

$$T_{1\rho}{}^{-1} = A_1 J_1(\nu_1, \tau_{c1}) + A_2 J_2(\nu_1, \tau_{c2}) \tag{5.1}$$

The $T_{1\rho}$ minimum which fitted to $E_a = 60(3)\,\mathrm{kJ\,mol^{-1}}$ likely relates to the reduction of the ^{2}H linewidth of the intermediate site in the intermediate temperature. It is possible that this represents the whole molecule movement of the hydrazinium ion as this has previously been measured to be $67\,\mathrm{kJ\,mol^{-1}}$ (reported as $16\,\mathrm{kcal\,mol^{-1}}$) in $Li(N_2H_5)SO_4$.[87] If this is the case here, it is plausible that a large scale motion of the cation causes the phase transition, which is consistent with the reduction of $T_{1\rho}$ starting before the phase transition.

The decrease in $T_{1\rho}$ relaxation times in the high temperature region likely relates to the narrowing of ^{1}H linewidths in this region. The region can be fitted simultaneously with the $<290\,\mathrm{K}$ values to a motion of $59.97\,\mathrm{kJ\,mol^{-1}}$ as shown by Figure 5.21. Hence this could be the re-emergence of the same dynamics seen in the mid temperature region happening at a slower rate due to the phase change. Although it should be noted due to the separation between the two fitted temperature regions, the higher temperature region could be fitted to any value between $35-85\,\mathrm{kJ\,mol^{-1}}$. The high temperature region could be sensitive to the interchange between aligned and dynamic protons, which would be consistent with the coalescing ^{15}N spectra (Figure 5.13 on page 76).

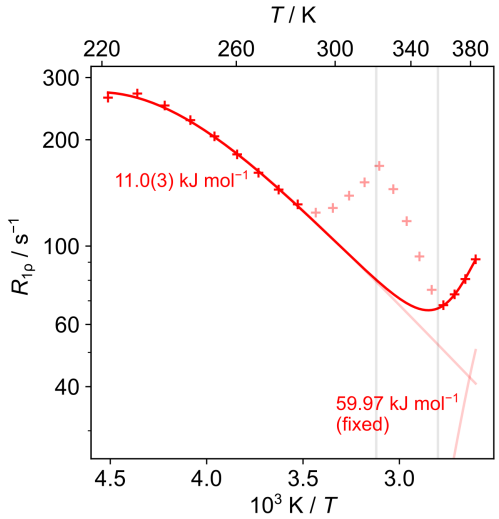

Figure 5.21: ^{1}H $T_{1\rho}$ relaxation times fitted to the low and high temperature regions (darker crosses) simultaneously. The activation energy of the higher energy process was fixed at 59.97 kJ mol^{-1} (the exact value of 60(3) kJ mol^{-1} from the fitting in Figure 5.19). The lower energy process is fitted to E_a = 11.0(3) kJ mol^{-1} and $\log_{10}(\tau_0$ / s) = −8.11(4) and the higher energy process fitted to $\log_{10}(\tau_0$ / s) = −13.25(6).

Deuterium T_1 relaxation times, shown in Figure 5.22 are much less informative than the ^{1}H relaxation times. The lower temperature data showed some deviations from single exponential behaviour, but a simple single-exponential fit was used to capture the temperature dependence, and show that this is consistent with the more extensive ^{1}H relaxation data. All parameters fitted from relaxation times are summarised in Table 5.2.

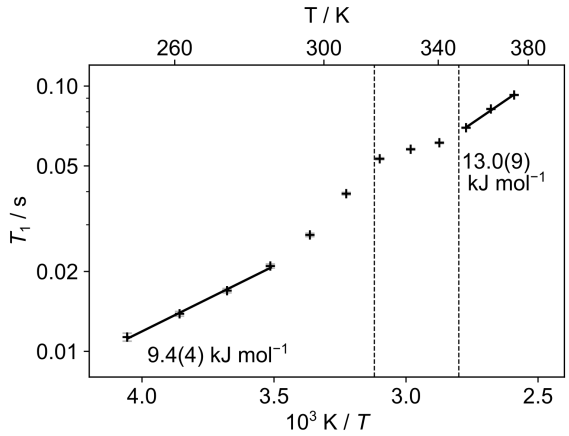

Figure 5.22: ^{2}H T_1 relaxation time constants as a function of temperature for static samples of dHMF at 76.71 MHz. The data was acquired using saturation recovery experiments.

Table 5.2: Summary of the fitted parameters from the relaxation data of HMF.

Relaxation Type	Temperature range / K	E_a / kJ mol^{-1}	$\log_{10}(\tau_0$ / s)	$\log_{10}$(A / Hz)
^{1}H T_1	222–314 (Low)	11.3(2)	−11.79(4)	9.248(2)
	322–353 (Mid)	8.4(5)	-	-
	361–384 (High)	6.58(12)	-	-
^{1}H $T_{1\rho}$	222–353	12.0(6)	−8.36(11)	7.926(9)
	(Low & Mid)	60(3)	−15.3(5)	7.471(13)
	222–276 & 361–384	11.0(3)	−8.11(4)	7.932(9)
	(Low & High)	59.97[a]	13.25(7)	7.37(5)
^{2}H T_1	247-286 (Low)	9.4(4)	-	-
	348-386 (High)	13.0(9)	-	-

[a] Fixed parameter

5.6 Conclusion

The combination of SCND and solid-state NMR has proved essential for analysing the structure and dynamics in HMF. It has been confirmed that the main phase transition is caused by the reorientation of hydrazinium ions from perpendicular to parallel in the channels. It is also highly likely that the hydrazinium molecules start reorienting before the phase transition, as indicated by the ^{1}H $T_{1\rho}$ minimum, which gave an activation energy consistent with whole molecule reorientation starting 60 K below the phase transition. It is also consistent with the anisotropic thermal expansion recorded by Chen et al., where the reduction of channel diameter starts gradually before the phase transition. It could be that a small number of hydrazinium ions reorient to reduce steric pressure by aligning along the channels. This realignment causes further reduction of pore diameter which causes further cations to reorient. This starts below the main phase transition and continues until a critical value where there is an energetically favourable number of parallel and perpendicular cations.

While ^{1}H relaxation measurements have given motional parameters, it is the spectra that have proved very useful for understanding the nature of the material. ^{2}H spectra have shown that there are two population of cations, one of the cations is highly mobile, whilst the other is in a symmetric potential. The interconversion of these populations in the high temperature phase must be slow compared to the deuterium linewidth ($\approx$ 100 kHz) but fast relative to the ^{13}C and ^{15}N linewidth ($\approx$ 500 Hz). ^{13}C spectra have also shown that there is a distribution of local environments in the the low temperature phase indicating static disorder of the framework.

Relating the structural and dynamic information of the material to the relaxor ferroelectric behaviour is not straightforward. The findings are not incompatible with the most common explanation for relaxor ferroelectrics involving polar nanoregions. There is a combination of parallel and perpendicular cations and if the polar parallel cations were found in small domains within the non-polar perpendicular cations, this would be

consistent with the common 'polar nanoregion' hypothesis. However, in the data presented here, much like in the literature, there is no direct evidence for the existence of polar nanoregions.

Relaxor ferroelectricity is fundamentally a frequency dependence of the dielectric response. From an NMR perspective, when there is a thermally activated process with an activation energy, there is a frequency dependence of the response; T_1 relaxation curves, for example, are frequency dependent and will be different when measured at 100 MHz compared to 500 MHz. If the dielectric permittivity is comparable, then the relaxor ferroelectric response is not found despite the dynamic molecules but directly because of the thermally activated dynamics.

Chapter 6

Characterising the Dynamics of Solvent Molecules in Pharmaceutical Cocrystal Solvates

6.1 Cocrystal Solvates

Cocrystals are multicomponent crystals formed between two or more compounds. They have a different crystal structure to their starting compounds and because of this, cocrystals will have different physicochemical properties. This has been utilised in many areas of research,[88] such as explosives[89] and pigments,[90] but particularly in pharmaceuticals.[91–95]

The pharmaceutical industry is particularly interested in the improvement of physicochemical properties in the solid form, since the majority of medicines are taken as a solid. Improvements in properties such as stability and powder flowability have a direct impact in practical aspects of drug manufacture, such as processing and storing.[96] Most important though, are improvements to solubility, as this has a direct impact on bioavailability. Hence cocrystallisation is potentially a route to making an active pharmaceutical ingredient (API) with prohibitively poor solubility, viable as a product.

Trapped solvent molecules are also very common in pharmaceuticals; it is estimated that up to a third of all APIs can form hydrates.[97] When the crystal packing of a host lattice is relatively inefficient, solvates can be found in the channels or voids in the lattice. Solvent molecules can create strong interactions and hydrogen bonding with APIs to form flexible clusters which can improve stability.[98,99] Alternatively, solvent molecules can simply fill the spaces without strong interactions with the framework,[100] which reduces the free energy of the crystal compared to the non-solvated form.[101]

Included solvent molecules are frequently dynamically disordered. Despite the potential benefits of solvates, disorder is a potential risk in the pharmaceutical industry, as it is assumed to reflect some degree of metastability. However, solvent dynamics could be providing entropic stabilisation and hence disorder may be intrinsic to the stability of a phase and not necessarily a marker of instability.

6.2 Furosemide-Picolinamide

Furosemide (FS) is a very important compound in medicine; it is on the World Health Organization's List of Essential Medicines in 2019[102] and it was the twentieth most prescribed medication in England in 2020/21.[103] It is a potent loop diuretic and is primarily used in relieving fluid accumulation (edema) in the heart, liver or kidney, but can also be used to treat high blood pressure. It does, however, have relatively poor aqueous solubility ($6\,\mathrm{mg\,dm^{-3}}$) particularly at physiological pH range.[104] This poor solubility limits bioavailability, hence cocrystallisation of FS has been widely investigated as a route to improving its solubility.[16,105] The molecular structure of FS is given in Figure 6.1a.

Picolinamide (PA) has been described as a 'promising coformer' and is one of the many molecules screened when formulating pharmaceutical cocrystals.[106] Its molecular structure is given in Figure 6.1b.

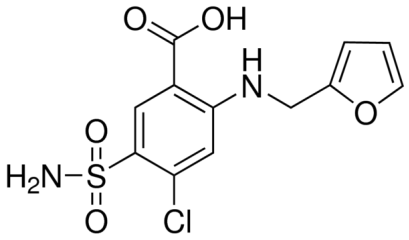

(a) Furosemide (FS)

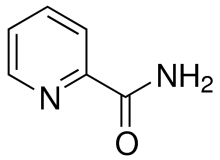

(b) Picolinamide (PA)

Figure 6.1: Molecular structure and the components of the cocrystal FSPA.

The following chapter is dedicated to understanding the dynamics of two solvent molecules in two isostructural cocrystal solvates of FS and PA: FSPA acetone and FSPA ethanol. Results are documented in two halves with ideas in the first section focusing on information understood from NMR in isolation. This 'traditional' analysis uses lineshape and relaxation data to model molecular motions and is represented by the shaded region of the pictorial chapter overview in Figure 6.2. The second part of the chapter describes how the full understanding of the dynamics can only be understood from molecular dynamics (MD) simulations, represented by the red boxed region of Figure 6.2.

NMR analyses rely on the assumption that the motions are thermally activated i.e. motions that have an energy barrier, an activation energy, a correlation time that is dependent on temperature and an amplitude of motion that is independent of temperature. These assumptions are implicit in relaxation fitting equations (given in Section 2.2 on page 7) as well as in modelling jump-type motions in EXPRESS[18] or Weblab.[19]

The MD simulations herein show that the motion of solvent molecules in both solvates has a strong librational character. These wobbling-type motions do not have an energy barrier and hence do not have an activation energy. For barrierless motions, in contrast to barrier motions, increasing the temperature increases the amplitude of the motion but correlation times remain constant.

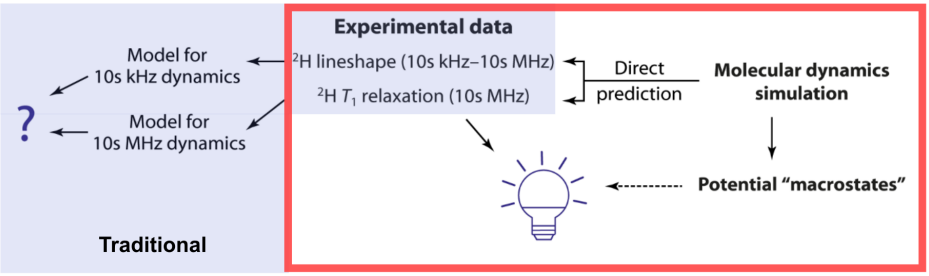

Figure 6.2: Pictorial chapter overview adapted from the manuscript in preparation. In the 'traditional' approach (shaded), NMR data is analysed using distinct models for lineshapes and relaxation times to produce a motional model. Results from this are only physically meaningful if motions are thermally activated. Reconciliation between the two sets of data fails if motions are complex or are barrierless. In this case, to correctly interpret the data, MD simulations have been run and are verified by NMR data, highlighted by the red box.

An overview of the motions of the solvate molecules determined by MD simulations are given in Figure 6.3 with schematic energy profiles alongside. It shows that the acetone molecules have significant librational character represented by the barrierless energy profile in blue. There are also four distinct 'macrostates' reflecting the C_2 symmetry of the molecule and the inversion symmetry. Jumps between macrostates are likely thermally activated which is shown as a barrier-type energy profile in green. Ethanol molecules have a complex mix of librational and jump character without distinct macrostates which is simplified by the low barrier energy profile in blue.

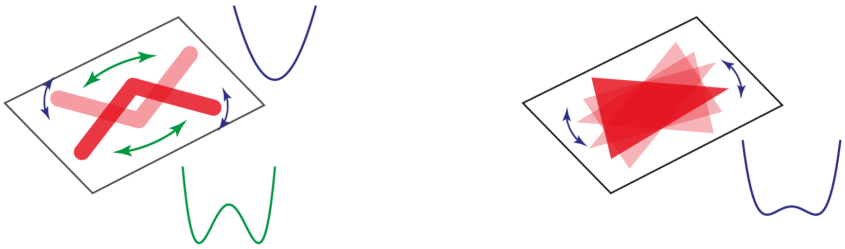

(a) FSPA acetone (b) FSPA ethanol

Figure 6.3: Cartoon representation of the resulting motions of (a) acetone and (b) ethanol with associated schematic energy profiles.

The MD simulations showed that the 'traditional' way of analysing molecular motions with NMR data is flawed when the motion has no energy barrier, or is a combination of barrier and barrierless motions as is the case here. Individual lineshapes have been fitted to models and relaxation times convincingly fitted which provide parameters such as activation energies and rates. However, the MD simulations show that these values are not physically meaningful as initial assumptions fundamental to the analysis are incorrect.

There are relatively few studies looking at the dynamics of solvent molecules trapped in cavities. The study below highlights how NMR data analysed in isolation can give misleading rates and motion types, and it is the combination of MD and NMR

that results in an accurate understanding of dynamics. It is hoped that principles used here may become a blueprint for understanding motions of trapped solvent molecules in the future.

6.3 Experimental Methods

6.3.1 Sample Preparation

Fresh FSPA acetone and FSPA ethanol solvate samples were prepared by liquid-assisted grinding of 1:1 molar quantities of the starting materials, 0.165 g FS (0.5 mmol) and 0.061 g PA (0.5 mmol). For the acetone solvate, FS and PA were ground in 1 mL acetone for 5 min. A further 1 mL was added and after 5 min a further 0.5 mL acetone was added every 10 min until the total grinding time was 30 min. A deuterated acetone solvate was produced by the same method using acetone-d_6. For the ethanol solvate, the FS and PA components were dry ground for 5 min before 10 drops of ethanol were added every 5 min until the total grind time was 1 h. A deuterated ethanol solvate was produced by the same method using ethanol-1,1-d_2, from here on called ethanol-d_2. Both syntheses yielded slightly damp cream powders, which were left to dry in air for 1 h before packing in 4 mm rotors for subsequent MAS NMR studies. Samples were stored in the rotor to limit desolvation. ^{13}C MAS NMR confirmed that the deuterated samples were identical to their non-deuterated analogues.

6.3.2 Experimental Details

High-resolution solid-state NMR spectra were obtained using either a Bruker Avance III HD spectrometer operating at ^{1}H, ^{13}C and ^{2}H NMR frequencies of 499.70 MHz, 125.65 MHz and 76.71 MHz respectively, or a Bruker Avance III HD spectrometer operating at the corresponding frequencies of 400.17 MHz, 100.62 MHz and 61.42 MHz. Samples were packed into 4 mm zirconia rotors. The ^{2}H shift scale was referenced with respect to neat TMS by setting the peak of D_2O to 4.81 ppm. The ^{13}C shift scale was referenced with respect to neat TMS by setting the highest frequency peak of adamantane to 38.5 ppm.

Variable-temperature ^{2}H static spectra and T_1 relaxation data were acquired at 76.71 MHz for the FSPA acetone-d_6 sample and 61.42 MHz for the FSPA ethanol-d_2 sample. FSPA acetone-d_6 spectra had a 1 s recycle delay and a 60 µs echo delay. FSPA ethanol-d_2 spectra had a 0.2 – 0.5 s recycle delay and a 40 µs echo delay.

^{2}H T_1 relaxation measurements were performed using a saturation recovery sequence for both samples, and single exponential decays were fitted to the integral of the complete sideband pattern as a function of recovery time. Excellent single-exponential fits were obtained at all temperatures on both samples. FSPA acetone-d_6 was measured under static conditions using 16 increments and a maximum recovery time ranging from 1.8 – 3.2 s. FSPA ethanol-d_2 was measured under 10 kHz MAS using 16 increments and a maximum recovery time ranging from 0.26 – 0.85 s.

^{13}C spectra of FSPA ethanol-d_2 were acquired at 100.62 MHz and 6 kHz MAS using

a 5 s recycle delay, 1800 transients, CP and TOSS to suppress sidebands. ^{13}C relaxation times were taken at 125.65 MHz, 10 kHz MAS, a 5 s recycle and between 128 – 2048 transients at each of the 10 delay times which were up to 51.2 s. Integrated areas of the solvent peaks were fitted to decaying single exponentials, although the fits were relatively poor due to low signal-to-noise.

The temperature dependence of relaxation times were fitted assuming a simple Arrhenius-like dependence of the motional correlation time, τ_c, on temperature, for details see Section 2.2. However, the fitting has been reparameterised to reduce the correlation between fitted variables and allows uncertainties to be propagated without the need for Monte Carlo (MC) simulations: detailed in Section 6.4.2.2.

6.4 Results

Single crystals of both FSPA solvates were obtained by crystallisation experiments carried out by Lorna Softley of the Ivana Evans group at the University of Durham. SCXRD studies revealed a unit cell with two pairs of FS and PA molecules in a unit cell. There was also additional electron density in a void at the inversion centre, suggesting the location of the disordered solvent molecules, however this was too disordered to be modelled. Illustrations of the unit cell of both solvates, including solvent molecules are given in Figure 6.4.

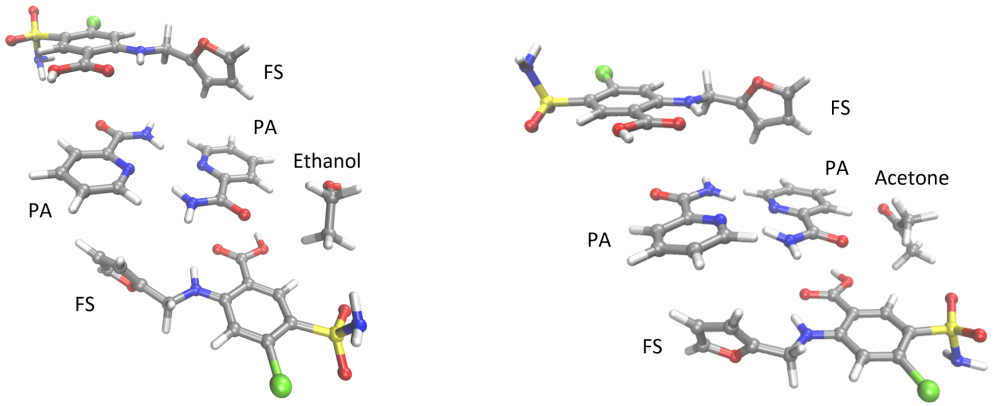

(a) FSPA ethanol (b) FSPA acetone

Figure 6.4: Illustrations of the unit cell of the FSPA cocrystal solvates derived from SCXRD experiments at 120 K.

^{13}C NMR is an easy way to prove that the grinding has also produced a cocrystal and not just a mixture of the two starting materials. Figure 6.5 shows the ^{13}C spectra of both reagents and both cocrystal solvates and it is clear that the peaks from reagents are not found in the cocrystals, confirming that they are indeed cocrystals. Coloured arrows indicate peaks from the solvate molecules. No peak splitting is observed which confirms that the asymmetric unit has a single molecule of each coformer. Very little difference is seen in the framework peaks of the solvates indicating that the two solvates

are isostructural. Full assignment of the framework peaks can be found in reference 16.

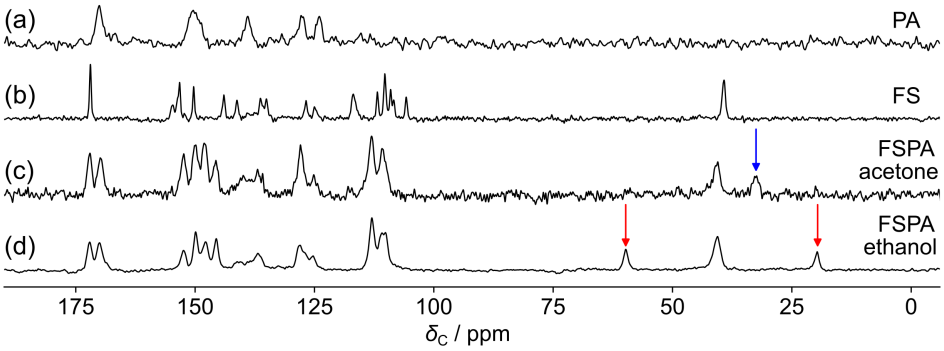

Figure 6.5: Reference ^{13}C MAS spectra of (a) PA, (b) FS, (c) FSPA acetone solvate and (d) FSPA ethanol solvate acquired at 125.65 MHz. Spectra (a)–(c) were acquired at 8 kHz MAS and spectrum (d) acquired at 5 kHz MAS. The recycle delay was 5 s and contact time 2.5 ms over 100 transients for all except (a) recycle delay 30 s with contact time 4 ms, (b) recycle delay 15 s with contact time 4 ms and (d) 480 transients. The blue arrow indicates the acetone CH_3 peak and the red arrows indicate the ethanol peaks. Adapted from reference 16.

6.4.1 FSPA Acetone-d_6

The ^{13}C spectrum shown in Figure 6.6 was used as a fingerprint and confirmed that the FSPA framework structure was identical to that previously reported by Kerr[16] and shown in Figure 6.5c. There was a small signal associated with the CH_3 group in the acetone molecule likely due to partially deuterated acetone molecules present in the original solvent. As documented by Kerr, the carbonyl carbon in the acetone molecule is not seen, due to inefficient CP likely caused by the weak dipolar couplings being averaged by dynamics.

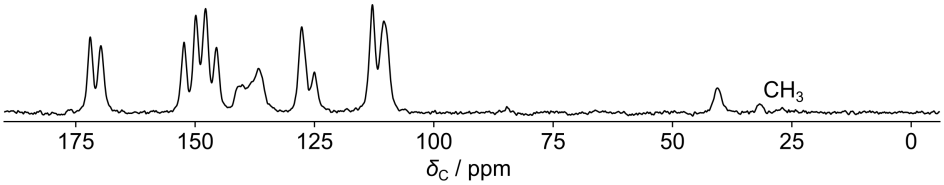

Figure 6.6: ^{13}C CP spectrum of FSPA acetone-d_6 acquired at 125.65 MHz. 8 kHz MAS was used with 480 transients with a recycle delay of 5 s.

The ^{2}H spectra of the FSPA acetone-d_6 are given at three temperatures shown in Figure 6.7a. The sharp peak in the centre of the experimental spectra at 235 K and 300 K is likely to reflect adventitious acetone. The spectra are relatively narrow at all temperatures, consistent with the fast dynamics of the CD_3 groups, even at 190 K. The changes observed as the temperature increases are consistent with the onset of a C_2 rotation about the C=O axis of the acetone molecule. Figure 6.7b shows the spectra of a 2-site jump of 115 ° predicted by EXPRESS[18] at jump rates from 10 kHz to 100 MHz, considered slow and

fast motions respectively in this regime. There is a good match between the experimental spectrum at 235 K and the predicted spectrum at 500 kHz. The other spectra do not fit as well, however it is clear that the experimental spectra are following a similar pattern to the modeled spectra.

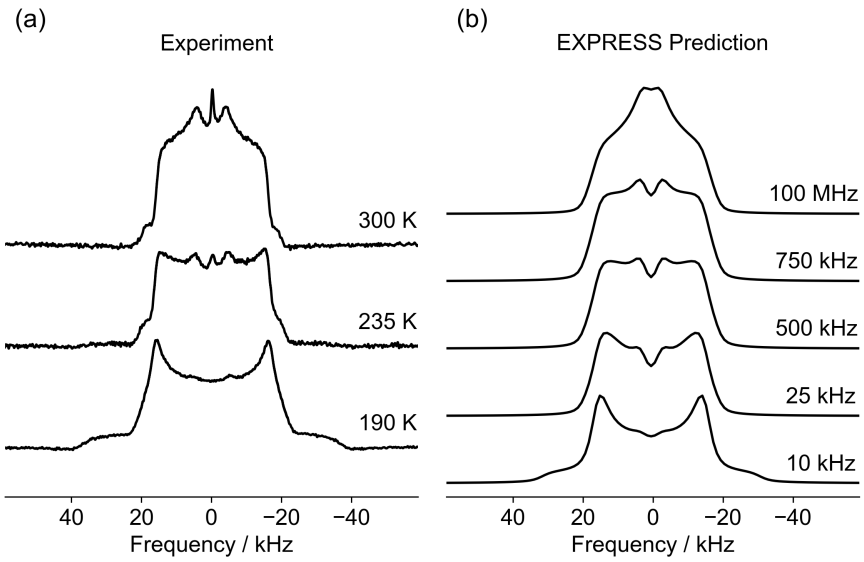

Figure 6.7: (a) Variable temperature static ^{2}H spectra of FSPA acetone-d_6 solvate at 76.71 MHz acquired with an echo delay $\tau = 60\,\mu s$ over 72000 transients. (b) EXPRESS[18] simulated static ^{2}H spectra over a 2-site jump motion of 115 ° *which assumes a barrier-type motion.* Data taken by Hannah Kerr, fitted parameters given in reference 16, with updated temperatures to reflect new understanding of probe temperature calibration.

Figure 6.8, shows the ^{2}H T_1 relaxation data, convincingly fitted to a straight line with an *apparent* $E_a = 7.9(2)\,kJ\,mol^{-1}$ derived from Arrhenius-type analysis. This is an unexpected result; $7.9\,kJ\,mol^{-1}$ is a very low activation energy, indicating a fast motion, perhaps akin to a methyl rotation, but the motion at 320 K is still slow compared the ^{2}H Larmor frequency (77 MHz), as shown by the negative gradient of the slope throughout. These two conclusions are seemingly incompatible.

The relaxation data also does not appear to be fully compatible with the spectra since the activation energy is significantly lower. Using 235 K = 500 kHz as a fixed rate and $E_a = 7.9\,kJ\,mol^{-1}$, gives a $\log_{10}(\tau_0 \,/\, s) = -8.25$. This value is compatible with the relaxation data; at the highest temperature in the relaxation graph, 320 K, the rate is 1.4 MHz which is less than 77 MHz. It is also consistent with the 300 K spectra giving a rate of 1.2 MHz. However, it is less consistent with the low temperature spectrum giving 190 kHz at 190 K, which is outside of a visual fit.

In summary, the NMR data collected on FSPA acetone-d_6 is strong with a clear activation energy derived from ^{2}H T_1 relaxation data and one rate of motion, given by ^{2}H spectra. However, despite the compelling data, it is difficult to relate the data to molecular behaviour.

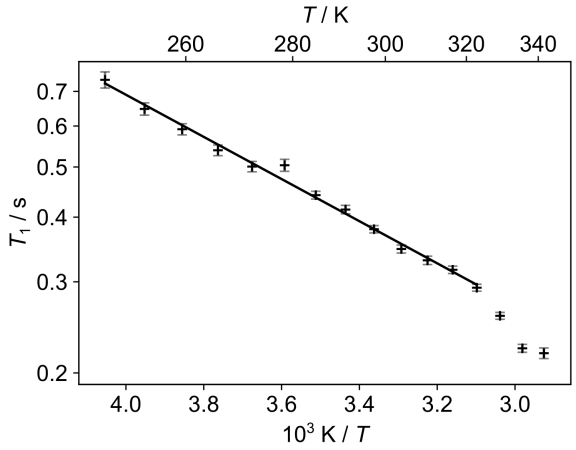

Figure 6.8: ^{2}H spin-lattice relaxation time constants as a function of temperature of FSPA acetone-d_6 at 76.71 MHz. Measured on a static sample using a saturation recovery sequence using a saturation train of 64 pulses. Each temperature had 16 increments with 64 transients and a maximum recovery time ranging from 1.8 – 3.2 s. The straight line fits to $E_a = 7.9(2)\,\mathrm{kJ\,mol^{-1}}$ *assuming an Arrhenius-type fitting.*

6.4.2 FSPA Ethanol

Figure 6.9 gives the ^{13}C spectra of FSPA ethanol as a function of temperature with the resonances from the ethanol solvate labelled. Both the framework and solvent resonances were identical to the spectrum previously reported by Kerr[16] (Figure 6.5). The solvent peaks did show change with temperature; the signal strength of the CH_2 resonance is broader in the 220 K and 200 K spectra and completely removed in the 185 K spectrum. The CH_3 resonance also shows some broadening, but only at 185 K. This is likely due to the motion of the solvent molecule entering a regime that interferes with experimental parameters such MAS rate or decoupling pulses as described in Section 2.4.2.

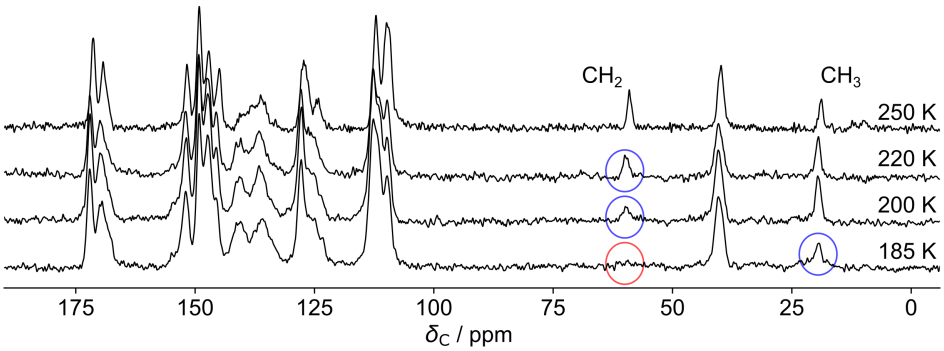

Figure 6.9: Variable temperature ^{13}C spectra FSPA ethanol at 125.67 MHz. Broadened signals highlighted in blue, unobserved signal highlghted in red.

Previously measured ^{13}C relaxation times of FSPA ethanol were taken by Kerr.[16] Contrary to expectation, the calculated activation energy of the motion affecting the CH_2 group was lower than the CH_3 groups ($8(2)\,\mathrm{kJ\,mol^{-1}}$ and $23(2)\,\mathrm{kJ\,mol^{-1}}$ respectively).

There were no uncertainties given for each relaxation time so it is unclear if these values were statistically meaningful or as a result of low signal-to-noise. Consequently, the experiments were repeated at the same field and the results are shown in Figure 6.10. Uncertainties have been calculated from linear regression analysis.

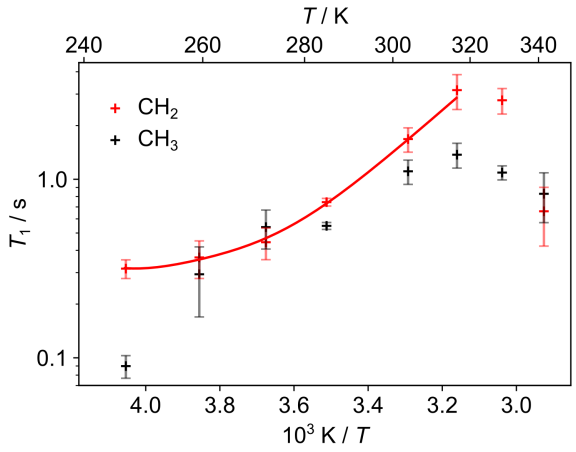

Figure 6.10: ^{13}C T_1 relaxation times of FSPA ethanol at 125.65 MHz and MAS rate of 10 kHz fitted to an Arrhenius model. Using the Torchia pulse sequence, the time delay was varied between 0.02 – 15 s in 8 steps with between 256 – 512 transients in each, using a recycle delay of 5 s. The curve is a fit of CH_2 experimental data to $E_a = 36(4)\,\mathrm{kJ\,mol^{-1}}$ and $\log_{10}(\tau_0 \,/\, \mathrm{s}) = -16.5(7)$ *assuming an Arrhenius-type fitting.*

Up to 310 K the overall picture is similar to the values reported by Kerr, however the CH_3 group is relaxing faster in the majority of temperatures which is more consistent with previous assumptions. Fitting the CH_2 relaxation times gave $E_a = 36(4)\,\mathrm{kJ\,mol^{-1}}$ and a $\log_{10}(\tau_0 \,/\, \mathrm{s}) = -16.5(7)$.

6.4.2.1 FSPA Ethanol-d_2

Due to low quality of the ^{13}C relaxation data, a new sample of FSPA ethanol-d_2 was synthesised. Ethanol-d_2, shown in Figure 6.11, was chosen over ethanol-d_5 to focus on the overall solvent motion, without complications due to methyl rotation. The alcohol proton must remain undeuterated as a deuterium atom here would exchange with exchangeable protons on the framework.

Figure 6.12 shows how the lineshapes of the deuterium spectra vary with temperature. It can be seen that there is a significant change in lineshape over this temperature

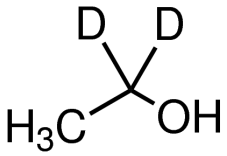

Figure 6.11: Ethanol-d_2

range. The spectrum taken at 185 K is close to being a classic static lineshape with some central features. The spectra at 235 K and above have lost the distinctive classic static lineshape and have an overall shape with a higher asymmetry.

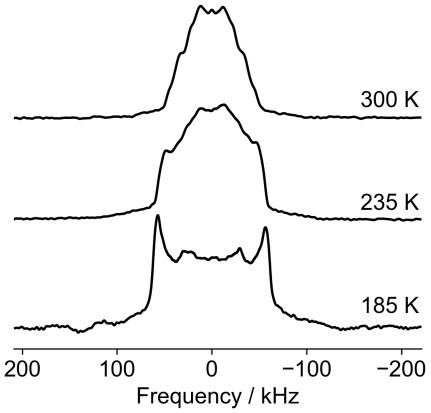

Figure 6.12: ^{2}H quadrupolar echo spectra of FSPA ethanol-d_2 spectra at 61.42 MHz. Recycle delays of 0.5 s, 0.2 s and 0.3 s were used with increasing temperatures and all were taken with 4096 transients or more and an echo delay of 40 µs.

The deuterium relaxation times are given in Figure 6.13. These were fitted to Arrhenius-type equations to give $E_a = 19.0(9)\,\mathrm{kJ\,mol^{-1}}$ and $\log_{10}(\tau_0 \,/\, \mathrm{s}) = -12.82(19)$. The biggest concern from this fit is the value of the correlation coefficient (CC) between the two variables which equals -0.9947. CCs measure the strength of the relationship between two fitted values. The closer to 1 (or -1) this is, the more strongly the fitted values are linked. This means that small changes in the fit of one value has a significant effect on the other. It is clear that the equations used to fit this data produce highly correlated fitted values, even with good quality data spanning a whole relaxation curve.

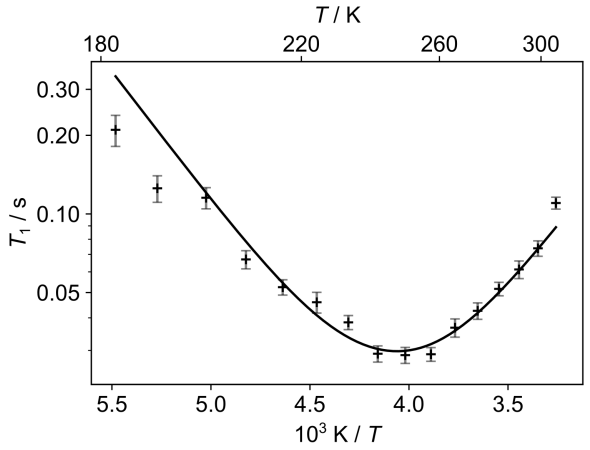

Figure 6.13: ^{2}H spin-lattice relaxation time constants as a function of temperature of FSPA ethanol-d_2 acquired at 61.42 MHz and 10 kHz MAS. Measured using a saturation recovery sequence using a saturation train of 64 pulses. Each temperature had 16 increments with 64 transients and a maximum recovery time ranging from 0.26 – 0.85 s. The curve is a fit of the experimental data to $E_a = 19.0(9)\,\mathrm{kJ\,mol^{-1}}$ and $\log_{10}(\tau_0 \,/\, \mathrm{s}) = -12.82(19)$ *assuming an Arrhenius-type fitting.*

6.4.2.2 Relaxation Analysis

Figures 6.10 and 6.13 show fitted ^{13}C and ^{2}H relaxation data from the CH_2 / CD_2 site on FSPA ethanol / FSPA ethanol-d_2. The data of each nucleus is of significantly different quality: the deuterium data has more measurements, it spans the whole relaxation curve, and the uncertainty on each measurement is lower. Typically, the ^{13}C relaxation data would be discarded in favour of much more reliable ^{2}H relaxation data, however the study below seeks to find out if the data is compatible within the experimental uncertainty.

Standard Fitting: E_a and $\log_{10}(\tau_0)$

A fitting program requires an estimated noise level to calculate the uncertainties on the fitted parameters. There are two options for the noise level: 'experimental' uses explicit experimental uncertainties and 'residual' estimates a noise level based on the residuals of the fit. For the ^{2}H data, where uncertainty on individual data points is low but there are systematic uncertainties meaning some data points do not sit on the fitted relaxation curve, it is sensible to use a noise level based on the residuals of the fit. For the ^{13}C data, the reverse is seen: the uncertainty on each value is large but the points align well on the fitted curve as there are only six data points. In this case using the noise level based on residuals of the fitting would underestimate the uncertainties so explicit experimental uncertainties have been used. The fitted parameters and their uncertainties based on an E_a / $\log_{10}(\tau_0)$ least squares fitting and the noise levels documented are given in Table 6.1.

There is significant disagreement between the fitted values of the carbon and deuterium relaxation measurements; both the E_a and $\log_{10}(\tau_0)$ values are well outside of the calculated uncertainty. Using Equation 6.1 and Equation 6.2, the rate of motion can be

Table 6.1: Fitted parameters based on the E_a / $\log_{10}(\tau_0)$ fitting. $\log_{10}(A$ / Hz$^2)$ was not correlated to either of the other fitted variables and so not considered further.

	Noise level	E_a / kJ mol^{-1}	$\log_{10}(\tau_0$ / s)	$\log_{10}(A$ / Hz$^2)$	CC between E_a and $\log_{10}(\tau_0)$
^{2}H	Residuals	19.0(9)	−12.82(19)	9.657(14)	−0.9947
^{13}C	Experimental	36(4)	−16.5(7)	8.82(4)	−0.9968

calculated over a range of temperatures. This leads to the key question: are the predicted rates from the relaxation measurements of the two nuclei compatible within the uncertainty? To answer this question, the uncertainty on the rate of motion must be calculated.

$$\tau_c = \tau_0 \exp \frac{E_a}{RT} \tag{6.1}$$

$$\nu = \frac{1}{2\pi\tau_c} \tag{6.2}$$

In the absence of strong correlations, the uncertainty on the rate would be easily calculated by propagating the uncertainties from the fitted parameters (given in Equation C.2 in Appendix C). However, the CC from this fitting is very close to −1, showing that there is a high dependency between the fitted parameters. The traditional error propagation formulae are only valid for independent, uncorrelated variables. The following sections seeks an alternative method of calculating the true uncertainty on the rate from each nucleus.

Monte Carlo Simulations

The most general method of estimating uncertainties is the MC approach. It simulates real data by adding random noise, at a specified level, to estimate uncertainties on fitted parameters after thousands of simulations. The results of each fitting can be binned and plotted in a histogram. Figure 6.14 shows the MC simulations of E_a and $\log_{10}(\tau_0)$ for the ^{2}H and ^{13}C data.

Table 6.2 shows that the uncertainties on each fitted parameter from the least squares fitting and the MC simulations are identical to two significant figures, as expected. When these fitted parameters are plotted as 2D histograms they become a pictorial representation of the CC between the parameters, as shown in Figure 6.15. For this parameterisation, MC simulations lie on a line confirming the strong correlation. Rates of motion can be calculated from individual MC simulations and the standard deviation of outputted values gives the uncertainty on each rate without the need for error propagation. This is the reason for running a MC simulation: even though the fitted parameters and their uncertainties are identical to a least squares fit, only a MC simulation can account

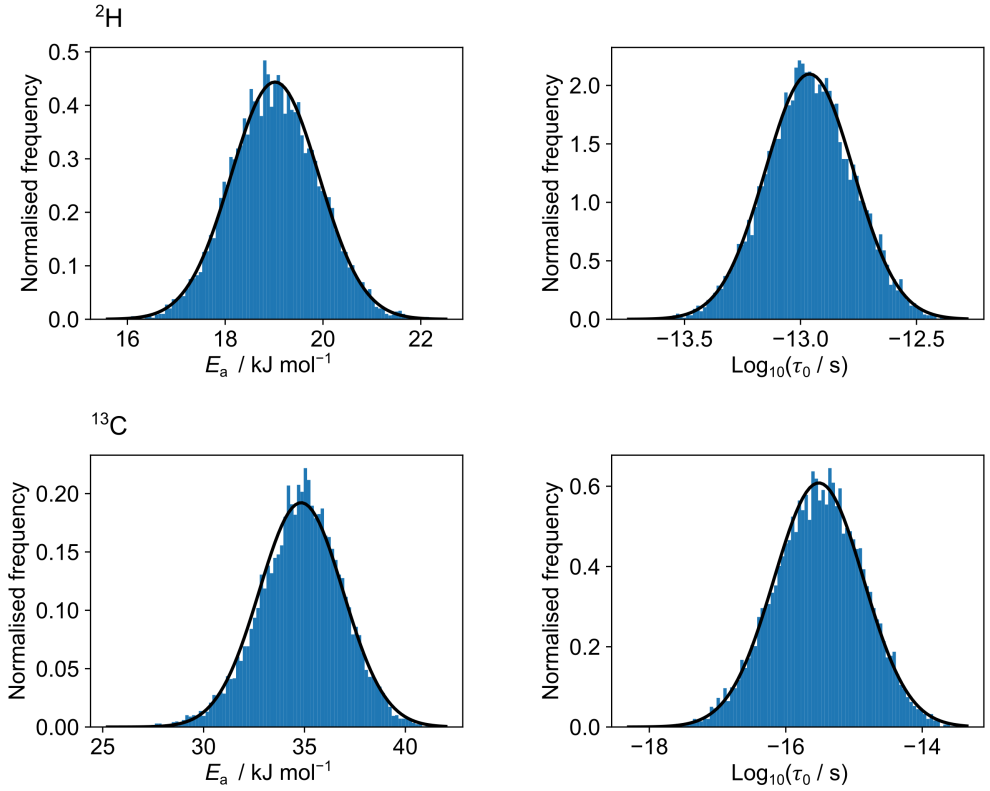

Figure 6.14: MC simulations of E_a and $\log_{10}(\tau_0)$ for ^{2}H and ^{13}C relaxation data based on 10,000 simulations.

for the correlation between fitted parameters.

Table 6.2: Comparison of uncertainties on fitted parameters from least squares fit documented in Table 6.1 and the MC simulations shown in Figure 6.14

			Uncertainties calculated by:	
Nucleus	**Noise level**	**Fitted parameter**	**Least squares fitting**	**Monte Carlo simulations**
^{2}H	Residuals	E_a / kJ mol^{-1}	0.90	0.90
		$\log_{10}(\tau_0$ / s)	0.19	0.19
^{13}C	Experimental	E_a / kJ mol^{-1}	4.0	4.0
		$\log_{10}(\tau_0$ / s)	0.73	0.73

The overlaid graph on Figure 6.15 shows that the ^{2}H and ^{13}C values do not overlap. They do lie on a similar line perhaps indicating that they are being affected by the same motion in different ways.

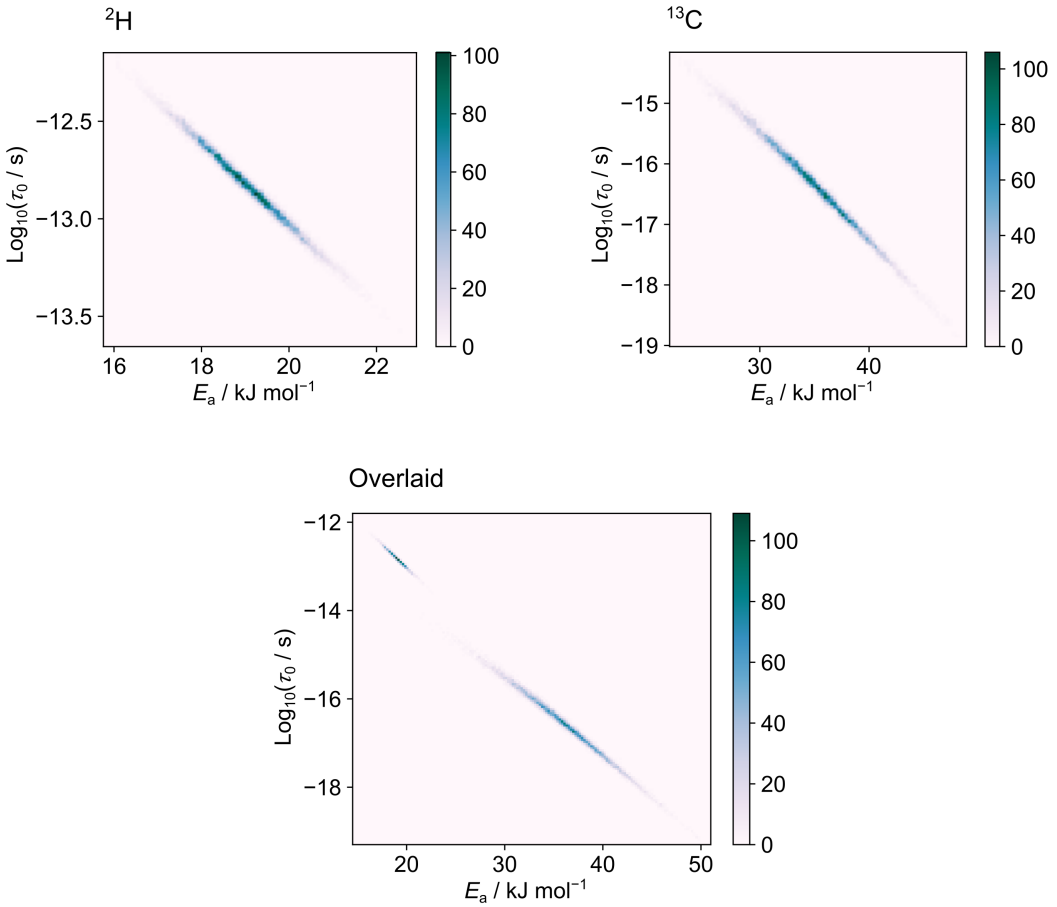

Figure 6.15: Correlation between the E_a and $\log_{10}(\tau_0)$ from MC simulations based on 10,000 repetitions for ^{2}H and ^{13}C. The vertical probability density scale is arbitrary.

Unlike the uncertainties from error propagation (Figure 6.19 on page 103), uncertainties from MC analysis do not vary linearly with inverse temperature, as shown in Figure 6.16. The deuterium pattern is consistent with Smith et al.[107] who reported that rates of motion could be predicted most precisely at the relaxation minimum. However, the uncertainties on the ^{13}C data are not at a minimum around the relaxation minimum, but instead have the smallest uncertainties around the centre of the fitting range.

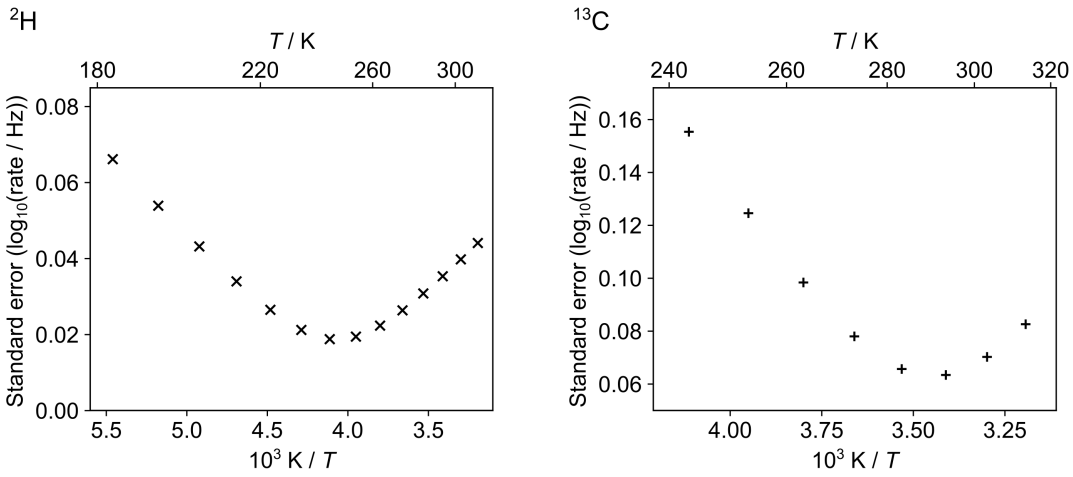

Figure 6.16: Uncertainties on $\log_{10}$(rate / Hz) as a function of inverse temperature for ^{2}H and ^{13}C relaxation data from MC analysis.

Figure 6.17 shows that the uncertainties from MC simulations are much smaller than uncertainties from those calculated incorrectly by propagating the errors. This demonstrates that error propagation is not appropriate for correlated variables and will significantly overestimate uncertainties, hence the only method of calculating uncertainties with this fitting is through MC simulations. This would have an impact on the conclusions drawn from the data: what would have originally been interpreted as overlapping uncertainties (shown by the shading), is now clear that the values are no longer equivalent within the uncertainty (shown by the error bars).

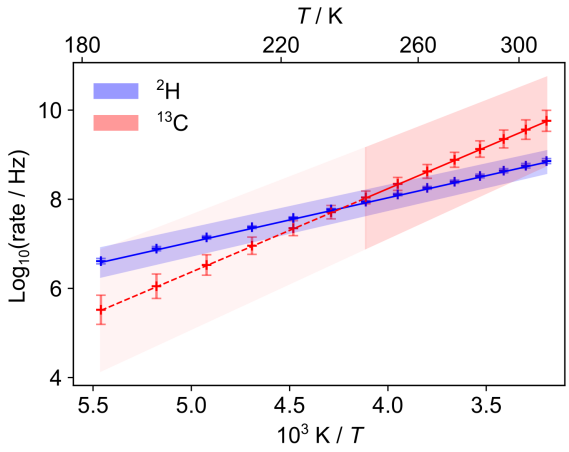

Figure 6.17: Rates of motion based on E_a / $\log_{10}(\tau_0)$ parameterisation with the shaded area representing the incorrect uncertainties calculated from error propagation and error bars representing the uncertainties calculated from MC simulations. Dashed line shows extrapolated fitting beyond the temperature range measured.

New Fitting: E_a and T_{min}

As discussed above, the traditional fitting of relaxation data in terms of an E_a and $\log_{10}(\tau_0)$ is problematic due to significant correlation between fitted parameters. Here, the fitting is reparametrised to E_a and T_{min}, which uses the Larmor frequency as a reference point* as shown in Equation 6.3. Since the activation energy is determined by the gradient of the curve and T_{min} is determined by the location of the curve in the horizontal axis, the correlation between the two parameters should be much smaller. Additionally, T_{min} is physically meaningful and can be estimated from the temperature of the minimum of the curve. In contrast, τ_0 is not physically meaningful which can make choosing a starting value for the fit more difficult, especially since parameters are highly correlated.

$$\nu_0 = \frac{1}{2\pi\tau_c(T_{min})} \tag{6.3}$$

The fitted E_a / T_{min} parameters are shown in Table 6.3. They are directly comparable with the fitted E_a / $\log_{10}(\tau_0)$ parameters given in Table 6.1. The most notable change is the reduction of the CC to more reasonable values. The correlation between E_a and T_{min} remains high for the ^{13}C data because the data points are only on one side of the curve making fitting to multiple parameters difficult. Despite the reduction in the CC, there are virtually no changes to the uncertainties of the activation energies, because they are determined by the uncertainty in the gradient of the slopes and not affected by correlation to another parameter.

Table 6.3: Parameters based on E_a / T_{min} fitting.

	Noise level	E_a / kJ mol^{-1}	T_{min} / K	$\log_{10}(A$ / Hz$^2)$	CC between E_a and T_{min}
^{2}H	Residuals	19.0(9)	234.0(1.2)	9.657(14)	0.49
^{13}C	Experimental	36(4)	245(5)	8.83(4)	0.92

From the E_a / T_{min} fitted parameters, rates of motion were calculated using Equation 6.4 which has been derived from Equation 6.3 and Equation 6.1. The new rates were identical to the original parameterisation (within 0.01 %). With a much lower CC, traditional error propagation is more meaningful and were calculated using Equation C.5 from Appendix C.

$$\tau_c = \frac{1}{2\pi\nu_0}\exp\left(\frac{E_a}{R}\left(\frac{1}{T} - \frac{1}{T_{min}}\right)\right) \tag{6.4}$$

The purpose of the reparameterisation is that valid uncertainties on the rates can be calculated without the need for a MC simulation. However for a complete picture, MC

*Although the temperature values will be close, it is important to note that T_{min} is the temperature that corresponds to the Larmor frequency, not the temperature at the minimum of the curve. The minimum of the curve is determined by linear combination of spectral densities as shown in Equations 2.6 and 2.7 on page 13.

analysis of the E_a / T_{min} fitting are shown in Figure 6.18 which demonstrates graphically the difference between reasonable uncorrelated parameters (^{2}H) and correlated parameters (^{13}C). Rates of motion calculated from these MC simulations were almost identical to the MC analysis of the E_a / $\log_{10}(\tau_0)$ fit given in Figure 6.15.

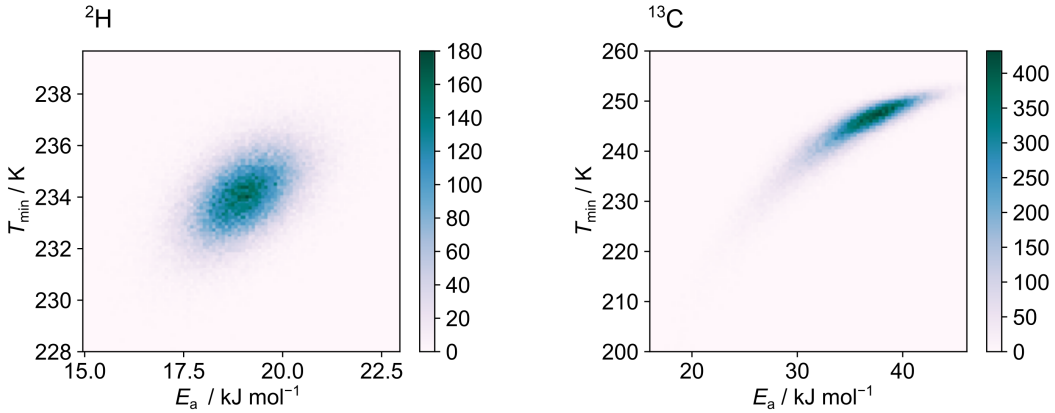

Figure 6.18: MC simulations of the E_a / T_{min} fit based on 100,000 repetitions. The vertical probability density scale is arbitrary.

As would be expected, the uncertainties derived from MC fitting are independent of the parameters used, as shown in Figure 6.19. They were also almost identical in pattern and magnitude demonstrating that MC analyses produce the same results regardless of how correlated the starting parameters are. Figure 6.19 also shows that the value of the uncertainties from the MC analysis and the propagation of errors on an E_a / T_{min} fit are very similar, in magnitude and trend. There is more deviation between the uncertainties on the ^{13}C data due to the remaining correlation on the E_a / T_{min} parameters. This shows that the T_{min} parameterisation has given a much more accurate uncertainty on rates of motion without the need for a MC simulation.

To summarise, fitting to E_a and T_{min} reduces the correlation between parameters compared to fitting to E_a and $\log_{10}(\tau_0)$, particularly with good quality data spanning the whole relaxation curve. This means that error propagation is a meaningful way of determining the uncertainties on rates, forgoing the need for MC analysis. After a search of the literature, and to the best of our knowledge, this parameterisation has not been described before.

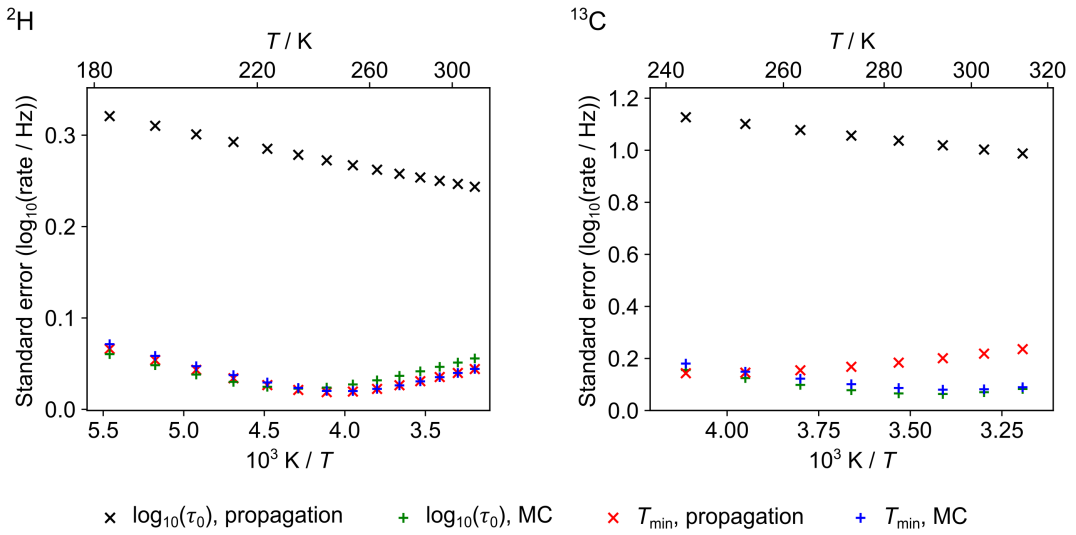

Figure 6.19: Comparison of the uncertainties in the rates calculated by error propagation and MC simulations of E_a / $\log_{10}(\tau_0)$ and E_a / T_{min} fits. Uncertainty parameterisation using the T_{min} parameterisation (red markers) gives results that closely match a robust uncertainty analysis using MC simulation (green and blue markers). Naive uncertainty propagation based on $\log_{10}(\tau_0)$ (black markers) gives significantly incorrect results for both low and high quality data. Note that the two MC analyses are near identical, as expected, and the T_{min} propagation values are much closer to the MC values than the $\log_{10}(\tau_0)$ values, particularly for the high quality data.

Fitting Both Datasets to One Activation Energy

The datasets have also been fitted to a common activation energy. This is regularly done in the literature, particularly when there are high numbers of low quality datasets, to improve the accuracy of results.[108] The dual fitted data shown in Figure 6.20 uses experimental uncertainties so that the fitting program can weight the relative importance of data points depending on the certainty of the measurement. The data fitted to $E_a = 18.0(4)\,\mathrm{kJ\,mol^{-1}}$ and the T_{min} values are recorded in Table 6.4. The rates of motion, and uncertainties calculated from error propagation, are shown in Figure 6.21.

Table 6.4: T_{min} values and CC between E_a and T_{min} values for each dataset based on a common E_a fitted to $E_a = 18.0(4)\,\mathrm{kJ\,mol^{-1}}$.

	T_{min} / K	$\log_{10}(A$ / Hz$^2)$	CC between E_a and T_{min}
^{2}H	230.6(3)	9.653(13)	0.29
^{13}C	203(8)	9.07(15)	0.32

Figure 6.20 and Figure 6.21 show that the fit has effectively optimised for the deuterium data, with a clearly poor fitting for the ^{13}C data. This is due to the difference in quality between the datasets. Fitting two sets of relaxation data in this instance has not produced more reliable rates because the quality of the datasets are vastly different.

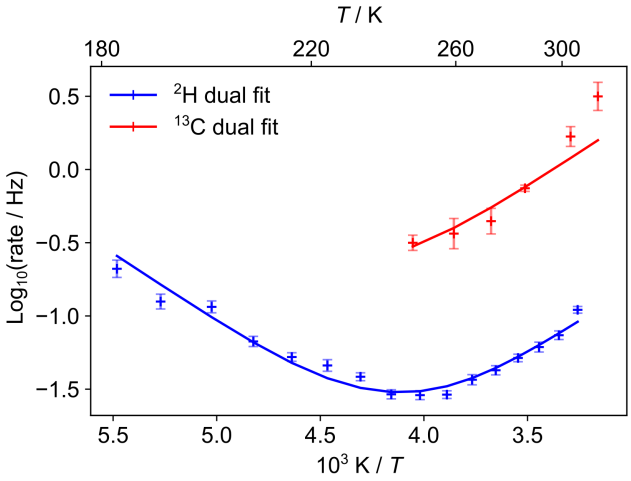

Figure 6.20: Both datasets fitted to a single activation energy.

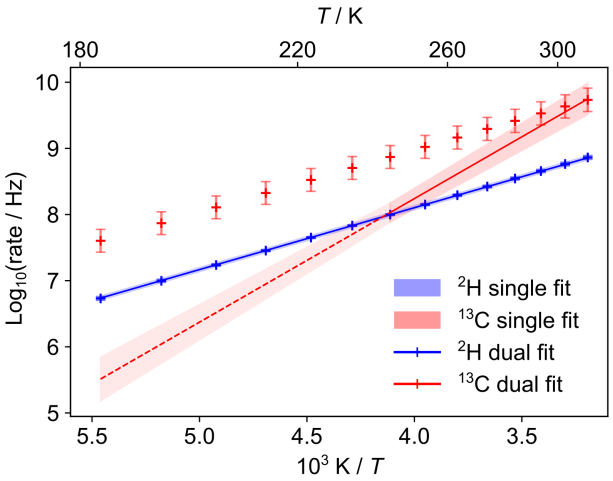

Figure 6.21: Rates of motion based on E_a / T_{min} fitting to a single E_a (error bars) and a single fit (shaded area) using explicit experimental uncertainties.

Reparameterisation Conclusion

In conclusion, fitting to an E_a and a $\log_{10}(\tau_0)$ gives high CCs even when fitting to high-quality data. This is not a significant problem if there is no interest in the uncertainties on the rates. However, for information regarding the uncertainties on the calculated rates, MC analysis is required to give a more accurate picture. These MC simulations are straight forward to run, but take time if many simulations are used.

Alternatively, reparameterising gives a much more robust analysis of uncertainties without the need for MC simulations. The CC will be closer to 0 when fitting to an E_a and a T_{min} if the data are of good quality. If this is the case, then uncertainties calculated from error propagation and from MC simulation will be very similar. Fitting multiple relaxation measurements to one activation energy may be the best way forward for datasets that are similar, in terms of number of measurements taken and the associated uncertainty on each

point, but do not work for cases where the quality is significantly different.

After analysis of the data, it is clear that the ^{2}H and ^{13}C relaxation do not give rates of motion that are compatible within the uncertainty in this case. This could be because the carbon data are poor quality and can not be analysed effectively. However there are many plausible reasons that ^{2}H and ^{13}C relaxation data may not give the same result. It is unlikely that each nuclide is probing a different motion since the Larmor frequency is only a factor of two apart. However it is plausible that each nuclide is affected differently by the same motion. Deuterium relaxation depends on the quadrupolar coupling tensor which, to a first approximation, is directed along the C–D bond hence the relaxation on each spin is independent. Conversely, ^{13}C relaxation is dependent on the dipolar tensors that depend on the orientation of the two C–H bonds. For non-isotropic motion, the correlated motion of the two C–H bonds makes relaxation theory complex.

Alternatively, it could be due to the motional model used to fit the data. Each relaxation model uses different linear combinations of spectral densities. In this case, the data has been fitted to isotropic motion, which is unlikely to be reality but does provide an unbiased starting point. In summary, the rates of motion are not known as precisely as the small uncertainties would suggest without a good initial model of the motion. Given that the ^{2}H and ^{13}C relaxation are fitted to different equations, it is possible that having an incorrect model would affect the fitting differently in each case.

Additionally, there may be problems regarding the physical interpretation of relaxation rates. Relaxation analysis is only meaningful for molecules undergoing one simple motional process with a well-defined correlation time. However any motion(s), simple or otherwise, can produce a v-shaped curve as a function of inverse temperature. Relaxation minima are effectively an interference effect and so the same shape could be seen if the motion were complex, with a distribution of correlation times. If this is the case, fitted parameters and rates would have no meaning.

6.4.2.3 Fitting Deuterium Lineshapes

There are numerous pieces of data giving clues to the motion of the ethanol molecules in FSPA ethanol-d_2. ^{2}H T_1 relaxation measurements indicate the presence of a fast motion with selected rates given in Table 6.5. There is also evidence of a motion on the order of 10s of kHz between 185 – 220 K from broadening of ^{13}C resonances shown in Figure 6.9 on page 93. The following section seeks to understand what can be learnt from the ^{2}H lineshapes given in Figure 6.12 on page 95.

The spectra did not fit well using SOLA on TopSpin because the spectra are not the result of a single simple motion. The following simulations were made with Weblab[19] (parameters are given in Table D.1 in Appendix D):

Simulation 1: One variable, intermediate motion about a C_2 axis with a cone angle of 59 °. (Green spectra in Table D.2 in Appendix D.)

Table 6.5: Rates of motion from simplistic modelling of isotropic motion of the ethanol molecule in FSPA ethanol-d_2 solvate calculated from fitted ^{2}H T_1 relaxation data *based on simple isotropic motion and assuming a barrier-type motion.*

Temperature / K	**Rate / MHz**
300	591.1(4)
235	64.0(2)
185	4.7(6)

This is the simplest model and simulates a C_2 jump of the whole ethanol molecule about an axis that bisects the D–C–D bond angle of 118 °. The simulation was run at 10^3, 10^4, 10^5, 10^6 and 10^7 Hz: spectra are shown in Table D.2 in Appendix D (green lines). These did not fit well with the experimental spectra so it was assumed that there must be two motions influencing the deuterium linewidths, which is consistent with the other experimental data.

The following simulations were designed to describe two motions: One variable, intermediate C_2 jump on a 59 ° cone angle, and a fast, wobble-type motion.

Simulation 2: One variable, intermediate motion about a C_2 axis with a cone angle of 59 ° and a fast 2-site jump at variable angles. (Blue spectra in Table D.2 in Appendix D.)

Simulation 3: One variable, intermediate motion about a C_2 axis with a cone angle of 59 ° and a fast 3-site jump at variable angles. (Cyan spectra in Table D.2 in Appendix D.)

Simulation 4: One variable, intermediate motion about a C_2 axis with a cone angle of 59 ° and a random wobble that has the effect of increasing the starting η value. (All spectra in Table D.3 in Appendix D.)

Single fast-jump spectra at variable angles (2-site (magenta) and 3-site (red) spectra both in Table D.2 in Appendix D) are also given as comparisons.

Overall, despite the large number of simulations, there were few simulations similar to the experimental lineshapes. The closest simulation to each experimental lineshapes are shown in Figure 6.22. These are based on a 2-site fast wobble motion and a starting C_Q equal to 160 kHz.

The 185 K predicted spectrum is satisfactory. The overall width is similar, as shown by the outer horns, and the inner peaks also match. Initially, it was hoped that a model could be found where the wobble angle remained constant and only the speed changed with temperature, however it is possible that the wobble angle also varies with temperature. The higher temperature spectra fit less well, likely because the motion is more complex than simulated here.

These fits give an indication of the possible types of motion present. It is plausible to infer that the ethanol molecule is wobbling at an angle of 25 – 35 ° at a fast rate on

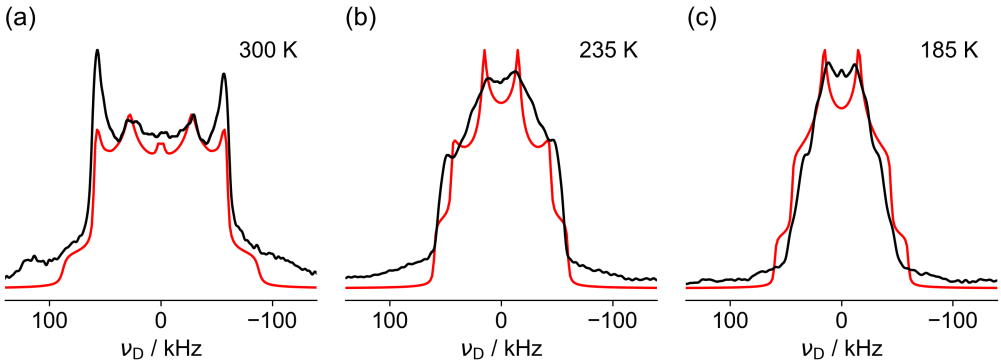

Figure 6.22: Experimental ^{2}H lineshapes of FSPA ethanol (shown in black) at (a) 300 K (b) 235 K and (c) 185 K. Simulated ^{2}H lineshapes (shown in red) of a C_2 jump on a cone of angle of 59 ° at rates (a) 10^4 Hz, (b) 10^6 Hz and (c) 10^7 Hz and a fast, 2-site wobble angle (a) 25 °, (b) 35 ° and (c) 35 °.

top of an intermediate speed, C_2 jump. However, the fits are far from perfect fits and so care must be taken when drawing conclusions. Significant numbers of spectra have been simulated each from a plausible model and so it is perhaps not unlikely that some will match the experimental data.

This lineshape data has not provided conclusive evidence for a particular motional model or information on rates. The best guess has been discussed above, however it may be the case that when a complex motion is present, lineshapes can be used to validate the motional models produced by MD, rather than predict motions themselves.

6.5 NMR Experimental Summary

NMR experiments are sensitive to molecular motions over many order of magnitudes. This can be both extremely useful in some cases but lead to difficulties and apparent contradictions.

For FSPA acetone, fitted ^{2}H spectra suggested a C_2 jump motion around 500 Hz at 235 K and fitting ^{2}H T_1 relaxation times gave an apparent $E_a = 7.9(2)$ kJ mol^{-1}. However, it would be surprising if a C_2 jump motion on an intermediate timescale had such a low activation energy.

For FSPA ethanol, there was more experimental data to work with and this is summarised in Figure 6.23. ^{2}H relaxation revealed a fast motion across the temperature range measured (190 – 300 K) however slower motion was also affecting the ^{2}H lineshapes. Despite extensive fitting using Weblab, no simple picture of the dynamics could be found which explained both the relaxation and lineshape data. There are reasons why this may be the case. Relaxation and lineshape analysis provide different angles for probing molecular motion in the solid state. Not only are the two motions probing different rates of motion, but they are also sensitive to different types of motion. While deuterium lineshapes are sensitive to larger amplitude motions, relaxation rates are sensitive to all motion, even

small libration-type motions. Both techniques provide valuable information on motions with different timescales, but care must be used when interpreting outputted rates. Both analyses work well with additional measurements, both from NMR and other techniques, and can benefit from a plausible model of the motion.

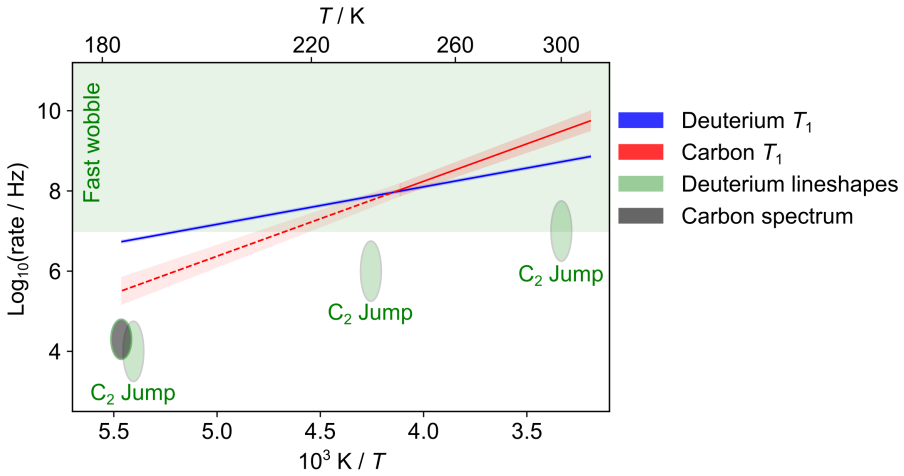

Figure 6.23: Summary of the ethanol motions *based on NMR data in isolation.*

6.6 Molecular Dynamics

The molecular dynamics simulations discussed in this section were run by Will Glossop, Songül Guryel, Valentina Erastova and Mark Wilson (Durham University) who collectively focused on the Markov State Modelling approach to analysis. Vasily Oganesyan (University of East Anglia) developed new methodology to directly predict NMR spectra and relaxation parameters from MD trajectories. This is summarised below and described in detail in the manuscript in preparation: 'Understanding guest dynamics in crystalline molecular organics'.

MD is a useful tool for studying dynamics in solids and can be utilised alongside NMR and XRD for a full understanding of dynamic disorder. A variety of systems have been studied with MD, commonly biomolecules and soft matter. However, there are very few studies for characterising motion using MD in a fixed cavity. A few examples combining MD and NMR in similar systems include modelling dynamics in urea inclusion compounds,[109] solvates of DMSO,[110] and in hydrates.[111]

The MD simulations were set up MD using a $9 \times 3 \times 3$ supercell of the unit cell obtained from XRD experiments at 120 K. The solvent molecules were too disordered to be located in the diffraction study so they were placed in the void and allowed to move freely during an equilibration period. After the initial setup was complete, the system was heated from 120 K to 350 K and from this, structures were extracted at five discrete temperatures:

150 K, 200 K, 250 K, 300 K and 350 K. At each temperature, final production simulation runs were performed for up to 400 ns and analysed separately.

The simulation runs at each temperature were analysed using two methods. One method, known as Markov State Modelling, involves 'clustering' the simulation results into discrete states. This technique was developed for analysing large amplitude motions of complex biomolecules and has the advantage of picking out the 'slower' motions but may overlook faster libration-type motions as these are treated as 'noise' on the jumps between distinct 'macrostates' of the system. The other method uses the simulation runs to directly predict NMR parameters (and hence predict relaxation times and spectra). This is useful since the experimental data can act as external, real-world validation of an otherwise purely theoretical model.

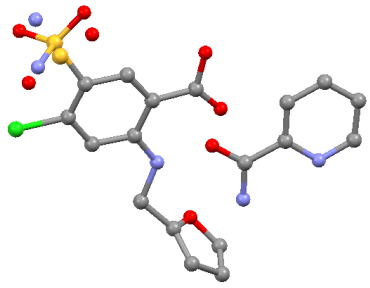

(a) Asymmetric unit

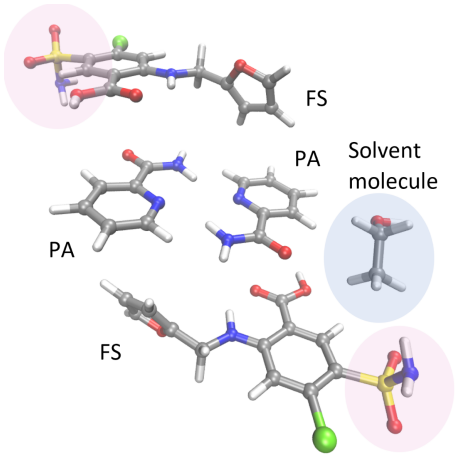

(b) Model A

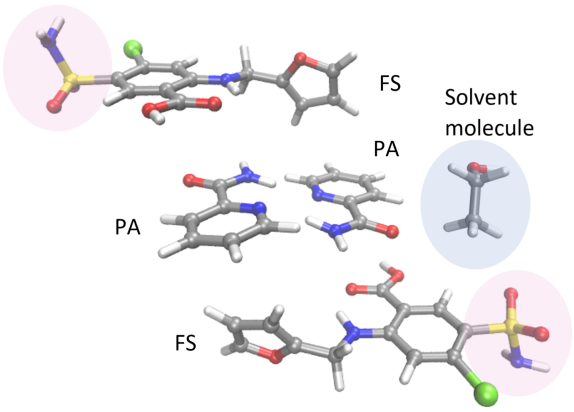

(c) Model B

Figure 6.24: (a) asymmetric unit of the FSPA solvates with disorder of the sulfonamide group is shown with split-atom sites (solvent molecule not shown). (b) and (c) illustrations of the unit cell of the FSPA cocrystal solvates derived from SCXRD experiments at 120 K. Disorder of the sulfonamide group (highlighted in pink) was modelled with a 50:50 split site model, which was resolved into two structure models, A and B, containing uniquely one position or the other.

SCXRD revealed additional disorder of the sulfonamide group on the FS molecule, as shown in Figure 6.24a which was modeled over two equal positions from the diffraction data. Modelling this disorder with an MD simulation was challenging since the dynamics

were much slower than the solvent dynamics so would have required much longer simulation runs. Instead, the sulfonamide disorder was addressed in the MD simulations by creating two MD trajectories, one with the NH_2 of the sulfonamide pointing towards the solvent channel (model A) and one away from it (model B). This is shown in the pink shading in Figure 6.24b and c. Naturally, the physical system will contain a random distribution of sulfonamide orientations but most simulations showed little movement of the sulfonamide.

Figure 6.25 shows the comparisons between experimental ^{2}H NMR spectra and the spectra predicted from MD trajectories. Considering the complexity of the system, the agreement between predicted ^{2}H NMR spectra is excellent. This experimental validation of MD simulations can give confidence that the simulations have accurately captured the solvent dynamics behaviour, and that the methodology used is appropriate to the system.

It should be noted that the overall predicted spectrum of the ethanol solvate at 200 K is a combination of the MD prediction and the 'frozen limit' lineshape. Similar unexpected contributions from 'frozen' guest molecules have been observed in similar studies,[112] and explained in terms of temperature gradients across the sample in the probe. This seems unlikely in this case since the ^{2}H lineshape predictions from MD are still not fully static at 150 K. This experimental behaviour was reproducible, and is perhaps the result of an interaction between the solvent and sulfonamide disorder, which results in a frozen glassy state which is difficult to reproduce in simulation.

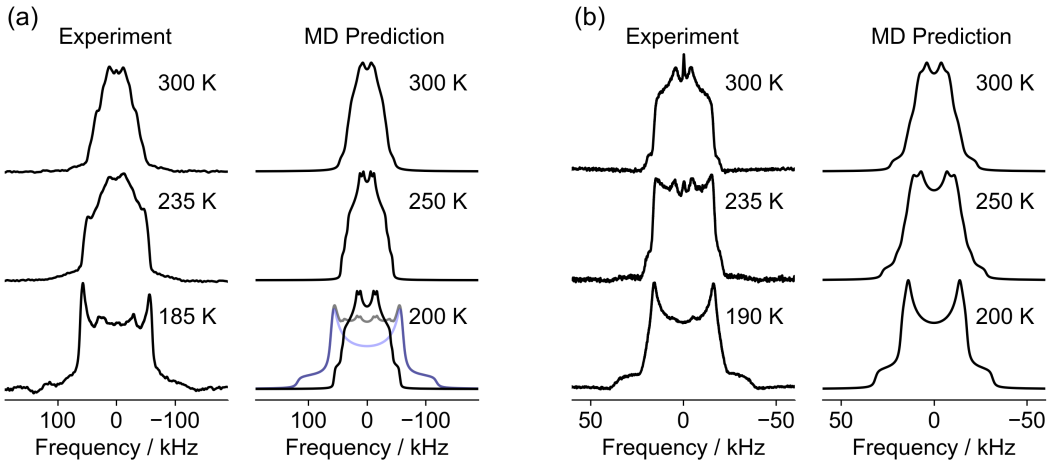

(a) FSPA ethanol-d_2

(b) FSPA acetone-d_6

Figure 6.25: For (a) FSPA ethanol-d_2 at 76.71 MHz and (b) FSPA acetone-d_6 at 61.42 MHz, comparisons between experimental ^{2}H NMR spectra (left) and those predicted from MD trajectories (summed over models A and B) for the closest matching temperatures (right). Note, FSPA ethanol-d_2 experimental spectrum at 185 K contains a significant contribution from the 'frozen limit' lineshape. The 'overall predicted lineshape' in this case (grey) is the sum of 20 % dynamic component predicted directly from MD trajectories (black) and 80 % static component (blue).

The motion from the MD trajectories do not fit into a simple motional model such as free rotational diffusion about an axis or C_2 jumps. Instead, the motion can be characterised as a combination of a varying wide-angle librational motion plus a flip-type motion. These dynamics are summarised in terms of a correlation time, τ_c, and a generalised order parameter, S^2, of the molecular orientations. These are derived from single-exponential representation of the autocorrelation functions, $C(t)$, where $S^2 = C(\infty)$ and the effective correlation time is calculated by time-integration of the correlation function using Equation 6.5. Autocorrelation functions can be found in the SI of the manuscript in preparation and an example is given in Figure 6.26 for context. Even though this parameterisation does simplify the solvent dynamics, it is expected to be sufficient to understand the system.

$$\tau_c = \frac{\int_0^\infty C(t) - C(\infty)\, dt}{1 - C(\infty)} \tag{6.5}$$

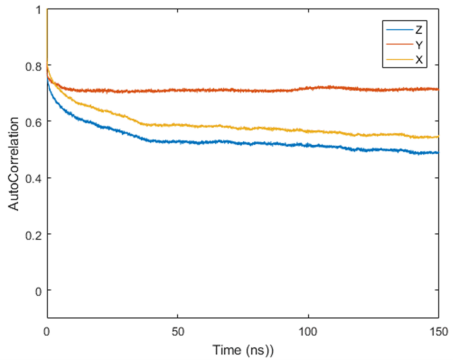

Figure 6.26: Autocorrelation functions of molecular axes X, Y and Z of FSPA acetone (model A) at 250 K. Figure supplied by Vasily Oganesyan.

The correlation times and order parameters are given in the mid and lower panels of Figure 6.27 respectively. In both cases, but in particular the acetone, these values show why the NMR data was difficult to interpret alone. The order parameter, which relates to the geometry or amplitude of the motion varies with temperature. This demonstrates why a simple jump-type model, which assumes a fixed amplitude of motion, will not correctly describe the dynamics, even if plausible fits to the experimental data can be obtained (shown in Figure 6.7 on page 92). Additionally, when fitting relaxation data, there are inherent assumptions made, such as the relaxation times are being affected by a barrier-type motion, which has a constant activation energy and hence can be fitted to an Arrhenius-type equation. However, the τ_c values are essentially independent of temperature over the range 200 – 300 K for FSPA acetone-d_6 (see mid panel of Figure 6.27b). Instead of the rate increasing with temperature, it is the extent of motion (parameterised by S^2) that changes with temperature. This implies that the acetone dynamics has a strong librational character. Libration-type motions are more like simple harmonic oscillators. These do not have an energy barrier hence the correlation time will not increase with temperature, as would be expected for a motion with an energy barrier, and instead the

amplitude increases. In contrast, FSPA ethanol-d_2 does show evidence of the presence of a barrier-type motion. From 200 – 350 K τ_c varies approximately linearly with temperature and the order parameter, S^2, is approximately constant.

The comparison of predicted T_1 relaxation times to experimental values, shown in the upper panels of Figure 6.27, gives further weight to the interpretation of the dynamics from the MD analysis. There is good qualitative agreement of relaxation when considering the systems as a pair.

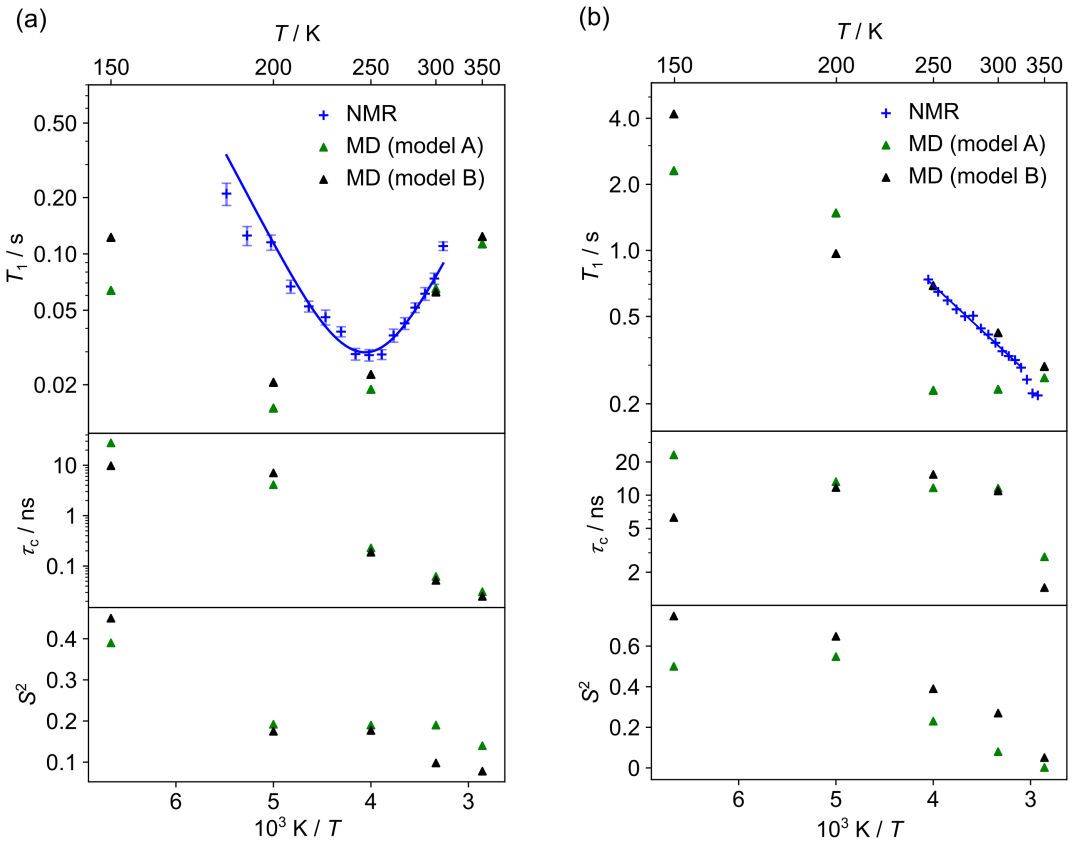

(a) FSPA ethanol-d_2

(b) FSPA acetone-d_6

Figure 6.27: Upper panels: ^{2}H spin-lattice relaxation time constants as a function of temperature of (a) FSPA ethanol-d_2 acquired at 61.42 MHz and (b) FSPA acetone-d_6 at 76.71 MHz. Triangles correspond to the predictions from MD simulation. Mid panels: rotational correlation times from MD simulations. Lower panels: generalised order parameters from MD simulations. The relaxation curve in (a) is a fit of the experimental data to E_a of 19.0(9) kJ mol^{-1} and a $T_{min} = 234.0(12)$ K. Although the experimental data in (b) looks to fit to a straight line, the correlation times obtained from MD show that the temperature dependence should not be interpreted in terms of an E_a.

For the acetone solvate, the Markov State Modelling approach to MD analysis allows for representative snapshots of the acetone molecule to be obtained. These four orientations of the acetone within the cavity, shown in Figure 6.28, are related by a C_2 axis (respecting the molecular symmetry) and an inversion centre (respecting the symmetry of the cavity). This is an additional piece of useful information which cannot be learnt

from NMR data since the ^{2}H quadrupolar tensor is unchanged under inversion and so any inversion-type dynamics will be invisible to ^{2}H NMR.

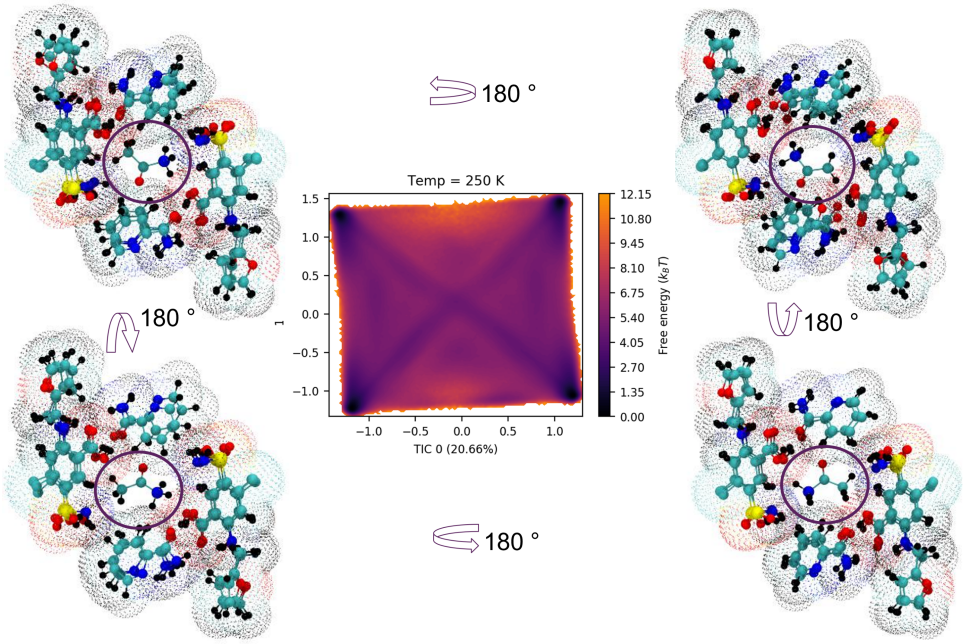

Figure 6.28: Free energy plot from Markov State Modelling of FSPA acetone with representative snapshots of macrostates corresponding to the four free energy minima. One of the methyl carbons of the acetone is coloured dark blue to highlight the reorientation.

Molecules do, however, spend significant time between macrostates, likely librating, which the Markov State Model is unable to observe as the technique is designed to filter out the faster motions. It is for this reason that this approach was not as effective for the ethanol solvate as the ethanol molecule did not have well defined low-energy states.

For the ethanol solvate, the Markov State Modelling approach to MD analysis is less successful at resolving 'macrostates' as shown in Figure 6.29. The motion is likely to be a complex mix of libration and wide-angled motions.

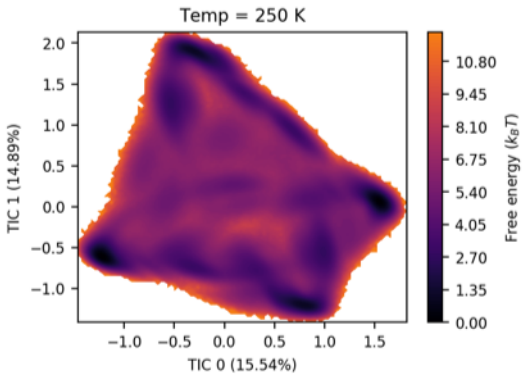

Figure 6.29: Free energy plot from Markov State Modelling of FSPA ethanol showing a complex energy surface with no defined macrostates.

6.7 Conclusion

Deuterating guest molecules is a useful method for probing guest dynamics as they are straightforward and inexpensive to incorporate. ^{2}H NMR parameters and spectra are affected by dynamic processes on a broad range of timescales, and measurements can be localised to the guest molecule or even a specific part of the guest molecule which is a huge advantage over ^{1}H NMR. Deuterium measurements typically have a high signal-to-noise ratio in comparison to ^{13}C measurements and hence information is quicker to acquire.

The two types of experiments used here, ^{2}H lineshapes and ^{2}H T_1 relaxation, probe molecular dynamics in different ways. Relaxation times are sensitive to changes in both correlation time and the amplitude of motion and it can be challenging to determine the primary cause of changing relaxation times. Even when data fit convincingly to a straight line or a relaxation curve, caution should be taken before calculating activation energies or correlation times. Such calculations assume the motion is a barrier-type motion (such as C_2 jumps) which have a constant activation energy and constant amplitude of motion. However, for barrierless-type motions (such as librations) there are no energy barriers, much like a simple harmonic oscillator. In this instance, correlation times do not increase with temperature, instead the amplitude of motion increases and hence fitting relaxation times to an activation energy will not be physically meaningful.

^{2}H lineshapes have to be fitted to a model to be interpreted. However, even when a simple model fits the data well, as was the case for the FSPA acetone-d_6, these results can still be misleading. It can be very difficult to discern a motion from lineshapes if the motion is complex, as was the case for FSPA ethanol-d_2. In this case, the lineshapes work best as a tool to validate MD simulations.

For the two solvates presented here, a full understanding of the disorder could not be obtained by NMR. Instead, MD simulations were run and analysed using a Markov State Modelling approach to find four symmetry-equivalent 'macrostates' of the acetone molecule. Quantitative information was obtained through analysis of autocorrelation functions which found that there was significant librational character to the motion of both solvates. It also showed that there was little change in the correlation time with temperature, showing that simple Arrhenius-type analysis of T_1 relaxation data indeed lead to incorrect results. Using MD trajectories to predict NMR lineshapes and relaxation times allows the simulations to be validated and show that the MD has fully captured the dynamics observed in the NMR.

Disorder may be intrinsic to the stability of the phase, by providing entropic stabilisation and hence not necessarily a marker of instability as often assumed. Many pharmaceutical products are solvates in their final form and others use solvates during production. While many simpler systems can be analysed using NMR alone, it is anticipated that as systems increase in complexity, the need to couple NMR and MD to understand molecular dynamics is only going to increase. It is hoped that techniques used here will prove useful, not only in pharmaceuticals but any system with a trapped solvent molecule.

Chapter 7

Concluding Remarks

The aim of this work has been to show how solid-state NMR can be used to characterise disorder, specifically dynamic disorder, in different systems. This has been demonstrated in three distinct systems each requiring a bespoke combination of NMR-based and non-NMR-based techniques.

For the diamondoid systems, the motion of the rigid hydrocarbon cages could be extensively investigated with solid-state NMR alone. ^{1}H and ^{13}C relaxation provided activation energies and rate estimations as well as the geometry of motion for diamantane and 1(2)3 tetramantane. In triamantane, where ^{13}C relaxation could not provide the geometry of motion, second moments were shown to be a useful complementary tool.

For the MOF HMF, it was the combination of SCND and the multi-nuclei NMR (^{2}H, ^{1}H, ^{13}C and ^{15}N) which was needed to characterise the dynamics. While ^{1}H relaxation measurements gave motional parameters, it was the ^{2}H spectra which proved vital for understanding the separate populations of cations. A new mechanism has been suggested which proposes that the relaxor ferroelectric response is directly because of the molecular dynamics, not despite it.

The dynamics of the solvent molecules in two cocrystal solvates FSPA ethanol and FSPA acetone were studied with ^{2}H and ^{13}C NMR, however determining a motional model from the data proved challenging. In this case, it was the MD which proved most useful and it was found that the motion had significant librational character. This explained why the usual relaxation and lineshape analysis, which assumes a constant amplitude with temperature, was unable provide a coherent model.

Whilst studying relaxation in the systems above, a few general observations and conclusions about relaxation fitting have been made. Firstly, if two relaxation processes are observed in a set of data, it is important to fit the two simultaneously for accurate fitting parameters. This was shown in the ^{1}H $T_{1\rho}$ data of both diamantane and the MOF sample. Secondly, it was found that the usual fitting parameters, E_{a} and $\log_{10}(\tau_0)$, gave a high correlation coefficient. Consequently, determining an uncertainty on the calculated rate of motion is difficult as variables must be independent to propagate uncertainties. New fitting parameters, E_{a} and T_{min}, have been proposed which significantly reduce the

correlation coefficient resulting in a more robust analysis of uncertainties on the rate. An additional benefit of these new fitting parameters is that $T_{\min}$ can be estimated from the temperature of the minimum of the curve, unlike τ_0 which has no physical meaning. Hence choosing a starting value is easier for a $T_{\min}$ fit.

The results presented in this thesis have focused on systems with fast and intermediate motions. Slow dynamics are typically studied with exchange-type experiments since motion is often slow enough to resolve chemical shifts. Where resonances cannot be resolved, a Centreband Only Detection Of EXchange (CODEX) experiment is a 1D exchange-based experiment that uses a recoupling sequence to selectively reintroduce the CSA information lost during MAS.[113] There is significant scope for determining correlation times of molecular solids undergoing slow dynamic through the CODEX sequence.

Disorder in solids is common and there are an endless number of additional potential systems, with different types of motion, that could be analysed in the future. For solvent molecules in cavities, NMR and computational tools have been well developed in this project. In theory, this could allow the dynamics of any solvent molecules in any organic crystal to be studied using a combination of these techniques. This is important in the pharmaceutical industry where many formulations are hydrates and there are robust legislative reasons for fully characterising formulations. Future work will undoubtedly be compelling in the field of functional materials, where understanding the dynamics of the molecules is vital for understanding the behaviour of the bulk material. This could lead to discovering new mechanisms which in turn would help the development of new materials.

Bibliography

[1] D. C. Apperley, R. K. Harris, and P. Hodgkinson, *Solid-State NMR Basic Principles & Practice*, Momentum Press, 2012.

[2] M. Li, W. Xu, and Y. Su, *Trends Anal. Chem.*, 2021, **135**, 116152.

[3] Y. Yao and Q. Chen, *From Helical Jump to Chain Diffusion: Solid-State NMR Study of Chain Dynamics in Semi-Crystalline Polymers*, Elsevier Ltd., 2010.

[4] V. J. Witherspoon, J. Xu, and J. A. Reimer, *Chem. Rev.*, 2018, **118**(20), 10033–10048.

[5] E. Brunner and M. Rauche, *Chem. Sci.*, 2020, **11**(17), 4297–4304.

[6] A. B. Siemer, *Solid State Nucl. Magn. Reson.*, 2020, **106**, 101643.

[7] A. Krushelnitsky, D. Reichert, and K. Saalwächter, *Acc. Chem. Res.*, 2013, **46**(9), 2028–2036.

[8] J. M. Lamley and J. R. Lewandowski, *eMagRes*, 2016, **5**(3), 1423–1434.

[9] M. Hong, Y. Zhang, and F. Hu, *Annu. Rev. Phys. Chem.*, 2012, **63**(1), 1–24.

[10] P. Schanda and M. Ernst, *Prog. Nucl. Magn. Reson. Spectrosc.*, 2016, **96**, 1–46.

[11] M. H. Levitt, *Spin Dynamics: Basics of Nuclear Magnetic Resonance*, Wiley, 2013.

[12] J. Keeler, *Understanding NMR Spectroscopy*, Wiley, 2010.

[13] M. J. Duer, *Introduction to Solid-State NMR Spectroscopy*, Wiley, 2005.

[14] F. Bloch, *Phys. Rev.*, 1946, **70**, 460–474.

[15] V. I. Bakhmutov, *Practical NMR Relaxation for Chemists*, Wiley, 2004.

[16] H. E. Kerr, *NMR Crystallography of Disordered Cocrystals*, PhD Thesis, Durham University, 2017.

[17] T. Mildner, H. Ernst, and D. Freude, *Solid State Nucl. Magn. Reson.*, 1995, **5**(3), 269–271.

[18] R. L. Vold and G. L. Hoatson, *J. Magn. Reson*, 2009, **198**(1), 57–72.

[19] NMR Weblab, `https://weblab2.mpip-mainz.mpg.de/weblab/`, (accessed March 2023).

[20] J. E. Dahl, J. M. Moldowan, K. E. Peters, G. E. Claypool, M. A. Rooney, G. E. Michael, M. R. Mello, and M. L. Kohnen, *Nature*, 1999, **399**(6731), 54–57.

[21] J. E. Dahl, J. M. Moldowan, Z. Wei, P. A. Lipton, P. Denisevich, R. Gat, S. Liu, P. R. Schreiner, and R. M. Carlson, *Angew. Chemie - Int. Ed.*, 2010, **49**(51), 9881–9885.

[22] G. Mansoori, *Adv. Chem. Phys.*, 2007, **136**, 207–258.

[23] G. M. Spinella, J. T. Andrews, W. E. Bacon, R. C. Fort, and J. Sabo, *J. Chem. Thermodyn.*, 1978, **10**(11), 1023–1032.

[24] D. V. Gurrola, J. Escobedo, and G. A. Mansoori, *Proceed. of the EXITEP 98, Int'l Petroleum Tech.*, 1998, **1**, 1–11.

[25] A. Ma, Z. Jin, C. Zhu, and Z. Bai, *Nat. Gas Geosci.*, 2017, **2**(4), 239–252.

[26] S. A. Stout and G. S. Douglas, *Environ. Forensics*, 2004, **5**(4), 225–235.

[27] A. R. Britcher and J. H. Strange, *J. Chem. Soc. Faraday Trans. 2 Mol. Chem. Phys.*, 1978, **74**, 1767–1777.

[28] R. Goc, *Z. Naturforsch A Phys. Sci*, 2002, **57**, 29–35.

[29] I. L. Karle and J. Karle, *J. Am. Chem. Soc.*, 1965, **87**(4), 918–920.

[30] E. F. Westrum, A. M. McKervey, J. T. S. Andrews, R. C. Fort, and T. Clark, *J. Chem. Thermodyn.*, 1978, **10**, 959–965.

[31] T. Clark, D. E. Johnston, H. Mackle, M. A. McKervey, and J. J. Rooney, *J. Chem. Soc. Chem. Commun.*, 1972, **1**(18), 1042–1043.

[32] T. E. Jenkins and A. R. Bates, *J. Phys. C Solid State Phys.*, 1979, **12**(6), 1003–1010.

[33] R. I. Khusnutdinov, R. R. Mukminov, R. I. Aminov, L. M. Khalilov, E. S. Mescheryakova, and U. M. Dzhemilev, *Tetrahedron Lett.*, 2015, **56**, 536–538.

[34] M. L. Dheu, D. Gagnaire, H. Duddeck, F. Hollowood, and M. A. McKervey., *J. C. S. Perkin II*, 1979, **3**, 357–359.

[35] V. Z. Williams, P. R. Schleyer, G. J. Gleicher, and L. B. Rodewald, *J. Am. Chem. Soc.*, 1966, **88**(16), 3862–3863.

[36] W. Burns, A. M. McKervey, and J. J. Rooney, *J. Chem. Soc., Chem. Commun.*, 1975, **24**, 965–966.

[37] R. Cernik, E. Evans, R. Hine, and J. Richards, *Solid State Commun.*, 1978, **27**(10), 1017–1019.

[38] A. T. Balaban, D. C. Young, J. Plavec, K. Pečnik, M. Pompe, J. E. Dahl, and R. M. Carlson, *Magn. Reson. Chem.*, 2015, **53**(12), 1003–1018.

[39] Y. Dmitry, *Internal unpublished work*, 2017.

[40] J. E. Dahl, J. M. Moldowan, T. M. Peakman, J. C. Clardy, E. Lobkovsky, M. M. Olmstead, P. W. May, T. J. Davis, J. W. Steeds, K. E. Peters, A. Pepper, A. Ekuan, and R. M. Carlson, *Angew. Chemie - Int. Ed.*, 2003, **42**(18), 2040–2044.

[41] D. A. Torchia, *J. Magn. Reson.*, 1978, **30**, 613–616.

[42] H. Wickins, *A Study into the Molecular Motion of Diamondoids*, Master's Dissertation, Durham University, 2017.

[43] J. Brash, *Solid-State NMR Studies into the Molecular Motion of Diamondoids*, Master's Dissertation, Durham University, 2018.

[44] S. Sturniolo, H. M. Wickins, and P. Hodgkinson, *J. Chem. Phys.*, 2018, **158**, 244502.

[45] F. Weigand, D. E. Demco, B. Blümich, and H. W. Spiess, *Solid State Nucl. Magn. Reson.*, 1996, **6**(4), 357–365.

[46] A. A. Malär, S. Smith-Penzel, G. M. Camenisch, T. Wiegand, A. Samoson, A. Böckmann, M. Ernst, and B. H. Meier, *Phys. Chem. Chem. Phys.*, 2019, **21**(35), 18850–18865.

[47] T. M. Alam, J. P. Allers, and B. H. Jones, *Int. J. Mol. Sci.*, 2020, **21**(15), 1–20.

[48] P. K. Kahol, *Phys. Status Solidi B*, 1990, **159**(2), 873–881.

[49] J. H. Van Vleck, *Phys. Rev.*, 1948, **74**(9), 1168–1183.

[50] R. Goc, *Mol. Phys.*, 1983, **50**(2), 275–284.

[51] R. Goc, *Z. Naturforsch.*, 1997, **52**(6), 477–484.

[52] R. Goc, *J. Magn. Reson.*, 1998, **132**(1), 78–80.

[53] R. Goc, *Solid State Nucl. Magn. Reson.*, 1998, **13**(1), 55–61.

[54] R. Goc, *J. Phys. Condens. Matter*, 1999, **11**(14), 2977–2982.

[55] R. Goc, *Comput. Phys. Commun.*, 2004, **162**(2), 102–112.

[56] R. Goc, A. Pajzderska, and J. Wasicki, *Z. Naturforsch*, 2005, **60**(3), 177–182.

[57] R. Goc, *Comput. Phys. Commun.*, 2004, **162**(2), 102–112.

[58] V. E. Zorin, S. P. Brown, and P. Hodgkinson, *J. Chem. Phys.*, 2006, **125**(14), 293–304.

[59] S. J. Clark, M. D. Segall, C. J. Pickard, P. J. Hasnip, M. I. Probert, K. Refson, and M. C. Payne, *Z. Kristallogr. Cryst. Mater.*, 2005, **220**(5), 567–570.

[60] J. G. Powles and J. H. Strange, *Proc. Phys. Soc.*, 1963, **82**(1), 6.

[61] dipolar_averages `https://github.com/CCP-NC/dipolar_averages`, 2023.

[62] O. K. Farha, I. Eryazici, N. C. Jeong, B. G. Hauser, C. E. Wilmer, A. A. Sarjeant, R. Q. Snurr, S. T. Nguyen, A. O. Yazaydın, and J. T. Hupp, *J. Am. Chem. Soc.*, 2012, **134**(36), 15016–15021.

[63] E. Barea, C. Montoro, and J. A. R. Navarro, *Chem. Soc. Rev.*, 2014, **43**, 5419–5430.

[64] Q. Qian, P. A. Asinger, M. J. Lee, G. Han, K. M. Rodriguez, S. Lin, F. M. Benedetti, A. X. Wu, W. S. Chi, and Z. P. Smith, *Chem. Rev.*, 2020, **120**(16), 8161–8266.

[65] T. N. Mandal, A. Karmakar, S. Sharma, and S. K. Ghosh, *Chem. Rec.*, 2018, **18**(2), 154–164.

[66] J. Liu, L. Chen, H. Cui, J. Zhang, L. Zhang, and C. Y. Su, *Chem. Soc. Rev.*, 2014, **43**, 6011–6061.

[67] M. D. Allendorf, M. E. Foster, F. Léonard, V. Stavila, P. L. Feng, F. P. Doty, K. Leong, E. Y. Ma, S. R. Johnston, and A. A. Talin, *J. Phys. Chem. Lett.*, 2015, **6**(7), 1182–1195.

[68] M. D. Allendorf, C. A. Bauer, R. K. Bhakta, and R. J. T. Houk, *Chem. Soc. Rev.*, 2009, **38**, 1330–1352.

[69] S. Chen, R. Shang, K. L. Hu, Z. M. Wang, and S. Gao, *Inorg. Chem. Front.*, 2014, **1**(1), 83–98.

[70] A. Chauhan, S. Patel, R. Vaish, and C. R. Bowen, *Materials (Basel)*, 2015, **8**(12), 8009–8031.

[71] L. Dou, Y. H. Lin, and C. W. Nan, *Molecules*, 2021, **26**(20), 6148.

[72] H. Palneedi, M. Peddigari, G. T. Hwang, D. Y. Jeong, and J. Ryu, *Adv. Funct. Mater.*, 2018, **28**(42), 1803665.

[73] I. S. Zheludev, *Domain Structure of Ferroelectrics and Antiferroelectrics*, Springer US, Boston, MA, 1971.

[74] A. Ahmed, I. A. Goldthorpe, and A. K. Khandani, *Appl. Phys. Rev. 2*, 2015, **107**(24), 011302.

[75] E. L. Cross, *Ferroelectrics*, 1987, **76**(1), 241–267.

[76] C. W. Ahn, C. H. Hong, B. Y. Choi, H. P. Kim, H. S. Han, Y. Hwang, W. Jo, K. Wang, J. F. Li, J. S. Lee, and I. W. Kim, *J. Korean Phys. Soc.*, 2016, **68**(12), 1481–1494.

[77] R. A. Cowley, S. N. Gvasaliya, S. G. Lushnikov, B. Roessli, and G. M. Rotaru, *Adv. Phys.*, 2011, **60**(2), 229–327.

[78] Y. Shiozaki, K. Shimizu, A. Oka, N. Noda, and R. Nozaki, *Ferroelectrics*, 1999, **229**(1), 183–188.

[79] Y. Liu, B. Zhang, W. Xu, A. Haibibu, Z. Han, W. Lu, J. Bernholc, and Q. Wang, *Nat. Mater.*, 2020, **19**, 1169–1174.

[80] A. Berlie, I. Terry, M. Szablewski, M. Telling, D. Apperley, P. Hodgkinson, and D. Zeller, *Phys. Chem. Chem. Phys.*, 2022, **24**(12), 7481–7492.

[81] G. H. Fecher, J. Kübler, and C. Felser, *Materials*, 2022, **15**, 5812.

[82] R. Centore, S. Fusco, F. Capone, and M. Causa, *Cryst. Growth Des.*, 2016, **16**, 2260–2265.

[83] K. M. Ok, E. O. Chi, and P. S. Halasyamani, *Chem. Soc. Rev.*, 2006, **35**, 710–717.

[84] T. J. Hitchings, H. M. Wickins, G. U. L. Peat, P. Hodgkinson, A. K. Srivastava, T. Lu, Y. Liu, R. O. Piltz, F. Demmel, A. E. Phillips, and P. J. Saines, *J. Mater. Chem. C*, 2023, Advance Article.

[85] R. Webber and G. H. Penner, *Solid State Nucl. Magn. Reson.*, 2012, **47**, 10–18.

[86] G. Peat, *Solid-State NMR Studies into Cation Dynamics at the Phase Transition of Two MOFs*, Master's Dissertation, Durham University, 2019.

[87] R. R. Knispel and H. E. Petch, *Can. J. Phys.*, 1971, **49**(7), 870–875.

[88] M. Karimi-Jafari, L. Padrela, G. M. Walker, and D. M. Croker, *Cryst. Growth Des.*, 2018, **18**(10), 6370–6387.

[89] O. Bolton, L. R. Simke, P. F. Pagoria, and A. J. Matzger, *Cryst. Growth Des.*, 2012, **12**(9), 4311–4314.

[90] D. K. Bučar, S. Filip, M. Arhangelskis, G. O. Lloyd, and W. Jones, *CrystEngComm*, 2013, **15**(32), 6289–6291.

[91] S. Aitipamula, A. B. H. Wong, P. S. Chow, and R. B. H. Tan, *Cryst. Growth Des.*, 2014, **14**(5), 2542–2556.

[92] S. Aitipamula, P. S. Chow, and R. B. Tan, *CrystEngComm*, 2009, **11**(9), 1823–1827.

[93] R. Banerjee, P. M. Bhatt, N. V. Ravindra, and G. R. Desiraju, *Cryst. Growth Des.*, 2005, **5**(6), 2299–2309.

[94] S. Basavoju, D. Boström, and S. P. Velaga, *Cryst. Growth Des.*, 2006, **6**(12), 2699–2708.

[95] P. Billot, P. Hosek, and M. A. Perrin, *Org. Process Res. Dev.*, 2013, **17**(3), 505–511.

[96] M. Guo, X. Sun, J. Chen, and T. Cai, *Acta Pharm. Sin. B*, 2021, **11**(8), 2537–2564.

[97] S. R. Vippagunta, H. G. Brittain, and D. J. W. Grant, *Adv. Drug Deliv. Rev.*, 2001, **48**(1), 3–26.

[98] C. H. Görbitz, *Acta Crystallogr. C*, 1997, **53**(6), 736–739.

[99] C. H. Görbitz and E. Torgersen, *Acta Crystallogr. B*, 1999, **55**(1), 104–113.

[100] C. H. Görbitz and H. P. Hersleth, *Acta Crystallogr. B*, 2000, **56**(3), 526–534.

[101] C. P. Price, G. D. Glick, and A. J. Matzger, *Angew. Chemie Int. Ed.*, 2006, **45**(13), 2062–2066.

[102] WHO Model Lists of Essential Medicines (2021), `https://list.essentialmeds.org`, (accessed March 2023).

[103] Prescription Cost Analysis – England 2020/21, `www.nhsbsa.nhs.uk`, (accessed March 2023).

[104] N. De Zordi, M. Moneghini, I. Kikic, M. Grassi, A. E. Del Rio Castillo, D. Solinas, and M. B. Bolger, *Eur. J. Pharm. Biopharm.*, 2012, **81**(1), 131–141.

[105] J. Abraham Miranda, C. Garnero, A. K. Chattah, Y. Santiago De Oliveira, A. P. Ayala, and M. R. Longhi, *Cryst. Growth Des.*, 2019, **19**(4), 2060–2068.

[106] H. C. Chan, G. R. Woollam, T. Wagner, M. U. Schmidt, and R. A. Lewis, *CrystEngComm*, 2014, **16**(21), 4365–4368.

[107] A. A. Smith, M. Ernst, and B. H. Meier, *Angew. Chemie Int. Ed.*, 2017, **56**(44), 13590–13595.

[108] A. Krushelnitsky, D. Faizullin, and D. Reichert, *Biopolymers*, 2004, **73**(1), 1–15.

[109] A. J. Ilott, S. Palucha, A. S. Batsanov, K. D. Harris, P. Hodgkinson, and M. R. Wilson, *J. Phys. Chem. B*, 2011, **115**(12), 2791–2800.

[110] A. J. Cruz-Cabeza, G. M. Day, and W. Jones, *Phys. Chem. Chem. Phys.*, 2011, **13**(28), 12808–12816.

[111] P. Rossi, E. Macedi, P. Paoli, L. Bernazzani, E. Carignani, S. Borsacchi, and M. Geppi, *Cryst. Growth Des.*, 2014, **14**(5), 2441–2452.

[112] C. Shi, X. Zhang, C. H. Yu, Y. F. Yao, and W. Zhang, *Nat. Commun.*, 2018, **9**(1), 481.

[113] K. Müller and M. Geppi, *Solid-State NMR Principles, Methods, and Applications*, Wiley, 2021.

Appendix A

Second Moments of Diamantane by Method

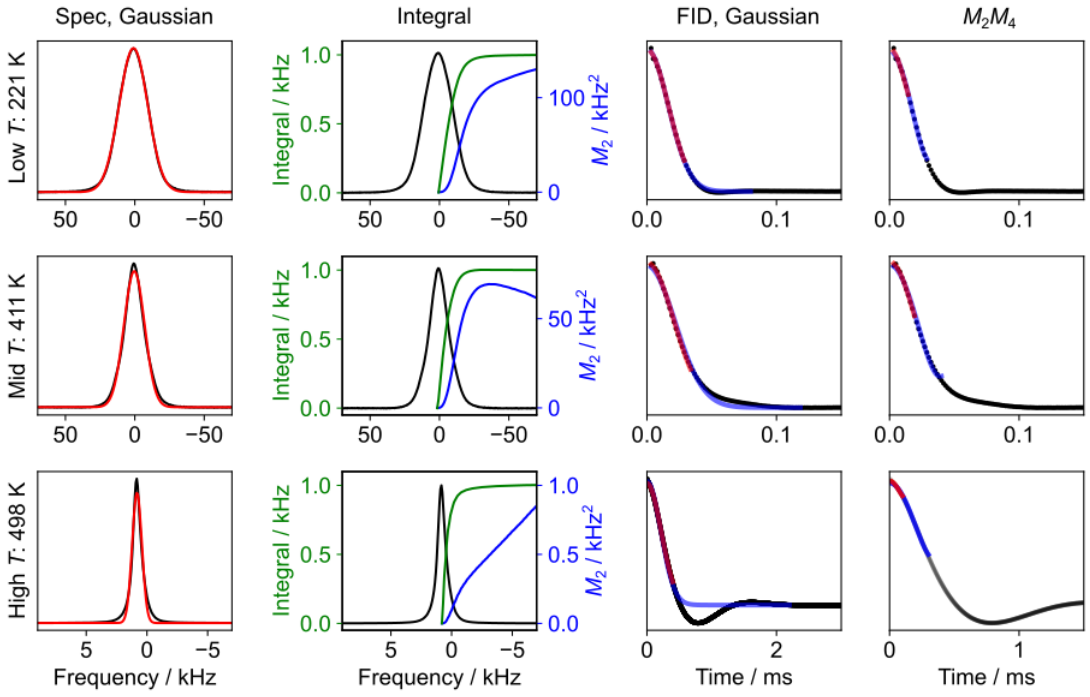

Figure A.1: Static ^{1}H spectra and FIDs of diamantane. Columns correspond to different second moment fitting methods. Column 1: Gaussian fitting (red) of the spectrum (black) and insert signal (blue). Column 2: second moment (blue) and integral (green) as a function of integral width overlaid with the spectrum (black). Column 3: Gaussian fitting (red and blue) of different fitted regions of the FID (black). Column 4: M_2M_4 method, both FID fits showing the smallest fitted region (red) and the largest region (blue).

Table A.1: Raw diamantane M_2 results.

	Spectrum			FID[a]	
	Gaussian σ / kHz	Integration / kHz^2		Gaussian σ / µs	M_2M_4 $(2\pi)^2M_2$ / Hz^2
Low T 221 K	9.838(3)	97%: 79 99%: 90	98%: 85 99.5%: 92	*30, 80 µs* 17.6(11) 17.2(11)	*15, 30 µs* $3.4(4) \times 10^9$ $3.28(5) \times 10^9$
Mid T 411 K	7.439(9)	97%: 52 99%: 61	98%: 57 99.5%: 63	*35, 120 µs* 20.48(17) 21.52(19)	*20, 40 µs* $2.46(14) \times 10^9$ $2.07(4) \times 10^9$
High T 498 K	0.4007(10)	97%: 0.33 99%: 0.48	98%: 0.38 99.5%: 0.57	*300, 800 µs* 221.8(7) 209.4(16)	*100, 300 µs* $3.52(11) \times 10^7$ $2.114(15) \times 10^7$

[a] FID fits are at two fitting ranges, both starting at $t = 0$ and ending at the values given in italics.

Table A.2: Diamantane M_2 results (in kHz^2).

	Spectrum		FID[c]	
	Gaussian[a]	Integration[b]	Gaussian	M_2M_4
Low T: 221 K	96.79(6)	85 ± 6	84 ± 8	84.0 ± 1.1
Mid T: 411 K	55.34(0.13)	57 ± 4	57 ± 3	57 ± 5
High T: 498 K	0.6101(17)	0.38 ± 0.15	0.571 ± 7	0.71 ± 0.18

[a] Values and uncertainties from least-squares fitting.
[b] Value from '98 %' integration. Uncertainty from ('99 %' − '97 %')/2
[c] Value from $(M_{2A} + M_{2B})/2$. Uncertainty from $(M_{2A} - M_{2B})/2$ where M_{2A} and M_{2B} are the largest and smallest fitted values respectively given in Table 4.7 on page 53.

Appendix B

HMF ^{15}N Fitted Parameters

Table B.1: Fitting parameters for the ^{15}N spectra of HMF with spectra given in Figure 5.14 on page 77.

Temperature / K	δ_{iso}			Relative integral		
257	−327.39	−328.43		0.58	0.42	
301	−327.13	−328.74	−329.99	0.51	0.39	0.10
314	−326.89	−328.56	−329.71	0.56	0.38	0.06
326	−326.81	−328.81		0.64	0.36	
339	−326.70	−328.78		0.71	0.29	
352	−326.64	−328.67	−327.71	0.61	0.24	0.15
364						
377	−327.62	−326.23	−326.74	0.87	0.10	0.03
390	−327.45	−326.78	−328.39	0.78	0.11	0.11

Appendix C

Error Propagation Calculations

Error on the rate: E_a and $\log_{10}(\tau_0)$

Variables with errors: $E_a \pm \delta E_a$, $\log_{10}(\tau_0) \pm \delta \log_{10}(\tau_0)$
Variables without errors: T
Constants: R, π

$$\tau_c = \tau_0 \exp\left(\frac{E_a}{RT}\right) \qquad (2.5) \qquad\qquad \nu = \frac{1}{2\pi\tau_c} \qquad (1.2)$$

$$\nu = \frac{1}{2\pi\tau_0 \exp\left(\frac{E_a}{RT}\right)} \qquad (C.1)$$

$\log_{10}(\nu) = -\log_{10}(2\pi) - \log_{10}(\tau_0) - \log_{10}(\exp(\frac{E_a}{RT}))$
$\log_{10}(\nu) = -\log_{10}(2\pi) - \log_{10}(\tau_0) - E_a/(RT\log_e(10))$

$$\boxed{\delta \log_{10}(\nu) = \sqrt{(\delta \log_{10}(\tau_0))^2 + \left(\frac{\delta E_a}{RT \log_e(10)}\right)^2}} \qquad (C.2)$$

Error on the rate: E_a and T_{min}

Variables with errors: $E_a \pm \delta E_a$, $T_{min} \pm \delta T_{min}$
Variables without errors: T, ν_0
Constants: R, π

$$\tau_c = \tau_0 \exp\left(\frac{E_a}{RT}\right) \quad (2.5) \qquad \nu = \frac{1}{2\pi\tau_c} \quad (1.2) \qquad \nu_0 = \frac{1}{2\pi\tau_c(T_{min})} \quad (6.3)$$

$$\frac{1}{2\pi\nu_0} = \tau_0 \exp\left(\frac{E_\mathrm{a}}{RT_\mathrm{min}}\right)$$

$$\tau_0 = \frac{1}{2\pi\nu_0 \exp\left(\frac{E_\mathrm{a}}{RT_\mathrm{min}}\right)}$$

$$\tau_\mathrm{c} = \frac{1}{2\pi\nu_0 \exp\left(\frac{E_\mathrm{a}}{RT_\mathrm{min}}\right)} \times \exp\left(\frac{E_\mathrm{a}}{RT}\right)$$

$$\tau_\mathrm{c} = \frac{1}{2\pi\nu_0} \exp\left(\frac{E_\mathrm{a}}{RT} - \frac{E_\mathrm{a}}{RT_\mathrm{min}}\right)$$

$$\tau_\mathrm{c} = \frac{1}{2\pi\nu_0} \exp\left(\frac{E_\mathrm{a}}{R}\left(\frac{1}{T} - \frac{1}{T_\mathrm{min}}\right)\right) \tag{C.3}$$

$$\nu = \frac{\nu_0}{\exp\left(\frac{E_\mathrm{a}}{R}\left(\frac{1}{T} - \frac{1}{T_\mathrm{min}}\right)\right)} \tag{C.4}$$

$$\log_{10}\nu = \log_{10}\nu_0 - \frac{E_\mathrm{a}}{R\log_e(10)}\left(\frac{1}{T} - \frac{1}{T_\mathrm{min}}\right)$$

$$u = E_\mathrm{a} \qquad \frac{\delta y}{\delta u} = \frac{T - T_\mathrm{min}}{RT\log_e(10)T_\mathrm{min}}$$

$$v = T_\mathrm{min} \qquad \frac{\delta y}{\delta v} = \frac{E_\mathrm{a}}{R\log_e(10){T_\mathrm{min}}^2}$$

$$(\delta\log_{10}\nu)^2 = (\delta E_\mathrm{a})^2\left(\frac{T - T_\mathrm{min}}{RT\log_e(10)T_\mathrm{min}}\right)^2 + (\delta T_\mathrm{min})^2\left(\frac{E_\mathrm{a}}{R\log_e(10){T_\mathrm{min}}^2}\right)^2$$

$$\delta\log_{10}\nu = \sqrt{\left(\frac{\delta E_\mathrm{a}(T - T_\mathrm{min})}{RT\log_e(10)T_\mathrm{min}}\right)^2 + \left(\frac{\delta T_\mathrm{min}E_\mathrm{a}}{R\log_e(10){T_\mathrm{min}}^2}\right)^2}$$

$$\delta\log_{10}\nu = \sqrt{\frac{(\delta E_\mathrm{a}T_\mathrm{min}(T - T_\mathrm{min}))^2 + (\delta T_\mathrm{min}E_\mathrm{a}T)^2}{(RT\log_e(10){T_\mathrm{min}}^2)^2}}$$

$$\boxed{\delta\log_{10}\nu = \frac{1}{RT\log_e(10)(T_\mathrm{min})}\sqrt{(\delta E_\mathrm{a}(T - T_\mathrm{min}))^2 + \left(\frac{\delta T_\mathrm{min}E_\mathrm{a}T}{T_\mathrm{min}}\right)^2}} \tag{C.5}$$

Appendix D

FSPA Ethanol-d_2 Deuterium Lineshape Simulations

D.1 Weblab Parameters

Table D.1: Inputted parameters in Weblab.[19] 1D echo, expert mode.

	Simulation number			
	1	2	3	4
Tensor Settings				
Spin	1			
Coupling δ_0	120 kHz			
Asymmetry ν_0	0.0			Variable
Euler angle α_0	0.0 °	0.0 °		0.0 °
Cone Settings				
Number of cone axes	1	2		1
Euler angle α_1	N/A	90 °		N/A
Cone 1				
Timescale of motion	Intermediate	Very fast		Intermediate
Type of motion	2-site	2-site	3-site	2-site
Cone angle	59 °	Variable		59 °
Jump angle	180 °	180 °	120 °	180 °
Jump rate	Variable	N/A		Variable
Cone 2				
Timescale of motion	N/A	Intermediate		N/A
Type of motion	N/A	2-site		N/A
Cone angle	N/A	59 °		N/A
Jump angle	N/A	180 °		N/A
Jump rate	N/A	Variable		N/A

Continued on next page

Table D.1 continued from previous page. Legend on page 130.

	1	2	3	4
Populations	N/A	0.5 0.5	0.5 0.5	N/A
Sample Settings				
Sample spinning	No			
Sample type	Powder			
Other Settings				
Pulse-delay	30 µs			
Broadening	Gaussian, 4 kHz			
Quality of spectrum	High			
Number of points	256			
Plot range x axis	−200 to 200 kHz			
Plot y axis	Auto			

D.2 Simulated ^{2}H Spectra with Different Motional Models

Simulated spectra on following pages. Legend given below.

- 2 cones: 1) 2 site wobble, $y°$, fast limit 2) 2 site jump, 59°, x kHz
- 2 cones: 1) 3 site wobble, $y°$, fast limit 2) 2 site jump, 59°, x kHz
- 1 cone: 2 site jump 59°, x kHz
- 1 cone: 2 site jump, $y°$, fast limit
- 1 cone: 3 site jump, $y°$, fast limit

Table D.2: Simulated ^{2}H spectra of different motional models. Legend on page 130.

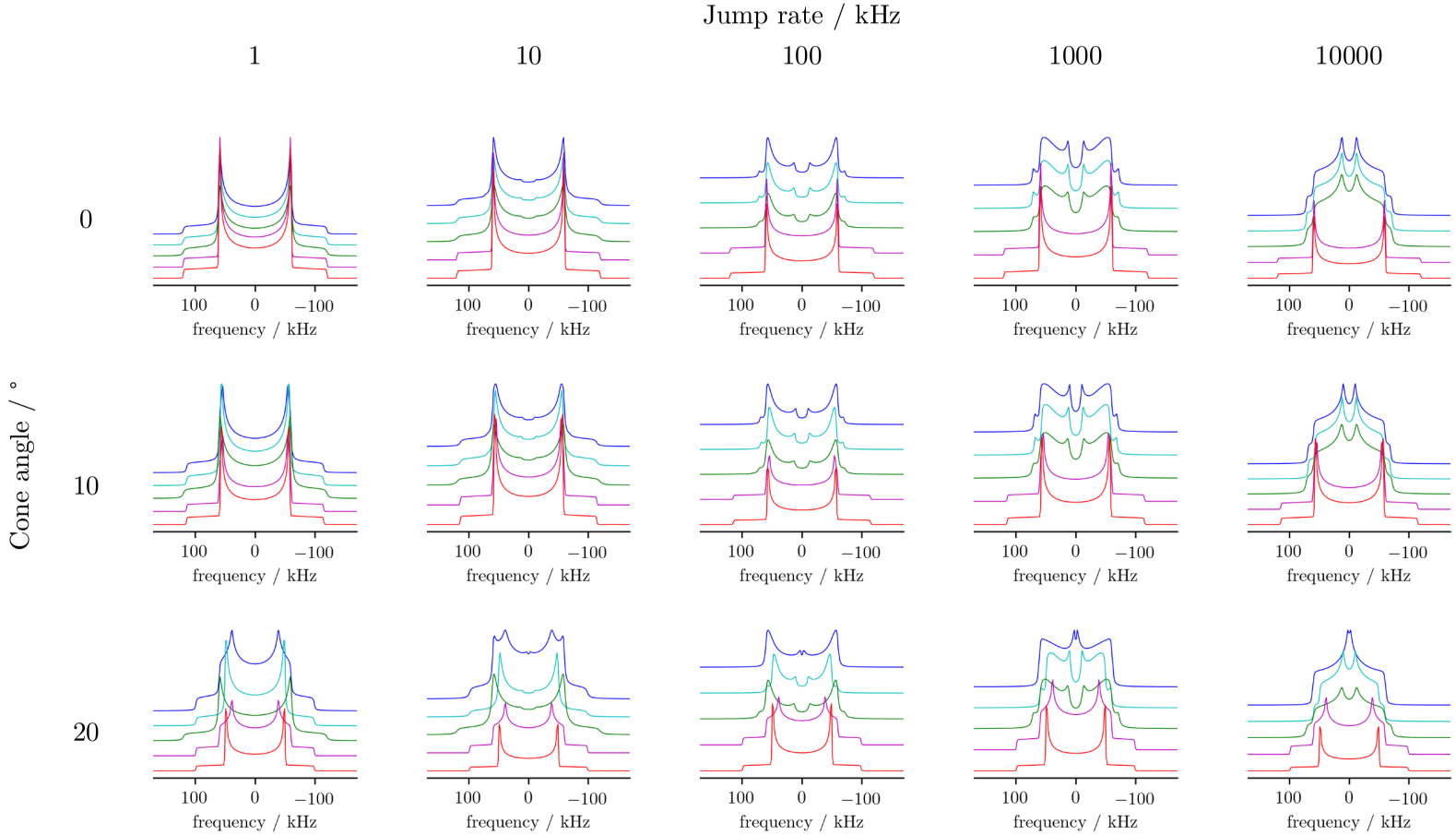

Table D.2 continued from previous page. Legend on page 130.

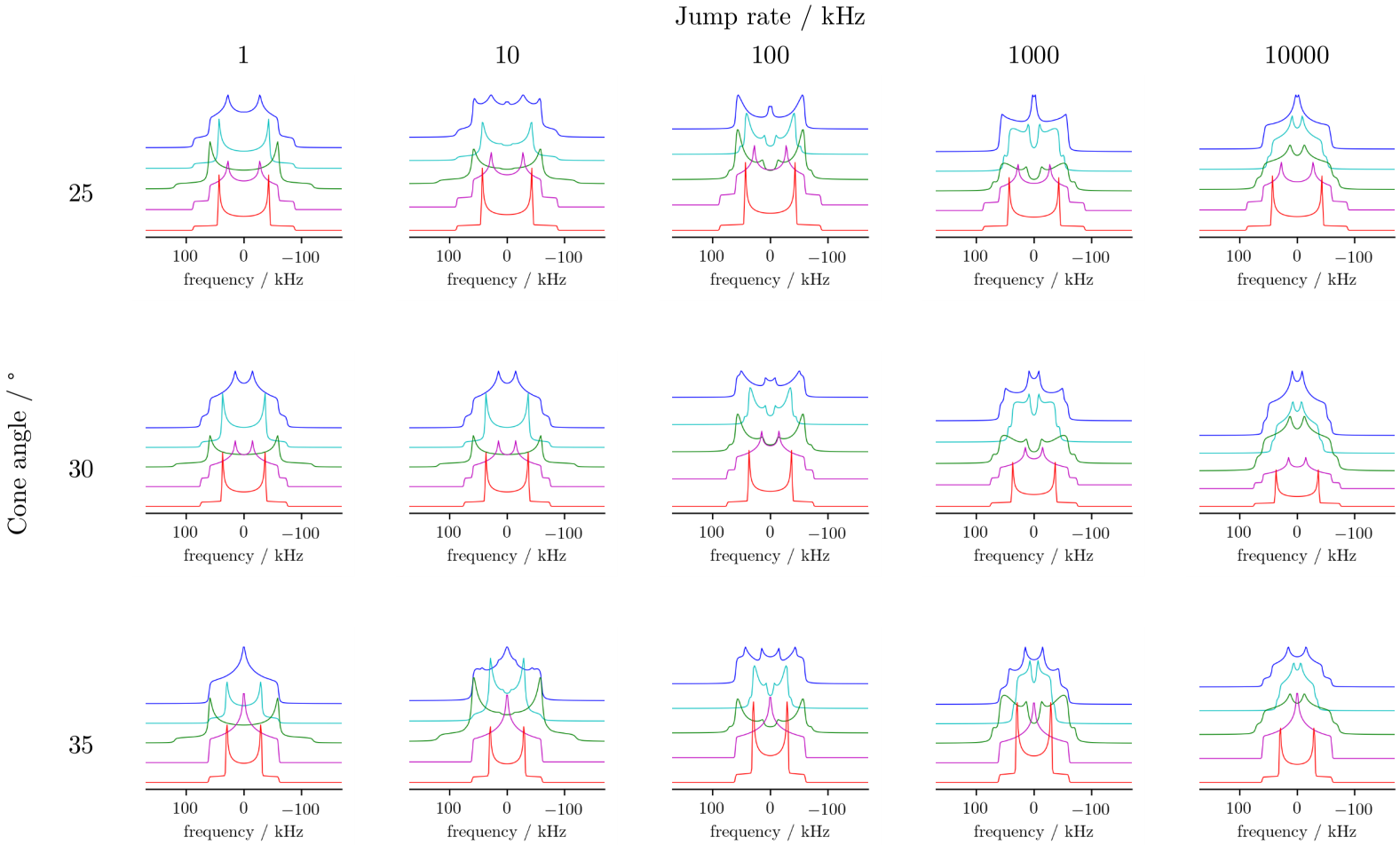

Table D.2 continued from previous page. Legend on page 130.

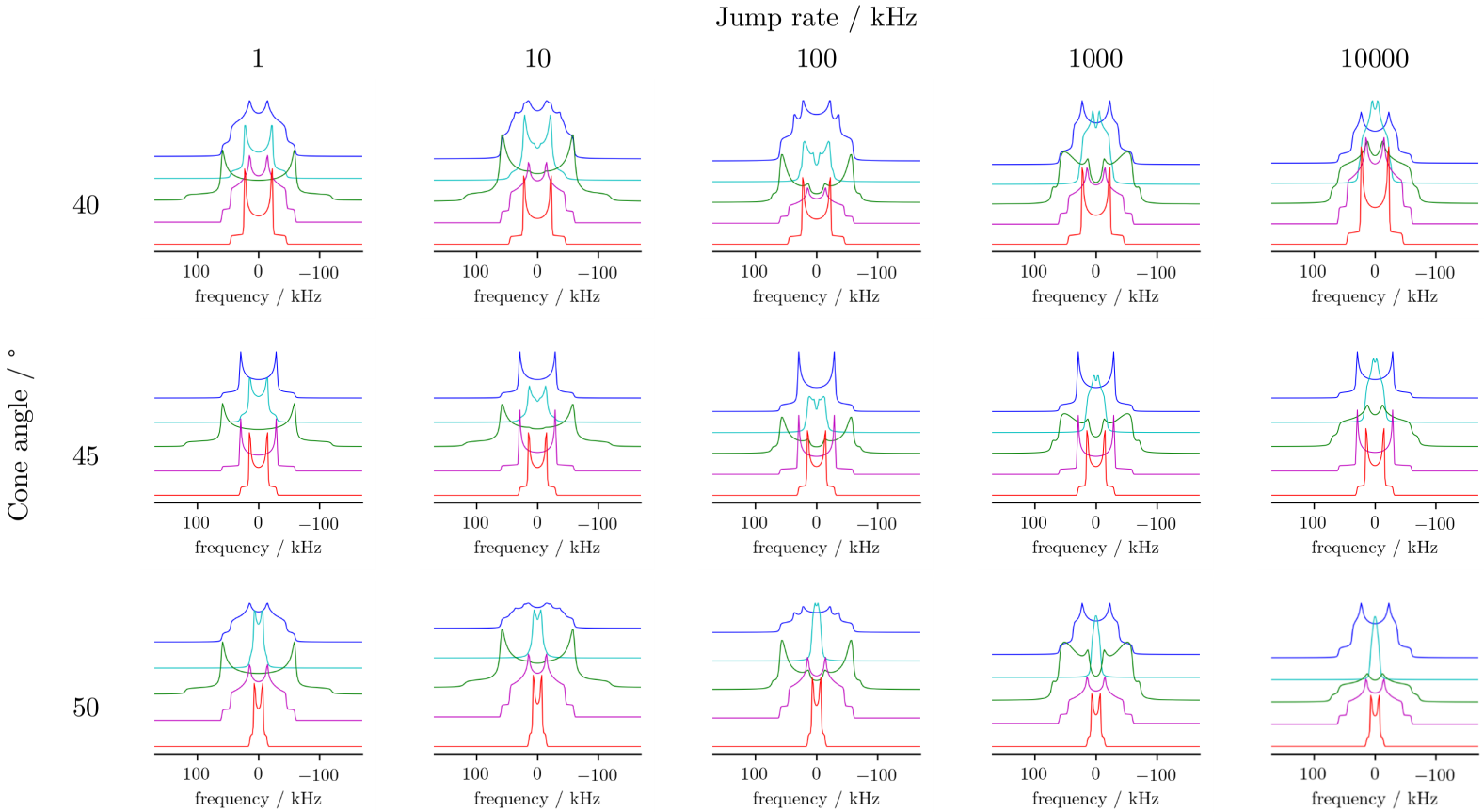

Table D.2 continued from previous page. Legend on page 130.

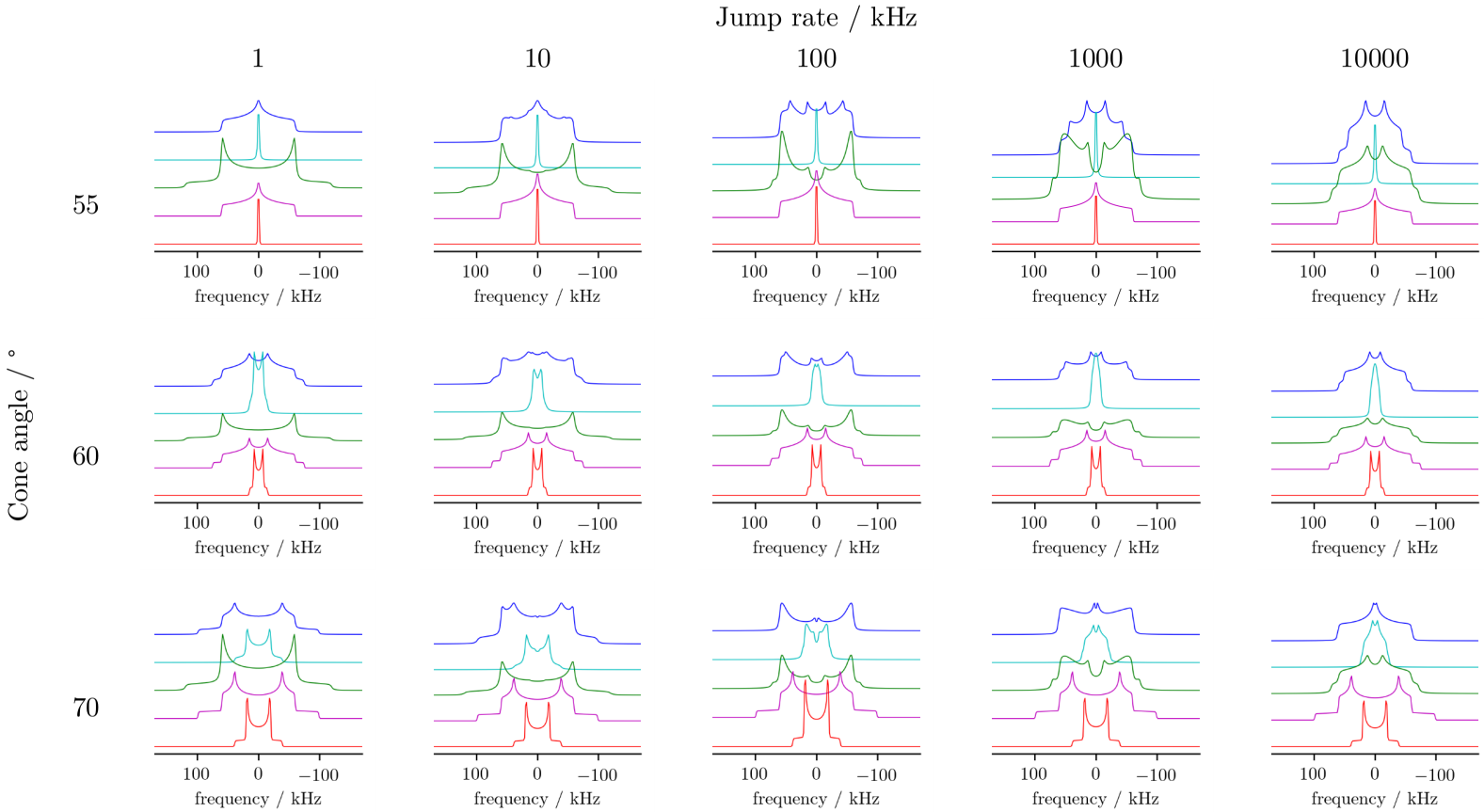

Table D.2 continued from previous page. Legend on page 130.

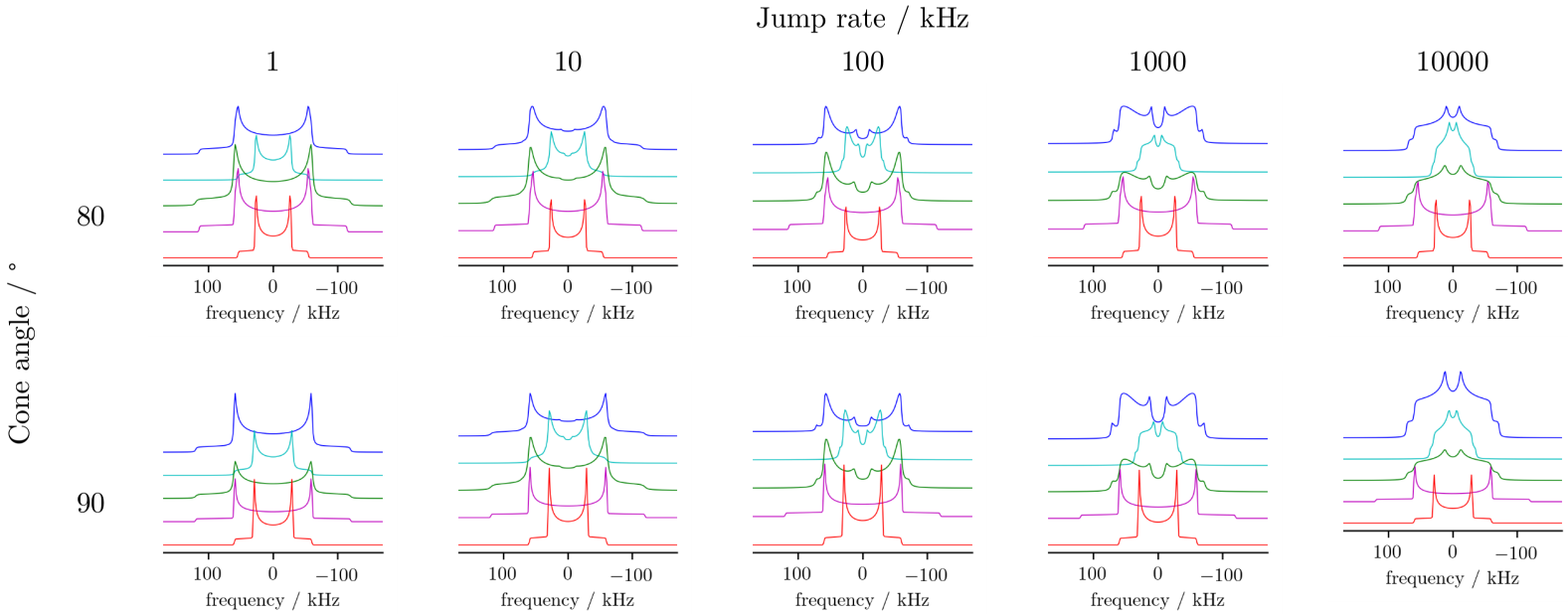

Table D.3: Simulated ^{2}H spectra, variable η_0 of a C_2 jump 59 °, variable speed (shown in the table heading), variable eta (shown in the legend, left of table)